Astronomy Letters, Vol. 28, No. 4, 2002, pp. 207–216. Translated from Pis'ma v Astronomicheskiĭ Zhurnal, Vol. 28, No. 4, 2002, pp. 243–252.

A Chemically Decoupled Nucleus and Inner Polar Ring of the SBb Galaxy NGC 4548

O. K. Sil'chenko*

Sternberg Astronomical Institute, Universitetskii pr. 13, Moscow, 119899 Russia

Received November 29, 2001

Abstract—Our investigation of the central region in NGC 4548, a bright Sb galaxy with a large-scale bar, using the Multipupil Field Spectrograph of the 6-m telescope revealed a chemically decoupled compact stellar nucleus with [Fe/H] = +0.6 and [Mg/Fe] = +0.1 . . . + 0.2 and with a mean stellar-population age of 5 Gyr. This nucleus, a probable circumnuclear disk coplanar with the global galactic disk, is embedded in the bulge whose stars are generally also young, $T \approx 4$ Gyr, although they are a factor of 2.5 more metal-poor. The bulge of NGC 4548 is triaxial and has a de Vaucouleurs surface-brightness profile; the unusual characteristics of its stellar population suggest the bulge formation or completion in the course of secular evolution in the triaxial potential of the global bar. The ionized gas within 3″ of the NGC 4548 nucleus rotates in a plane inclined to the principal symmetry plane of the galaxy, possibly, even in its polar plane, which may also result from the action of the large-scale bar. © *2002 MAIK "Nauka/Interperiodica".*

Key words: *galaxies, groups and clusters of galaxies, intergalactic gas*

INTRODUCTION

We began our searches for chemically decoupled nuclei in disk galaxies with the Multipupil Field Spectrograph of the 6-m telescope in 1989 (Sil'chenko *et al.* 1992). The detectors were changed several times in the course of our work, each time marking a qualitative leap in the informativeness of our data; the spectrograph itself was changed twice. We have discovered a total of almost thirty galaxies with chemically decoupled nuclei. Having come across this phenomenon, we also analyzed other galaxy properties—the kinematics of gas and stars in the central region, its structure, and peculiarities of the global galactic structure, etc.—in an attempt to guess which of them could be related to the origin of the chemically decoupled nuclei. In particular, these efforts led to the discovery of circumnuclear polar gaseous disks. It has long been known that there is a rare type of peculiar galaxies, galaxies with global polar rings [see the catalog of such galaxies by Whitmore *et al.* (1990)]. Occasionally, but rarely, the polar rings are smaller in size than the galaxy itself, as, for example, in the case of IC 1689 (Hagen-Thorn and Reshetnikov 1997; Sil'chenko 1998). We also know cases where the rotation axes of the circumnuclear ionized gas and circumnuclear stars in early-type galaxies devoid of gas outside the central region are misaligned (see, e.g., Bertola *et al.* 1992, 1995). In both cases, a universally accepted explanation of the phenomenon was the capture by the galaxy of a foreign gas whose angular momentum does not necessarily coincide with the angular momentum of the capturing galaxy. However, for the first time, we have discovered circumnuclear polar disks in spiral galaxies with a large amount of normally rotating gas in the global disks outside the central region: in the Sb galaxy NGC 2841 (Sil'chenko *et al.* 1997) and the Sa galaxies NGC 6340 (Sil'chenko 2000) and NGC 7217 (Zasov and Sil'chenko 1997; Sil'chenko and Afanasiev 2000). In these cases, it is hard to suggest that the captured gas with an orthogonal angular momentum immediately reached the center of the capturing galaxy by avoiding collisions with clouds of its own gas; besides, the galaxies turned out to be isolated. It would be more natural to search for an intrinsic mechanism of transferring the galactic circumnuclear gas to a polar orbit. This mechanism has already been hinted at in the literature devoted to three-dimensional gas dynamics in a triaxial potential. By numerically simulating the secular evolution of a flat cold stellar–gaseous disk, Friedli and Benz (1993) obtained stable orbits for gaseous clouds with the opposite sense of rotation in a plane inclined to the global galactic plane after the stellar-bar formation. A qualitative reasoning of Sofue and Wakamatsu (1994) led them to conclude that the dissipative component of the galactic disk (gas) during its interaction with a bar must lose the tangential velocity component, increase the radial velocity of the motion toward the center, and keep

*E-mail: olga@sai.msu.su

Spectroscopic observations of NGC 4548

Date	T(exp), min	PA(top)	Range, Å	FWHM$_*$
May 8–9, 1997	60	75°	4600–5600	2.5″
May 8–9, 1997	40	75	6000–7000	2.5

the vertical velocity component constant; collectively, all these factors must give rise to circumnuclear polar gaseous disks in barred galaxies. Observations seem to confirm the relationship of the circumnuclear polar rings to the presence of a triaxial potential in the galaxy: although all three galaxies in which we detected this phenomenon are formally not classified as barred, our morphological analysis of their isophotes suggests the existence of triaxial bulges in NGC 2841 and NGC 6340 and an oval dense inner disk (a lens?) in NGC 7217.

The galaxy NGC 4548, which is dealt with here, possesses an indubitable large-scale bar and has always been classified as SBb. In contrast to the slightly triaxial structures in NGC 2841, NGC 6340, and NGC 7217, NGC 4548 has a thin, high-contrast bar. A morphological analysis of this galaxy is also facilitated by the fact that it is seen almost, but not exactly face-on (all structural features can be closely examined), which also allows the kinematics of its gas and stars to be analyzed in the galactic disk plane. The basic parameters of NGC 4548 are:

Morphological type	SBb
R_{25}	13 kpc
B_T^0	10.60
M_B	−20.98
V_r(radio)	485 km s^{-1}
Distance	17 Mpc (Virgo)
Line-of-sight inclination	37°
$PA_{\rm phot}$	150°
v_m, km s^{-1}	180
σ_*, km s^{-1}	155

It is all the more interesting to search for a circumnuclear polar ring in such a classical triaxial potential. NGC 4548 was also included in our list of candidates with chemically decoupled nuclei (Sil'chenko 1994) and, as such, was observed with the Mutipupil Field Spectrograph of the 6-m telescope as part of our program of searching for chemically decoupled nuclei in disk galaxies. Here, we present the results of these observations.

OBSERVATIONS AND DATA REDUCTION

The central part of NGC 4548 was observed with the Multipupil Field Spectrograph (MPFS) at the prime focus of the 6-m Special Astrophysical Observatory (SAO) telescope [see Afanasiev *et al.* (1990) for a description of the instrument] near the Mg Ib λ 5175 Å absorption line and Hα with a reciprocal dispersion of 1.6 Å per pixel (a spectral resolution of ~ 4 Å). A log of our spectroscopic observations for NGC 4548 is given in the table.

The detector for the MPFS was a Russian-made 1040×1160-pixel CCD array produced by the Elektron research-and-production association. During the MPFS observations, a 8×16 array of microlenses formed a pupil matrix, which was fed to the entrance of a grating spectrograph. This configuration allows up to 128 spectra to be simultaneously taken, each corresponding to a $1.3'' \times 1.3''$ spatial element of the galaxy image. We separately took a comparison spectrum of a helium–neon–argon lamp for wavelength calibration and a dawn-sky spectrum to make corrections for vignetting and for different microlens transmission. We also separately exposed the sky background near the galaxy in the green spectral range where the absorption-line equivalent widths were to be calculated; its spectra were then smoothed and subtracted from the object spectra. The main data reduction steps included the following: bias subtraction, cosmic-ray particle hit removal, the extraction of one-dimensional spectra from the matrix format, the linearization of extracted spectra, and the construction of two-dimensional surface-brightness distributions and velocity fields. These were performed with a software package developed at the SAO (Vlasyuk 1993).

We used the MPFS observations in the spectral range 4600–5600 Å, first, to investigate the radial dependences of the absorption-line equivalent widths and, second, to construct the two-dimensional line-of-sight velocity field of stars at the galactic center. The first goal was achieved by adding up the spectra in concentric rings centered on the galactic nucleus with a width and radial step of 1.3″, i.e., equal to the spatial element size (in this way, we managed to maintain an approximately constant signal-to-noise ratio along the radius, which is unattainable, say, in long-slit observations). Subsequently, we calculated the Hβ, Mgb, Fe5270, and Fe5335 indices in the standard Lick system (Worthey *et al.* 1994). Detailed model calculations in terms of old stellar population synthesis models are available for the above strong absorption lines (Worthey 1994; Vazdekis *et al.* 1996; Tantalo *et al.* 1998). To achieve the second goal, the spectrum of each spatial element after the continuum subtraction and conversion to the velocity scale was

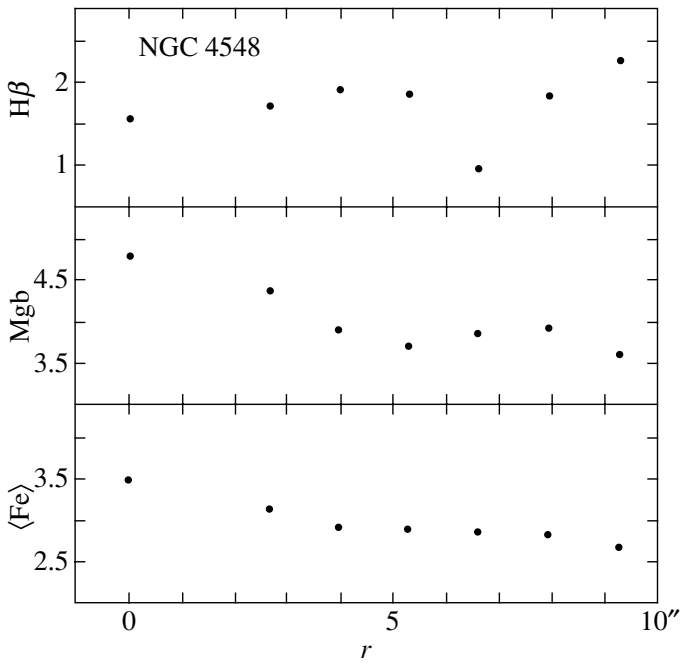

Fig. 1. Radial variations in the azimuthally averaged absorption-line indices Hβ, Mgb, and $\langle \mathrm{Fe} \rangle \equiv (\mathrm{Fe5270} + \mathrm{Fe5335})/2$, as inferred from our MPFS data for NGC 4548.

cross-correlated with the spectra of the K0–K2 III giant stars observed during our set with the same instrumentation as for the galaxy. The observations in the red spectral range were used to construct the two-dimensional line-of-sight velocity field of ionized gas. To this end, we accurately measured the centroid positions of the [N II] λ 6583 Å emission line; since NGC 4548 is a LINER, the Hα emission is weak in its circumnuclear region. The night-sky λ 5577, 6300, and 6864 Å lines were used to check the accuracy of the wavelength scale and the measured velocity zero point. We estimated the accuracy of individual line-of-sight velocity measurements for stars and gas to be 20 and 30 km s^{-1}, respectively, and the accuracy of determining the absorption-line equivalent widths in the azimuthally averaged spectra to be 0.15 Å.

We made use of data from the Hubble Space Telescope (HST) archive and from the Digital Atlas of Nearby Galaxies by Frei *et al.* (1996) to morphologically investigate the central part of NGC 4548. The galaxy was imaged with the STIS/HST instrument on April 26, 1999, as part of the program "The Nature of Nuclear Activity in Nearby Galaxies" by H.-W. Rix. A very broadband (1000 Å) filter centered at 7150 Å was used; the exposure time was 60 s. The scale with which the central part of the galaxy $5'' \times 5''$ in size was exposed was $0.05''$ per pixel. The image morphology was analyzed with the FITELL code written by V.V. Vlasyuk.

A CHEMICALLY DECOUPLED NUCLEUS IN NGC 4548

Figure 1 shows the radial dependences of the azimuthally averaged Lick indices Hβ, Mgb, and $\langle \mathrm{Fe} \rangle \equiv (\mathrm{Fe5270} + \mathrm{Fe5335})/2$. Note that the dependences are flat at radii larger than $3''$ (if the Hβ spike at $R = 6.6''$ is assumed to be fortuitous). The indices, particularly the metal indices, are virtually constant outside the zone of influence of the unresolved nucleus, FWHM $\approx 2.5''$. We can calculate the following means from five points in the range $R = 4''$–$9''$: $\langle \mathrm{Mgb} \rangle_{\mathrm{bul}} = 3.82 \pm 0.06$ Å and $\langle \mathrm{Fe} \rangle_{\mathrm{bul}} = 2.85 \pm 0.04$ Å. The estimates of the rms scatter from point to point are 0.14 Å and 0.09 Å, respectively, which is completely within the limits of our observational (statistical) error, 0.15 Å. If we now compare the above calculated mean circumnuclear values of Mgb and $\langle \mathrm{Fe} \rangle$ with the indices measured in the unresolved nucleus, $\mathrm{Mgb}_{\mathrm{nuc}} = 4.82$ Å and $\langle \mathrm{Fe} \rangle_{\mathrm{nuc}} = 3.50$ Å, then we will immediately see that NGC 4548 possesses a chemically decoupled nucleus. Having been calibrated in terms of the metallicity difference (assuming the stellar populations to be of the same age), the differences in the nuclear and circumnuclear metal indices, $\Delta\mathrm{Mgb} = 1.00$ Å and $\Delta\langle \mathrm{Fe} \rangle = 0.65$ Å, correspond, according to the models by Worthey (1994), to $\Delta[\mathrm{Fe/H}] \approx 0.4$; i.e., the mean metallicity of nuclear stars in NGC 4548 is a factor of 2.5 higher

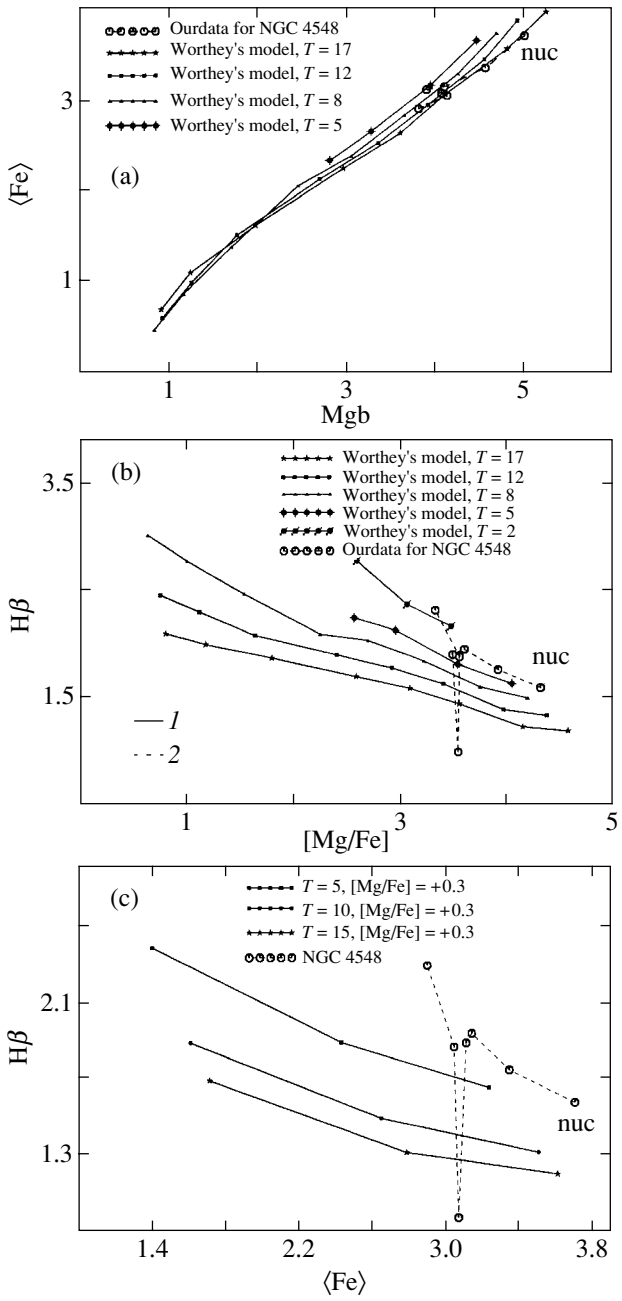

Fig. 2. Diagnostic index–index diagrams: a comparison of models with the azimuthally averaged observational data for NGC 4548. The large symbols connected by lines *2* represent the observational data for NGC 4548 taken along the radius at 1.3″ steps; the nucleus position is marked by "nuc." (a) The (⟨Fe⟩, Mgb) diagram with the models by Worthey (1994) for [Mg/Fe] = 0, (b) the (Hβ, [MgFe] $\equiv$ (Mgb⟨Fe⟩)$^{1/2}$) diagram with the models by Worthey (1994) for [Mg/Fe] = 0, and (c) the (Hβ, ⟨Fe⟩) diagram with the models by Tantalo *et al.* (1998) for [Mg/Fe]= +0.3. Lines *1* connect the models of the same age; the small symbols mark the positions of the models with the following metallicities (from right to left): +0.50, +0.25, 0.00, −0.22, −0.50, −1.00, −1.50, −2.00 for the models by Worthey (1994) and +0.4, 0.0, −0.7 for the models by Tantalo *et al.* (1998).

than the mean metallicity of stars in the immediate vicinity of its nucleus.

Meanwhile, not only metallicity but also the mean age of the stellar population affects the metal-line depth in the integrated stellar-population spectrum: the younger it is, the shallower the metal lines are. Note that the hydrogen absorption lines exhibit an exactly opposite behavior and a comparison of the metal and hydrogen-line indices allows one to remove degeneracy and to simultaneously determine both parameters of the stellar population (Sil'chenko 1993; Worthey 1994). It should only be made sure that the magnesium-to-iron abundance ratio in the models used to determine the stellar-population parameters correspond to the actual Mg/Fe ratio in the galaxy under study. Otherwise, an ambiguity in the choice of the metal index to be compared with Hβ arises.

The (⟨Fe⟩, Mgb) diagram (Fig. 2a) compares the observed, azimuthally averaged indices at various distances from the NGC 4548 center with the models for old stellar populations calculated by Worthey (1994) at a solar magnesium-to-iron abundance ratio, [Mg/Fe] = 0. In the (⟨Fe⟩, Mgb) diagram, the models for [Mg/Fe] = 0 occupy a narrow band containing stellar systems of all metallicities, ages, and star-formation histories; the deviations of the observed points from this band can be unequivocally interpreted as a nonsolar magnesium-to-iron abundance ratio. At first glance, the observed indices for NGC 4548 satisfy the solar Mg/Fe ratio at all radii; however, a slight radial drift of the points across the [Mg/Fe] = 0 band may still be noticed. Since, in addition, as we will see below, the mean age of the nuclear stellar population does not exceed 5 Gyr, we must admit a small magnesium overabundance for the NGC 4548 nucleus, [Mg/Fe] = +0.1 . . . + 0.2. By contrast, [Mg/Fe] = 0 in the circumnuclear region.

Keeping this result in mind, we turn to the diagrams that diagnose the stellar-population age by comparing the Hβ index with one of the metal indices or their combination. Figure 2b shows a comparison of the observations with the models by Worthey (1994) for [Mg/Fe] = 0. It must be used to determine primarily the parameters of the circumnuclear region. We see that the circumnuclear stellar population, if we discard the outlier, is fairly young, $T \approx 4$ Gyr, and metal-rich, [Fe/H] $\approx +0.2$. If this circumnuclear region is a bulge, then such unusual parameters of its stellar population suggest the bulge formation or, to be more precise, completion over the entire galaxy lifetime; i.e., there is clear evidence of the so-called secular evolution. To determine the age of the nuclear stellar population in NGC 4548, we take into account its magnesium overabundance and, in

addition to Fig. 2b, invoke the diagram in Fig. 2c, where the models by Tantalo *et al.* (1998) are shown for [Mg/Fe] = +0.3. The two diagrams suggest that the mean age of the nuclear stellar population in NGC 4548 is about 5 Gyr and the mean metallicity is monstrously high: [Fe/H] ≈ +0.6! Thus, in contrast to our previously studied central regions of galaxies with chemically decoupled nuclei, the sharp radial decrease in metallicity in NGC 4548 is not accompanied by a significant age gradient. This implies that in the case under consideration, the chemical "decoupleness" of the nucleus did not result from an isolated compact star-formation burst in it but simply suggests that the secondary star formation proceeded in the nucleus faster and more effectively than in the circumnuclear region.

THE KINEMATICS OF GAS AND STARS IN THE CENTRAL REGION OF NGC 4548

In kinematic studies, the use of two-dimensional spectroscopy is of fundamental importance: only when analyzing the two-dimensional line-of-sight velocity field of gas or stars can the pattern of rotation be established without assuming *a priori* that it is circular. Indeed, if the stars are distributed and rotate in a thin circular disk (or, in a more general sense, if the geometry and rotation are axisymmetric), then by looking at it at some angle, we will see, in projection onto the sky, an ellipse and a maximum line-of-sight velocity, the projected rotation velocity, on the major axis of this ellipse, which will coincide with the line of nodes of the galactic plane. Simple geometric considerations allow us to write out the following formula for the azimuthal variation in the apparent line-of-sight velocity gradient within the region of rigid rotation:

$$dv_r/dr = \omega \sin i \cos(PA - PA_0),$$

where ω is the angular velocity of the galactic center, i is the inclination of the galactic-disk rotation axis to the line of sight, and PA_0 is the position angle of the line of nodes. Thus, for a circular (axisymmetric) distribution and rotation of stars, the isophotal major axis coincides with the line of nodes, while the central velocity-field isoline, the line of a zero relative line-of-sight velocity, is perpendicular to this direction. In a triaxial potential, for example, in a bar, the velocity-field isolines turn along the bar. Thus, if the direction of the maximum line-of-sight velocity gradient is called a kinematic major axis, then the kinematic and photometric major axes in a triaxial potential must turn in opposite directions from the line of nodes of the disk [see Monnet *et al.* (1992) and Moiseev and Mustsevoi (2000) for more details].

Figure 3 shows the two-dimensional line-of-sight velocity fields for stars and ionized gas at the center of NGC 4548 that we obtained from our MPFS observations. The stars (Fig. 3a) exhibit a regular quasi-rigid rotation over the entire segment under study. A cosine-wave fit to the azimuthal variations in dv_r/dr indicates that within 3″ of the center, the kinematic major axis is oriented at $PA = 145°$; i.e., it virtually coincides with the line of nodes of the global galactic disk (see an isophotal analysis below and conclusions in the Introduction). Further out, at $R = 3''$–$5''$, $PA_{0,\mathrm{kin}} = 134.5°$. This may imply a turn of the kinematic major axis from the nodal line, but it is not very significant. The cosine-wave amplitude in the two radial ranges is 11 km s^{-1} arcsec^{-1} ($\pm 5 \ldots 6$ km s^{-1} arcsec^{-1}), which confirms the rigid rotation of the stars within 5″ of the center; given the projection effect, the angular velocity at the center is 18 km s^{-1} arcsec^{-1} or about 220 km s^{-1} kpc^{-1}. The appearance of the ionized-gas velocity field is completely different (Fig. 3b). Near the galactic nucleus, within 3″–4″ of the center, we see the lines of equal velocities to turn through 90°. At the very center, the cosine-wave fit to the azimuthal dependence of the line-of-sight velocity gradients clearly yields an angular velocity of 19 ± 9 km s^{-1} arcsec^{-1} and the orientation of the kinematic major axis $PA_{0,\mathrm{kyn}} = 236°$. That the gas rotates slightly faster than the stars is, in principle, normal, considering an appreciable stellar velocity dispersion in the NGC 4548 bulge (see conclusions in the Introduction). However, the position angle of the kinematic major axis for ionized gas within 3″ of the NGC 4548 center differs by 91° from that of the kinematic major axis for stars; i.e., we may observe an exactly polar circumnuclear gaseous disk. In this case, the difference between the apparent cosine-wave amplitudes constructed from the line-of-sight velocity gradients of gas and stars can most likely be attributed to the difference between the inclinations of the rotation planes to the line of sight: we must see the polar disk almost edge-on, and the correction to the gas rotation velocity for the projection effect must be small. A blue image of the central part of NGC 4548 with a high spatial resolution would help in determining the exact orientation of its circumnuclear gaseous disk: since the galaxy is seen nearly face-on, the polar gaseous disk could manifest itself as a thin dust lane passing through the bright central part of the bulge. It is by this configuration that we first suspected a circumnuclear polar gaseous disk in NGC 6340, which was subsequently confirmed by kinematic data (Sil'chenko 2000). Unfortunately, however, only a red image of NGC 4548 was obtained with the STIS/HST instrument; al-

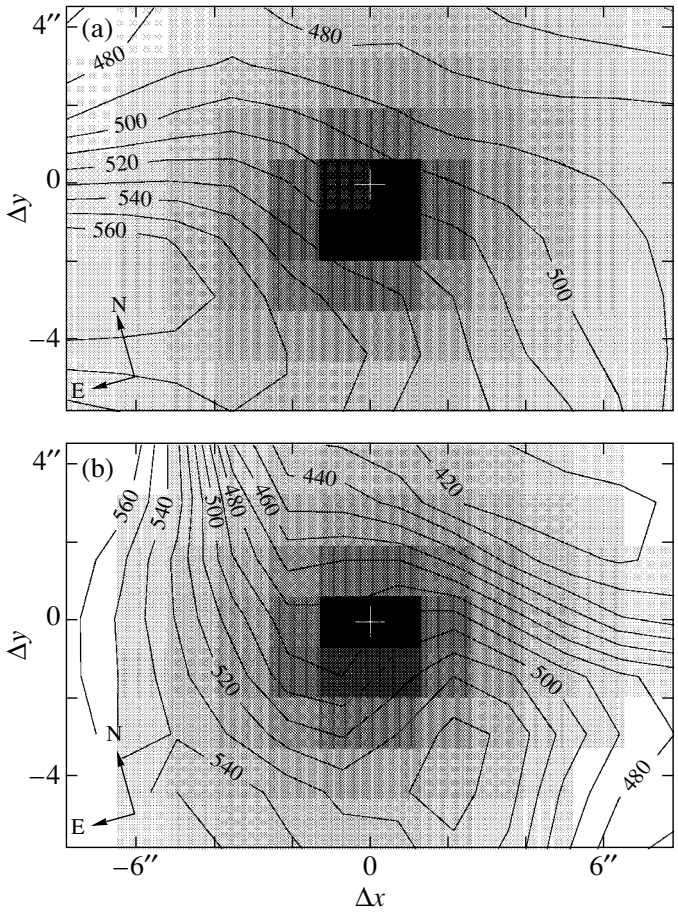

Fig. 3. Two-dimensional line-of-sight velocity fields for (a) stars and (b) ionized gas at the center of NGC 4548, as derived from our MPFS data (isolines). The gray-scaled background indicates the continuum intensity map; the cross marks the photometric center of the galaxy.

though it reveals a rich morphology (see below), there is no clear evidence for the presence of dust.

Nevertheless, let us turn to the morphological characteristics of the isophotes in the central region of NGC 4548, which are of considerable interest. Figure 4 shows the data obtained with various spatial resolutions. Whereas the seeing during the observations by Frei *et al.* (1996) was $2.3''$–$2.6''$, the seeing during the observations by Rauscher (1995) was $0.75''$ and the HST spatial resolution was $0.1''$–$0.2''$. Still, there is general agreement between the data even near the very center. At the galactic center, at $R < 2''$, according to Rauscher (1995), and at $R < 0.5''$ if we use the HST/STIS data, the isophotal orientation comes to $PA = 140°$–$150°$, i.e., to the line of nodes. Since, as we now know, the kinematic major axis of the circumnuclear stars is also oriented at $PA_{0,\mathrm{kin}} = 145°$, this coincidence proves that the rotation (and distribution) of stars at the very center of NGC 4548 is axisymmetric, despite the existence of a global bar in the galaxy. This is all the more surprising, because there is ample evidence that the global bar is not the only triaxial structure in NGC 4548. According to Fig. 4, the orientation of the isophotal major axis in the range of distances from the center $2''$–$14''$ is kept near $PA \sim 100°$–$120°$; this is neither the line of nodes (148°) nor the global-bar direction (60°). The ellipticity in this radial range exhibits a local maximum, $1 - b/a = 0.13$, at $R \approx 6''$. Since 0.13 is less than 0.2, the ellipticity of the outer isophotes that corresponds to a global-disk inclination of 38°, this structure cannot be a flat secondary bar in the thin disk. It most closely resembles a triaxial bulge.

Let us now look at the same morphological characteristics of the isophotes on the scale of the entire galaxy (Fig. 5). The quiet, undisturbed global disk of NGC 4548 shows up only at $R > 120''$, or 10 kpc: the spiral arms are a hindrance closer to the center, while at $R \approx 30''$–$60''$, the thin high-contrast bar elongated virtually perpendicular to the line of nodes dominates. When analyzing the azimuthally

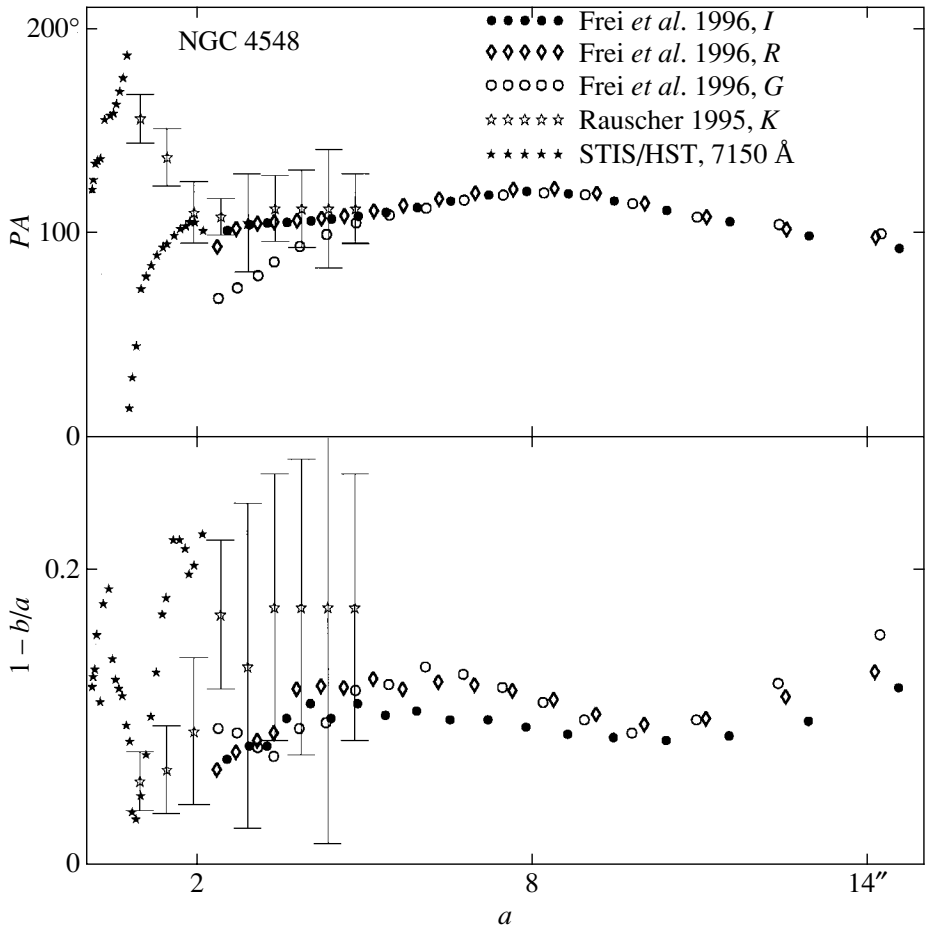

Fig. 4. The morphological characteristics of isophotes, the major-axis position angle and ellipticity, at the center of NGC 4548, as derived from various photometric data.

averaged brightness profile in the outer parts, we obtained an exponential global-disk scale length of 62.8″, which significantly exceeds the value of 28.7″ in Baggett *et al.* (1998). When we subtracted the model of an exponential disk with the line of nodes at $PA = 148°$, an inclination of 38°, and our derived parameters of the radial brightness profile from the actual digital images of NGC 4548 taken from the Atlas by Frei *et al.* (1996), the residual brightnesses in the radial range 2.4″–20″ excellently fitted into a de Vaucouleurs law with $r_e = 24''$ [Baggett *et al.* (1998) give $r_e = 36.7''$]. The K (2 mkm) band brightness profile of NGC 4548 within $R \approx 6''$ obtained by Rauscher (1995) also obeys the de Vaucouleurs law. Finally, in their photometric survey, where the galaxy images were decomposed into a disk and a bulge with an arbitrary brightness profile, Gavazzi *et al.* (2000) also pointed out that a bulge with a de Vaucouleurs brightness profile was found in NGC 4548 in the H (1.6 mkm) band. Thus, although the bulge of NGC 4548 is triaxial, it has a young stellar population and is, probably, a product of the secular evolution of the galaxy with a global bar; nevertheless, it exhibits a classical de Vaucouleurs brightness profile. This is an unexpected result that is in conflict with some theoretical predictions.

DISCUSSION

Having measured the indices (equivalent widths) of magnesium and iron absorption lines in the nucleus and circumnuclear region of NGC 4548, we found an unresolved chemically decoupled nucleus in this galaxy. However, it proved to bear no resemblance to all the previously studied chemically decoupled nuclei and most likely stems from the fact that we investigate a galaxy with a thin, high-contrast large-scale bar for the first time.

First of all, the nuclear stellar population in NGC 4548 shows a record high metallicity: it is a factor of 4 higher than the solar one. The structure of the decoupled nucleus itself is, probably, conventional: according to the HST data, a compact stellar disk whose plane coincides with the principal

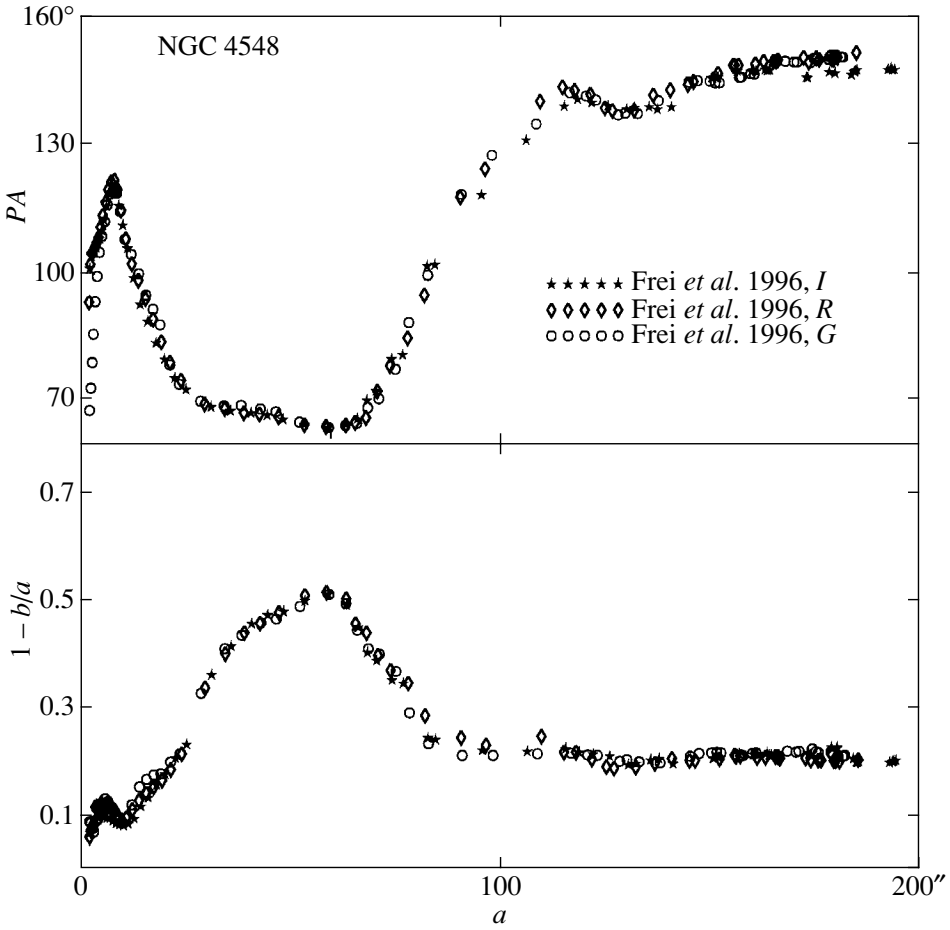

Fig. 5. The morphological characteristics of isophotes, the major-axis position angle and ellipticity, in NGC 4548 on large scales, as derived from the photometric data by Frei *et al.* (1996).

galactic symmetry plane can be seen within 0.4″ (∼33 pc). The stars in this disk rotate in circular orbits. However, the conventional circumnuclear stellar disk is embedded in quite an unusual bulge: although its stars are, on average, a factor of 2.5 less metal-rich than those in the nucleus (which still implies a mean metallicity higher than the solar one), the mean age of the stellar population is the same or younger than that in the nucleus, less than 5 Gyr. This implies that the central star-formation burst that occurred several Gyr ago encompassed an extended circumnuclear territory; the fact that the nucleus turned out to be chemically decoupled and to have an enhanced Mg/Fe ratio suggests a shorter time scale and a higher star-formation efficiency in the circumnuclear disk that those in the bulge region distended in all directions. This behavior of the circumnuclear star-formation burst may stem from the fact that the large-scale bar intensively supplied the nucleus with fuel for the burst, providing an inflow of gas with a large angular momentum from the outer global disk. Interestingly, the rejuvenated bulge is slightly triaxial and has a classical de Vaucouleurs brightness profile, whereas the calculations of models for the secular evolution, a gradual bulge formation over a period of several Gyr through radial gas inflow, generally yield quasi-exponential profiles (Courteau *et al.* 1996). It may well be that this is evidence of the bursting rather than a monotonic event that determined the bulge structure.

Finally, note the unusual kinematics of the ionized gas within 200–250 pc of the galactic center. The kinematic major axis of its velocity field, the direction of the maximum line-of-sight velocity gradient, is perpendicular to the kinematic major axis of the stellar velocity field and to the line of nodes of the global galactic disk. Theoretically, this is possible in two cases: either the gas lies in the galactic symmetry plane but has only purely radial motions or it regularly rotates in a plane that does not coincide with the global-disk plane. The former situation seems unlikely. Radial gas motions are usually produced either by the bar or (much weaker) by the spiral arms. There is no minibar at the center of NGC 4548: we

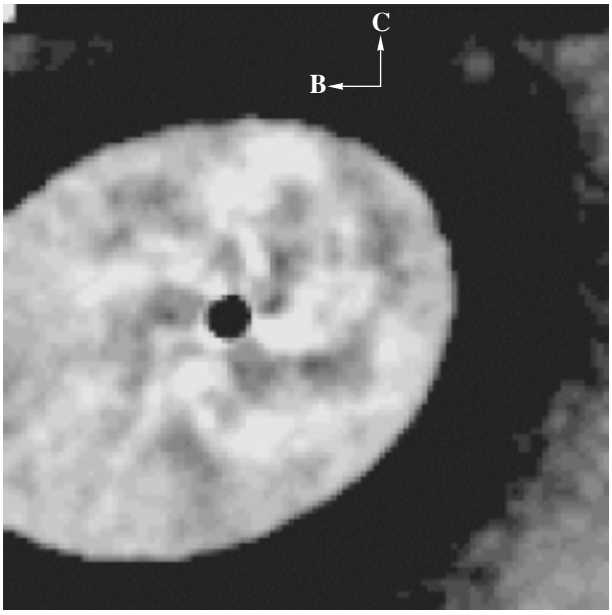

Fig. 6. The residual-brightness map for NGC 4548 in a λ 7150 Å (STIS HST) filter after the subtraction of a model with purely elliptical isophotes: the position angle of the vertical line is 17°, and the total region size is $5'' \times 5''$. We did not subtract the model at the very center (painted black); the light ellipse encloses the region in which the model was subtracted.

made sure in the preceding section that the stars within $R \approx 3''$ are distributed and rotate axisymmetrically. There are spiral arms, though: Fig. 6 shows the residual-brightness map for NGC 4548 obtained with the STIS/HST instrument after the subtraction of a model distribution with purely elliptical isophotes; a four-arm spiral pattern is clearly seen on this map within 1.5″ of the center. However, the perturbed velocities introduced by the spiral pattern generally do not exceed 20–30 km s^{-1}; in contrast, being a dynamically cold subsystem, the gas must rotate, judging by the stellar rotation, with a velocity no less than 50 km s^{-1} at 2″–3″. If the amplitudes of the radial and tangential gas velocities are comparable, then the kinematic major axis will turn through a mere 45°; in order that this axis turn through an apparent angle of 90°, the radial gas velocities at the center of NGC 4548 must exceed the rotational component at least by an order of magnitude. Bearing in mind the regular morphology and the absence of any nuclear activity in NGC 4548, such radial motions seem implausible. It remains to assume that the gas at the center of NGC 4548 rotates in an inclined plane. We cannot prove that this plane is exactly polar, as long as we have no confirmation in the form of morphological evidence based on a blue map with a high spatial resolution. However, given the reasoning concerning bars and presented in the Introduction, the fact that the circumnuclear gaseous disk in NGC 4548 is polar seems highly likely.

ACKNOWLEDGMENTS

I wish to thank V.L. Afanasiev, V.V. Vlasyuk, and S.N. Dodonov from the Special Astrophysical Observatory (Russian Academy of Sciences) for help with the 6-m telescope observations. The observational data used here were obtained with the 6-m telescope financed by the Ministry of Science of the Russian Federation (registration no. 01-43). We also partly used data from the NASA/ESA Hubble Space Telescope operated by the Association of Universities for Studies in Astronomy under contract with the NASA (NAS 5-26555). We also relied on the LEDA database provided by the LEDA team at the CRAL Lyon Observatory (France). This study was supported by the Russian Foundation for Basic Research (project no. 98-02-16196) and the Russian State Science and Technology Program "Astronomy. Fundamental Space Research" (Astronomy Section) (project no. 1.2.4.1).

REFERENCES

1. V. L. Afanasiev, V. V. Vlasyuk, S. N. Dodonov, and O. K. Sil'chenko, Preprint No. 54, SAO RAN (1990).
2. W. E. Baggett, S. M. Baggett, and K. S. J. Anderson, Astron. J. **116**, 1626 (1998).
3. F. Bertola, L. M. Buson, and W. W. Zeilinger, Astrophys. J. Lett. **401**, L79 (1992).
4. F. Bertola, P. Cinzano, E. M. Corsini, *et al.*, Astrophys. J. Lett. **448**, L13 (1995).
5. S. Courteau, R. S. de Jong, and A. H. Broeils, Astrophys. J. Lett. **457**, L73 (1996).
6. Z. Frei, P. Guhathakurta, J. E. Gunn, and J. A. Tyson, Astron. J. **111**, 174 (1996).
7. D. Friedli and W. Benz, Astron. Astrophys. **268**, 65 (1993).
8. G. Gavazzi, P. Franzetti, A. Boselli, *et al.*, Astron. Astrophys. **361**, 863 (2000).
9. V. A. Hagen-Thorn and V. P. Reshetnikov, Astron. Astrophys. **319**, 430 (1997).
10. A. V. Moiseev and V. V. Mustsevoĭ, Pis'ma Astron. Zh. **26**, 657 (2000) [Astron. Lett. **26**, 565 (2000)].
11. G. Monnet, R. Bacon, and E. Emsellem, Astron. Astrophys. **253**, 366 (1992).
12. B. J. Rauscher, Astron. J. **109**, 1608 (1995).
13. O. K. Sil'chenko, Pis'ma Astron. Zh. **19**, 693 (1993) [Astron. Lett. **19**, 279 (1993)].
14. O. K. Sil'chenko, Astron. Zh. **71**, 706 (1994) [Astron. Rep. **38**, 624 (1994)].
15. O. K. Sil'chenko, Astron. Astrophys. **330**, 412 (1998).
16. O. K. Sil'chenko, Astron. J. **120**, 741 (2000).
17. O. K. Sil'chenko and V. L. Afanasiev, Astron. Astrophys. **364**, 479 (2000).

18. O. K. Sil'chenko, V. L. Afanasiev, and V. V. Vlasyuk, Astron. Zh. **69**, 1121 (1992) [Sov. Astron. **36**, 577 (1992)].
19. O. K. Sil'chenko, V. V. Vlasyuk, and A. N. Burenkov, Astron. Astrophys. **326**, 941 (1997).
20. Y. Sofue and K.-I. Wakamatsu, Astron. J. **107**, 1018 (1994).
21. R. Tantalo, C. Chiosi, and A. Bressan, Astron. Astrophys. **333**, 419 (1998).
22. A. Vazdekis, E. Casuso, R. F. Peletier, and J. E. Beckman, Astrophys. J., Suppl. Ser. **106**, 307 (1996).
23. V. V. Vlasyuk, Izv. SAO **36**, 107 (1993).
24. B. C. Whitmore, R. A. Lucas, D. B. McElroy, *et al.*, Astron. J. **100**, 1489 (1990).
25. G. Worthey, Astrophys. J., Suppl. Ser. **95**, 107 (1994).
26. G. Worthey, S. M. Faber, J. J. Gonzalez, and D. Burstein, Astrophys. J., Suppl. Ser. **94**, 687 (1994).
27. A. V. Zasov and O. K. Sil'chenko, Astron. Zh. **74**, 824 (1997) [Astron. Rep. **41**, 734 (1997)].

Translated by V. Astakhov

Astronomy Letters, Vol. 28, No. 4, 2002, pp. 217–222. Translated from Pis'ma v Astronomicheskiĭ Zhurnal, Vol. 28, No. 4, 2002, pp. 253–259.

A Possible Formation Mechanism of the Asymmetry in the H_2O Maser Emission Line

N. A. Silant'ev[1,2], E. E. Lekht[1,3*], J. E. Mendosa-Torres[1], and A. M. Tolmachev[4]

[1] *Instituto Nacional de Astrofísica, Óptica y Electrónica, Luis Enrique Erro No. 1, Apdo Postal 51 y 216, 72840 Tonantzintla, Puebla, México*

[2] *Pulkovo Astronomical Observatory, Russian Academy of Sciences, Pulkovskoe sh. 65, St. Petersburg, 196140 Russia*

[3] *Sternberg Astronomical Institute, Universitetskii pr. 13, Moscow, 119899 Russia*

[4] *Pushchino Radio Astronomy Observatory, Astrospace Center, Lebedev Physical Institute, Russian Academy of Sciences, Pushchino, Moscow oblast, 142292 Russia*

Received November 21, 2001

Abstract—We present a possible formation mechanism of the asymmetry in the maser emission line of H_2O sources associated with star-forming regions. Observations with the RT-22 radio telescope at the Pushchino Radio Astronomy Observatory are used. We analyze the line profiles of emission features in the sources G43.8–0.1, NGC 2071, and ON1. If the line is asymmetric, the left (low-velocity) wing is higher than the right wing. The proposed mechanism accounts for the observed asymmetry and makes it possible to estimate some physical parameters of the medium in the vicinity of a maser spot. © *2002 MAIK "Nauka/Interperiodica".*

Key words: *star-forming regions, interstellar molecules, maser radio sources*

INTRODUCTION

In general, the observed cosmic maser emission of water-vapor molecules is a superposition of individual emission features with different intensities and widths. The features can be taken as single ones during flares, when their intensity is much higher than that of the blending components. Observations show that in most cases, such features have a symmetric line shape. In some cases, a blending is possible even during very strong flares (Matveyenko 1981). Single features with an asymmetric line shape are more rare. The cause of the line asymmetry may be the maser geometry, i.e., the existence of density and velocity nonuniformities in the maser spot.

Another probable cause of the asymmetry was considered for the source S269, which is most likely identified with a protoplanetary disk. Such a maser may be considered as a superposition of spherical and cylindrical masers. The spherical maser, which is an inhomogeneous rotating vortex, is located in the red amplification corridor of the Keplerian disk. Because of the nonlinear variation in the velocity of H_2O molecules with an inverse population in the amplification corridor, a line asymmetry arises (Lekht *et al.* 2001).

Yet another mechanism that accounts for the line asymmetry of individual emission peaks in H_2O maser sources associated with star-forming regions was proposed by Lekht *et al.* (2002). The idea is that the emission of a maser spot undergoes selective absorption in the layer of material adjacent to the spot. In this model, the maser spot moves toward the observer relative to the star at a higher velocity than does the adjacent layer; i.e., the maser spot (condensation) catches up with the layer of material and compresses it. In this case, the left (low-velocity) line wing is higher than the right wing.

In this paper, based on the monitoring of H_2O maser sources associated with star-forming regions, we developed our model.

DATA PRESENTATION

We chose the spectra of the water-vapor maser sources G43.8–0.1, NGC 2071, and ON1 in those periods when some individual emission features had an asymmetric line shape. The spectra were obtained with the RT-22 radio telescope at the Pushchino Radio Astronomy Observatory. The spectral resolution of the filter-bank analyzer at 22 GHz was 0.101 km s^{-1}. The radio telescope, instrumentation,

*E-mail: lekht@inaoep.mx,lekht@.sai.msu.ru

1063-7737/02/2804-0217$22.00

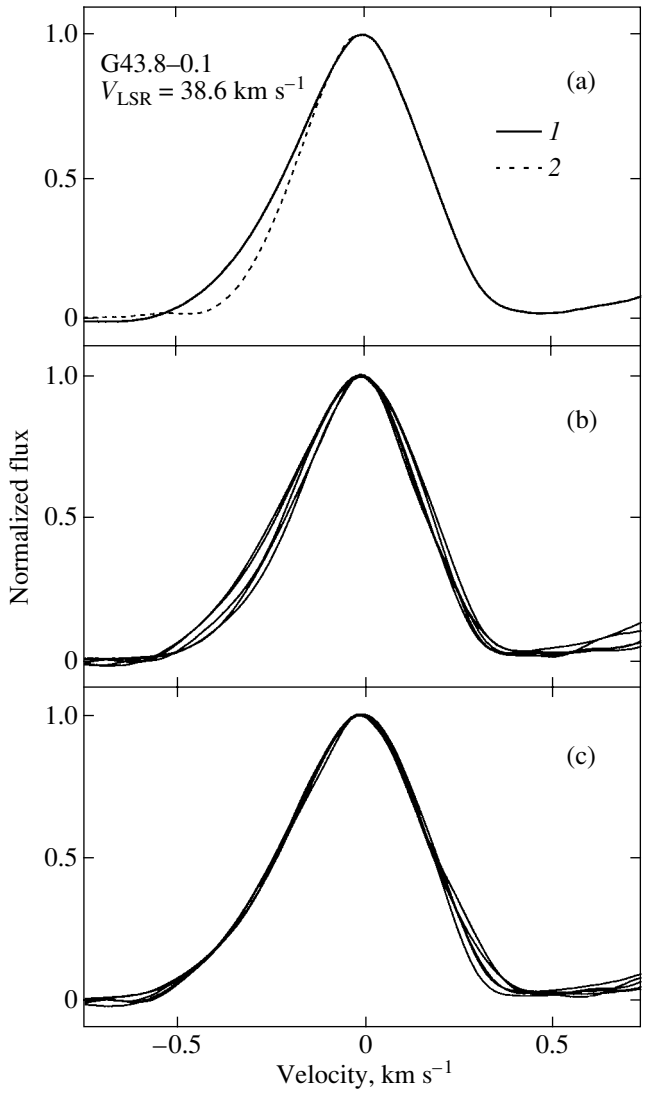

Fig. 1. An average normalized H_2O line profile of the 1981–1982 flare in G43.8–0.1 at a radial velocity of 38.6 km s^{-1} (a) and a superposition of the profiles normalized in amplitude (b) and width (c).

and observing techniques were described in greatest detail by Sorochenko *et al.* (1985). Our data reduction techniques used for single features were described by Lekht *et al.* (2002).

Figure 1a shows an average H_2O line profile of the maser G43.8–0.1 for the strong flare at a radial velocity of 38.6 km s^{-1} (*1*) observed from October 1981 through May 1982. A mirror image of the right line wing was constructed (*2*). All the line profiles of this period were first normalized in flux (Fig. 1b). Figure 1c shows these profiles reduced to the same width. The normalization was performed at a line half-maximum level. We see a close coincidence of the profiles, particularly of the left line wings, which is of greatest importance to us. This suggests a close similarity between the observed line profiles of the flare at 38.6 km s^{-1}.

Figure 2a shows the H_2O line profiles of NGC 2071 for September–December 1986. The mean radial velocity was 12.2 km s^{-1}. Since the flux was highly variable, to compare the line profiles at different epochs, we normalized them in amplitude and aligned them in velocity (Fig. 2b). The alignment is necessary, because we observed a radial-velocity drift of the emission feature. In addition, the random errors and the errors in the radial velocities were eliminated. Figure 2c shows an average curve for the normalized lines (*1*) and a fitted Gaussian (*2*). The difference between the curves is insignificant, being concentrated mainly in the line wings.

Figure 3 shows temporal variations in the radial velocity, width, and asymmetry of the line. The asym-

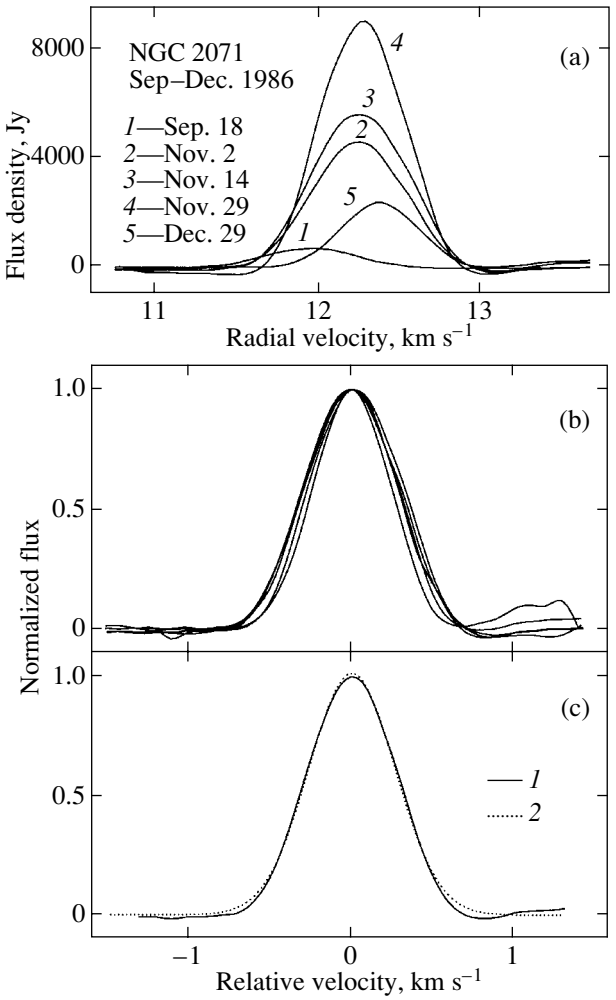

Fig. 2. (a) H_2O line profiles of the flare feature in NGC 2071 at 12.2 km s^{-1}; (b) a superposition of the lines normalized in flux and aligned in velocity; (c) an averaged line (*1*) and a fitted Gaussian (*2*).

metry was defined as

$$\eta(V) = \frac{I_R(U) - I_L(U)}{I_{mean}(U)} \equiv \frac{I_R(U) - I_L(U)}{0.5[I_R(U) + I_L(U)]}. \quad (1)$$

Here, the intensities of the right (I_R) and left (I_L) wings and the mean intensity I_{mean} were taken at point U counted off from the line peak. The parameter η was measured at the line half-width.

Figure 4 shows averaged line profiles of the emission feature at 15 km s^{-1} (*1*) in the H_2O spectrum of ON1 for two different periods. To show the asymmetry, we plotted a mirror image of the right line wing (*2*).

Figure 5 shows a possible model of the maser spot associated with the 1982 flare in G43.8–0.1, and Fig. 6 demonstrates the action of the mechanism responsible for the line asymmetry.

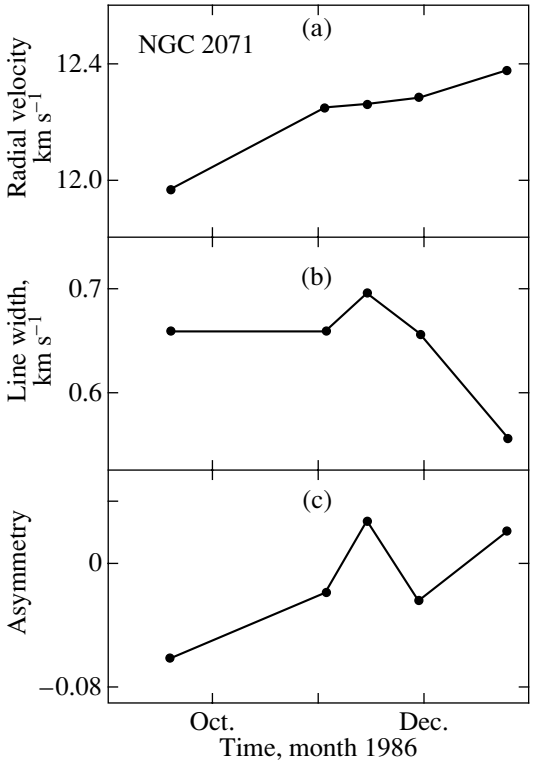

Fig. 3. Variations in the (a) radial velocity, (b) line width, and (c) line asymmetry of the emission feature at 12.2 km s^{-1} in NGC 2071.

DISCUSSION

The Source G43.8-0.1

During the 1981–1982 flare, the line was narrow: its minimum width was 0.35 and its mean width was 0.4 km s^{-1}. The line had an asymmetric shape (Fig. 1). The flare duration was estimated to be six or seven months. Below, we single out the main characteristics of the observed line.

(1) No radial-velocity drift was observed.

(2) There was a correlation between the flux and line-width variations (Lekht 2000), which is characteristic of an unsaturated maser (Mattila *et al.* 1985).

(3) The left line wing was greatly raised relative to the right wing, with the asymmetry being preserved in all H_2O spectra.

(4) Despite the line-width variations, the profile similarity was unchanged.

The absence of any drift implies that there is no accelerated motion of the masing region. In some cases, a strong flare can be produced by the passage of a shock wave through a region with a radial-velocity gradient. In this case, there is a radial-velocity drift. Since the 38.6-km s^{-1} feature exhibits no drift, the maser spot has no appreciable velocity gradient.

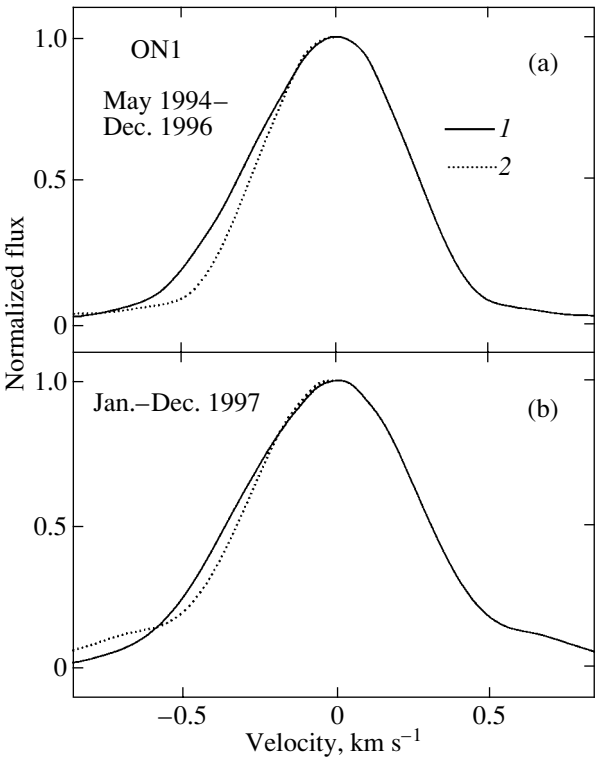

Fig. 4. (a) An average normalized H_2O line profile of the emission feature at 15 km s^{-1} (*1*) in the source ON1 from May 1994 through December 1996; (b) the same for all the 1997; (*2*) the dotted lines represent the mirror images of the right line wings.

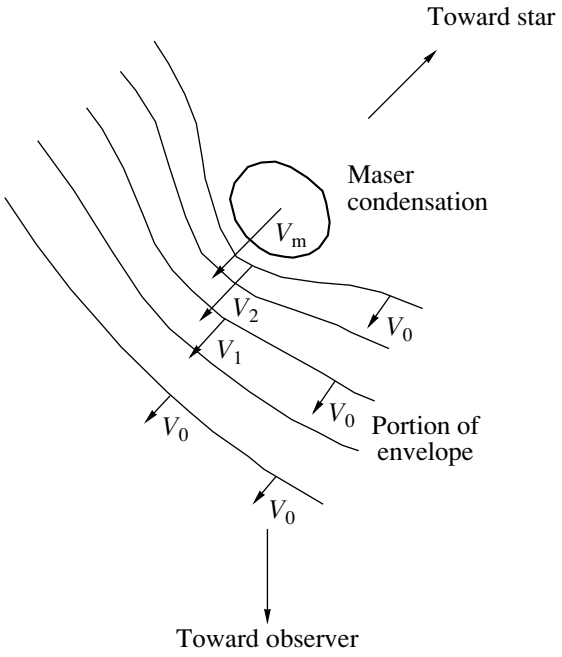

Fig. 5. A possible model of the maser spot associated with the 1982 flare in G43.8–0.1.

The line-width variations are caused by the properties of the unsaturated maser and are, most likely, unrelated to the geometry of the maser spot, i.e., to its internal structure. The line asymmetry can be most easily attributed to a superposition of the emissions from two components. However, the observed similarity of the asymmetric line as its width varies rejects this possibility. The asymmetry, probably, arises on the propagation path of the maser emission.

The Source NGC 2071

Recall that according to Torrelles *et al.* (1998), there are two groups of maser spots in this region associated with compact H II regions and with the infrared sources IRS1 and IRS3. One of these regions located near IRS1 is elongated along the jet. The other group of spots associated with IRS3 forms a rotating protoplanetary disk. The disk plane is perpendicular to the jet axis. The angular separation between the groups of spots is less than 6″. This information is necessary for interpreting the data, because the RT-22 radio telescope receives the emission from both sources.

Below, we list the main characteristics of the 1986 flare at $V_{LSR} = 12.2$ km s^{-1}.

(1) There was a radial-velocity drift of the feature during a fairly short period (3.5 months). The drift was 0.4 km s^{-1} in magnitude.

(2) The line width varied over the range 0.55–0.7 km s^{-1}. We found no correlation with the flux.

(3) On September 29, 1986, the line asymmetry was 6%. In the remaining cases, the measured asymmetry changed sign, but these variations did not exceed the measurement errors.

(4) The average line profile is symmetric and nearly Gaussian in shape. The largest differences are concentrated in the line wings and are insignificant at its peak.

A line drift in the H_2O spectrum can take place in the case of an actual variation in the maser condensation velocity. A different model is also possible. A shock wave propagates in a medium with a radial-velocity gradient, successively exciting different layers of this medium. As a result, the masing region will displace in space, and the emitted line will have a drift in the spectrum. Since the line-width variability does not correlate with the flux, the probable cause of the line-width variation can be an inhomogeneity of the medium. For this reason, preference should be given to the latter model. In our view, the variability pattern of the line shape also confirms this model.

The 1988 flare at a radial velocity of 12.2 km s^{-1} most likely occurred in the group of maser spots associated with the jet (IRS1).

The Source ON1

Lekht *et al.* (2002) have shown that, despite the line-width and flux variations, the line asymmetry was preserved. According to the model of the H_2O maser in ON1 (Lekht *et al.* 1995), the emission feature responsible for this emission is located at the envelope side closest to the observer and has a radial motion relative to the central star.

As in the case of G43.8–0.1, we may assume that there is a compressed layer of gas (without inverse level populations of water-vapor molecules) with a slightly higher radial velocity in front of the maser spot. In this case, the effect is weaker, because the spot is located on the envelope periphery (Lekht *et al.* 1995).

The Mechanism Responsible for the Line Asymmetry

According to present views, the groups of maser spots can be associated with a protoplanetary disk, a jet, or an envelope around the forming star. The separation of masers into protoplanetary disks and envelopes is, to some extent, arbitrary. In both cases, there can be a radial motion of the masing region driven by stellar wind and its rotation in the stellar gravitational field (Matveyenko *et al.* 2000; Lekht *et al.* 1995).

To explain the line asymmetry observed in the sources G43.8–0.1 and ON1, which are associated with a shell structure, we propose the following model. A maser condensation driven by stellar wind moves radially away from the star and rakes up a layer of gas with noninverse level populations of water molecules in front of it. As a result of this interaction, the gas in the layer adjacent to the maser condensation is compressed (Fig. 5). This causes an increase in its density and a redistribution of molecules in radial velocity, which gives rise to a velocity gradient. The resulting velocity of the layer V_s will be slightly lower than the condensation velocity, i.e., $V_d = V_m - V_s \gtrsim 0$, where V_d is the approach velocity of the condensation and the layer.

The appearance of a sufficient number of molecules with velocities close (but not equal) to the velocity of the maser condensation results in selective absorption of the maser emission: the high-velocity wing of the maser line will undergo a stronger absorption than the low-velocity wing.

We see from Figs. 1 and 4 that the maximum asymmetry is observed in the source G43.8–0.1. At the line half-width, it is 15%. To calculate the probable asymmetry, let us write the solution of the radiative transfer equation as

$$I(V) = I(0)e^{-\left(\frac{2V}{\delta V_m}\right)^2} \exp\left[-\tau_0 e^{-\left(\frac{2(V-V_d)}{\delta V_T}\right)^2}\right], \quad (2)$$

where $I(0)e^{-\left(\frac{2V}{\delta V_m}\right)^2}$ is the intensity of the emission emerging from the maser condensation as a function of velocity V and δV_m is the line width of this emission. The last factor in Eq. (2) gives the absorption in the compressed layer of gas. Here, τ_0 is the optical depth of the layer with noninverse level populations (at velocity V_d), δV_T is the molecular velocity dispersion in the layer, which is determined mainly by the thermal motion of molecules.

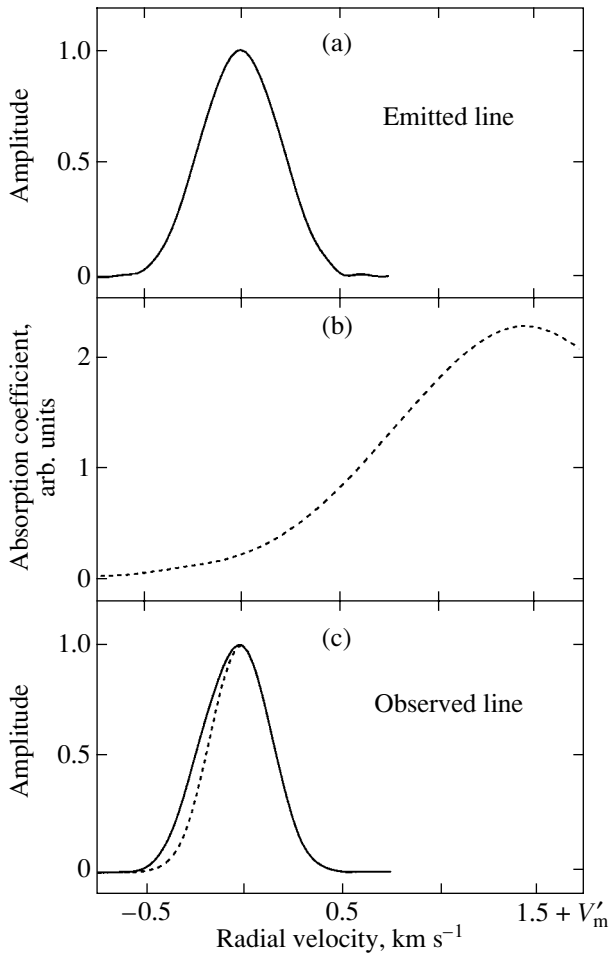

Fig. 6. Action of the mechanism responsible for the line asymmetry. (a) The emission line at the exit of the maser spot and (c) the observed line; (b) a possible profile of the absorption coefficient in the vicinity of the maser spot with allowance for the velocity and density gradients; V'_m is the radial velocity of the maser spot.

The degrees of asymmetry in %

$\delta V_m/\delta V_T$	$\tau_0 = 1$	2	3	4
0.5	2	5	6	8
0.6	4	7	8	11
0.7	5	10	12	15
0.8	7	13	16	20
0.9	9	17	20	24
1	11	20	25	28

The calculations with formulas (1) and (2) show that line asymmetry η depends on three dimensionless parameters: $\delta V_m/\delta V_T$, τ_0, and $V_d/\delta V_T$. The dependence on the first two parameters is strongest. Since the dependence of the asymmetry on the third parameter is weaker, we assumed that $V_d/\delta V_T \approx 1$. Our calculations for various values of the above parameters are presented in the table.

It follows from the table that the asymmetry observed in G43.8–0.1 (15%) can be obtained for different optical depths τ_0. It should be noted that a certain gas kinetic temperature T_k corresponds to each velocity dispersion δV_T. A colder gas requires a smaller τ_0. The actual gas kinetic temperature in the compressed layer can be within the range 100–200 K. The optical depth of such a layer must be 3–4.

All our calculations were performed for a radial motion. In the actual case of G43.8–0.1 (Lekht and Sorochenko 1999), it is necessary to make a correction for the projected motion. This will result either in a small increase of the layer optical depth or in a decrease of its kinetic temperature. For ON1, the observed line asymmetry is smaller. This is most likely because the maser spot with $V_{LSR} = 15$ km s^{-1} is located closer to the envelope periphery. The asymmetric line in ON1 is broader than that in G43.8–0.1. The larger line-width (0.6 versus 0.4) suggests a hotter gas in the layer. However, the peripheral location of the maser spot, on the contrary, requires a lower temperature. As a result, the most appropriate value for the layer with noninverse level populations of H_2O molecules is $T_k \approx 100$–200 K.

CONCLUSIONS

We have analyzed individual H_2O emission features in the maser sources G43.8–0.1, NGC 2071, and ON1 and suggested a mechanism responsible for the asymmetry of the observed lines. Below, we summarize our main results.

(1) For G43.8–0.1 and ON1, we observed a line asymmetry of the same sign: the left (low-velocity) line wing is higher than the right wing. The degree of asymmetry ranges from 8 to 15%, depending on the source and the date of observations.

(2) The asymmetry mechanism is the passage of the maser emission through the layer of gas adjacent to a maser condensation with noninverse level populations of H_2O molecules. The layer is compressed by the moving condensation.

(3) The numerical value of the line asymmetry allows us to estimate the optical depth of the layer, its kinetic temperature, and the relative velocity of the maser condensation and this layer.

(4) The line-asymmetry variations in NGC 2071 appear to be attributable to a drift of the masing region in an inhomogeneous medium. The 12.2 km s^{-1} feature responsible for this emission is most likely located in the group of maser spots associated with the jet (the source IRS1).

ACKNOWLEDGMENTS

This work was supported by the Ministry of Information of the Russian Federation (RT-22 radio telescope; registration no. 01-10) and the Russian Foundation for Basic Research (project no. 99-02-16293). We are grateful to the staff of the Pushchino Radio Astronomy Observatory for help with the observations.

REFERENCES

1. E. E. Lekht, Astron. Astrophys., Suppl. Ser. **141**, 185 (2000).
2. E. E. Lekht and R. L. Sorochenko, Astron. Zh. **76**, 758 (1999) [Astron. Rep. **43**, 663 (1999)].
3. E. E. Lekht, J. E. Mendoza-Torres, and R. L. Sorochenko, Astron. Zh. **72**, 39 (1995) [Astron. Rep. **39**, 34 (1995)].
4. E. E. Lekht, N. A. Silant'ev, J. E. Mendoza-Torres, *et al.*, Astron. Astrophys. **377**, 999 (2001).
5. E. E. Lekht, N. A. Silant'ev, J. E. Mendoza-Torres, and A. M. Tolmachev, Pis'ma Astron. Zh. **28**, 106 (2002).
6. K. Mattila, N. Holsti, M. Toriseva, *et al.*, Astron. Astrophys. **145**, 192 (1985).
7. L. I. Matveyenko, Pis'ma Astron. Zh. **7**, 100 (1981) [Astron. Lett. **7**, 54 (1981)].
8. L. I. Matveyenko, P. J. Daimond, and D. A. Graham, Astron. Zh. **77**, 669 (2000) [Astron. Rep. **44**, 592 (2000)].
9. R. L. Sorochenko, M. M. Berulis, V. A. Gusev, *et al.*, Tr. Fiz. Inst. Akad. Nauk SSSR **159**, 50 (1985).
10. J. M. Torrelles, J. F. Gómes, L. F. Rodrígues, *et al.*, Astrophys. J. **505**, 756 (1998).

Translated by G. Rudnitskii

Astronomy Letters, Vol. 28, No. 4, 2002, pp. 223–236. Translated from Pis'ma v Astronomicheskiĭ Zhurnal, Vol. 28, No. 4, 2002, pp. 260–275.

Searches for the Shell Swept up by the Stellar Wind from Cyg OB2

T. A. Lozinskaya[1]*, V. V. Pravdikova[1], and A. V. Finoguenov[2]

[1] *Sternberg Astronomical Institute, Universitetskii pr. 13, Moscow, 119899 Russia*

[2] *Space Research Institute, Russian Academy of Sciences, ul. Profsoyuznaya 84/32, Moscow, 117810 Russia*

Received October 2, 2001

Abstract—We investigated the kinematics of ionized gas in an extended ($20° \times 15°$) region containing the X-ray Superbubble in Cygnus with the aim of finding the shell swept up by a strong wind from Cyg OB2. Hα observations were carried out with high angular and spectral resolutions using a Fabry–Perot interferometer attached to the 125-cm telescope at the Crimean Observatory of the Sternberg Astronomical Institute. We detected high-velocity gas motions, which could result from the expansion of the hypothetical shell at a velocity of 25–50 km s^{-1}. Given the number of OB stars increased by Knödlseder (2000) by an order of magnitude, Cyg OB2 is shown to possess a wind that is strong enough [$L_w \simeq (1–2) \times 10^{39}$ erg s^{-1}] to produce a shell comparable in size to the X-ray Superbubble and to a giant system of optical filaments. Based on our measurements and on X-ray and infrared observations, we discuss possible observational manifestations of the shell swept up by the wind. © *2002 MAIK "Nauka/Interperiodica"*.

Key words: *star clusters and associations, interstellar medium, stellar wind*

INTRODUCTION

The studies of Cyg OB2 by Reddish *et al.* (1966) showed it to be a Galactic association that is unique in compactness and in the density of massive early-type stars. The question of where the shell swept up by the wind from this compact grouping of young stars was raised long ago. As such a shell, different authors considered the following: a system of optical filaments, 15° in size (Ikhsanov 1960; Dickel *et al.* 1969); the inner (relative to it) system of filaments, 8°–10° in size, elongated across the Galactic plane (Bochkarev and Sitnik 1985); the diffuse component of the Cygnus X radio source (Wendker 1970); the Cyg 4 or Cyg 5 gas–dust shells from the list by Brand and Zealey (1975); and the giant X-ray Superbubble in Cygnus (Cash *et al.* 1980). This list of possibilities is not yet complete.

Recently, the data on the Cyg OB2 stellar population have been radically changed. Having added stars previously hidden due to strong absorption, Knödlseder (2000) increased the number of members and the total mass of the object by an order of magnitude. As a result, the author classified this star grouping as a young globular cluster similar to the numerous blue globular clusters in the Large Magellanic Cloud (LMC), but it is the only one identified in the Galaxy so far. Currently, Cyg OB2 numbers ~120 O-type stars, which forces us to significantly (by an order of magnitude; see Section 3) increase the flux of ionizing radiation and the mechanical luminosity of the stellar wind and makes the searches for the swept-up shell around Cyg OB2 even more urgent.

The nature of the X-ray Superbubble in Cygnus and its relationship to Cyg OB2 have been discussed repeatedly. The observations published before 1984 were analyzed in detail by Bochkarev and Sitnik (1985). Uyaniker *et al.* (2001) carried out new radio continuum observations and comprehensively analyzed currently available observational data for the region in the X-ray and infrared bands and in molecular radio lines. The same conclusion was reached in the two studies: the Cygnus Superbubble is not a physical unity but is the sum of emissions from physically unrelated objects located at distances from 0.5 to 3.5 kpc.

Here, we pose the question from a different angle. There is no doubt that a superposition of the X-ray, optical, infrared, and radio emissions from objects located at different distances along the spiral arm is observed in the Cygnus region. Nevertheless, Cyg OB2 is a compact star grouping that, probably, possesses the strongest stellar wind in the Galaxy whose action has continued for $\approx(2-3) \times 10^6$ yr. In that case, where is the evidence for the action of this wind on the ambient interstellar gas in the first place? If none of the objects mentioned above can be identified as the shell swept up by the Cyg OB2 wind, then what must be the parameters of the ambient interstellar medium for such a shell to be unobservable?

*E-mail: lozinsk@sai.msu.ru

1063-7737/02/2804-0223$22.00

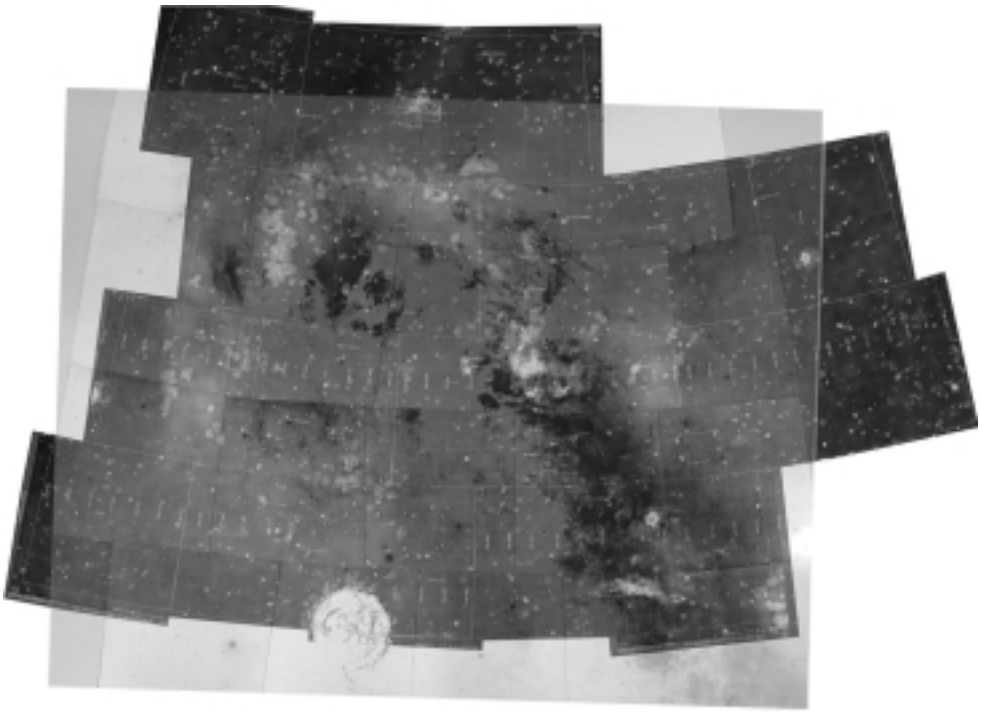

Fig. 1. Overall X-ray and optical structure of the Superbubble region in Cygnus. The shades of light gray indicate the X-ray (0.4–2.4 keV) brightness distribution with a high resolution obtained from the ROSAT archival data. The shades of dark gray indicate an optical photograph of the region (a mosaic of 19 Palomar Sky Survey red prints).

In attempting to detect the swept-up shell, we investigated the radial-velocity field of the ionized gas in an extended ($20^\circ \times 15^\circ$) region using our Hα observations with a Fabry–Perot interferometer attached to the 125-cm telescope at the Crimean Observatory of the Sternberg Astronomical Institute (SAI).

In Section 1, the X-ray image constructed from the ROSAT archival data is compared with an optical image of the entire region under study. Our interferometric observations are presented in Section 2: we describe the observing and data reduction techniques; construct the radial-velocity distribution of the ionized gas in the region; and reveal the velocities that could be attributable to an expansion of the shell swept up by the wind. In Section 3, based on the possible expansion velocity of the hypothetical shell we found and on currently available optical, X-ray, infrared, and radio observational data, we attempted to find morphological manifestations of this shell. Our conclusions are briefly summarized in the last section.

1. A COMPLETE X-RAY AND OPTICAL IMAGE OF THE REGION UNDER STUDY

An image of the entire region under study, including the X-ray Superbubble in Cygnus and the giant system of optical nebulae, is shown in Fig. 1.

The high-resolution X-ray brightness distribution was constructed from the ROSAT observational data. For imaging, we used archival data from the ROSAT all-sky survey in three energy bands: 0.11–0.40, 0.40–1.0, and 1.0–2.4 keV. (The charged particle background was removed from these images.) Figure 1 shows the total emission in the three energy bands. Our data reduction revealed the dominance of the 0.4–1.0 keV emission from the Superbubble. The complete X-ray image for the $25^\circ \times 22^\circ$ region is a mosaic of 18 separate fields.

The optical emission distribution in the region superimposed on the X-ray distribution is a mosaic map constructed from 19 Palomar Sky Survey red prints. The optical emission is represented by the giant system of diffuse and thin-filament nebulae in the region with $\mathrm{RA} = 19^\mathrm{h}30^\mathrm{m} \ldots 21^\mathrm{h}50^\mathrm{m}$, $\mathrm{D} = 30^\circ \ldots 47^\circ$; $l = 70^\circ \ldots 88^\circ$, $b = -8^\circ \ldots +5^\circ$.

As Fig. 1 shows, the giant system of optical filaments and the X-ray Superbubble as a whole closely coincide in the plane of the sky, considering that their emission is produced by plasma with a distinctly different temperature.

2. IONIZED-GAS VELOCITIES IN THE REGION

2.1. Observations and Data Reduction

In attempting to identify the shell produced by the Cyg OB2 wind, we analyzed in detail the radial-velocity field by using the Hα emission of the ionized

gas in this most complex region of the Local spiral arm.

We measured the radial velocities in Hα using a Fabry–Perot interferometer with a focal reducer on the 125-cm telescope at the Crimean Observatory of the SAI.

The observing program for this giant region was initiated in 1991. The detector was an image intensifier before 1994 and an ST-6 242 × 378-pixel CCD array after 1994.

An interference filter centered on Hα with a FWHM of 25 Å was used to premonochromatize the emission. The actual spectral resolution of the interferometer corresponded to $\simeq$15 km s^{-1}; the dispersion region (the radial-velocity range free from an overlapping of adjacent interference orders) was $\approx$800 km s^{-1}. The [N II] 6584 Å line was in the middle of this range and was clearly separated from Hα, whose largest zero-level width did not exceed 200 km s^{-1} everywhere in the region under study.

The interferometer field of view and angular resolution for observations with the focal reducer at the Cassegrain focus of the 125-cm telescope are 10′ and 3″–4″, respectively.

A gas-filled tube was used as the laboratory Hα source to calibrate the radial velocities and to allow for the instrumental profile of the interferometer.

The data reduction technique was detailed by Pravdikova (1995). Each line profile was fitted with one or more Gaussians by assuming that the FWHM of each component was larger than the FWHM of the instrumental profile and that the signal-to-noise ratio was $\geq$5. The profile was fitted with a set of Gaussians in those cases where either several peaks, or a clear profile asymmetry, or broad line wings were observed.

In the course of our long-term program for studying the region, we obtained more than 1000 interferograms. As a result of their processing, we measured the velocities at maximum and the FWHMs of individual Hα components approximately at 20 000 positions in the Cygnus region. These data were used here.

Our observing technique allows us to investigate the extended complex in Cygnus, more than 20° in size, with an angular resolution of 3″–4″, but this requires too much observing time. Therefore, the region was covered with measurements with a nonuniform density. Detailed observations with a multiple overlapping were performed for separate large areas. The velocity field was investigated most extensively in the central and western sectors of the region; in the rest of the region, mostly brighter nebulae (ME $\geq$ 100 pc cm^{-6}) have been investigated so far as a tradeoff. In the areas of weak emission, we carried out mainly search observations with a large step. Only if anomalous velocities or multipeaked line profiles were found did we study the region in detail.

The velocities and line widths for the extended filaments that form the giant ring system mentioned above were measured selectively, with a poor spatial coverage.

2.2. Results of the Interferometric Observations

Figure 2 shows a map of optical emission and marks the regions with measured radial velocities.

The small heavy squares indicate the localization of the positions for which individual digital images were obtained with the Fabry–Perot etalon. The square size roughly corresponds to the size of an interference Hα ring in projection onto the sky. The numbers beside the squares give the radial velocities determined by processing the corresponding interferogram. Since the interference-ring radius is typically $\approx$3′–5′, for our purposes, we disregarded the coordinate differences between the radial scans of the interference ring that were used to construct the line profiles. Accordingly, for each position, we averaged from 10–12 to 20–25 velocity measurements for different radial scans of one or two interference rings. The rms error of each velocity measurement varies from interferogram to interferogram within the range 1.5 to 4.5 km s^{-1}. Only for the group of very weak filaments in the southeast of the region does the error exceed these values, ranging from 5 to 9 km s^{-1} for different interferograms. In this way, we present the results of our measurements for those positions at which mostly search observations were carried out.

The results of more detailed observations of the eleven fields for which many interferograms that overlap the field with a large density were obtained are presented in the form of radial-velocity histograms. The large rectangles in Fig. 2 mark the boundaries of fields nos. 1–11 for which radial-velocity histograms were constructed in Hα. The corresponding histograms are shown in Fig. 3.

The velocity histograms shown in Fig. 3 were fitted with a set of Gaussians; the fitting results are presented in the table. The columns give, respectively, field numbers and boundary coordinates; mean radial velocities, FWHM and amplitude for each Gaussian of the histogram.

The results of our ionized-gas velocity measurements for the region can be summarized as follows.

The observed Hα profiles in the Superbubble region in Cygnus consist either of one component, occasionally with a blue or red wing, or of two to three components. In general, the intensity of the weak features observed in the wings does not exceed 15–20% of the intensity of the main component.

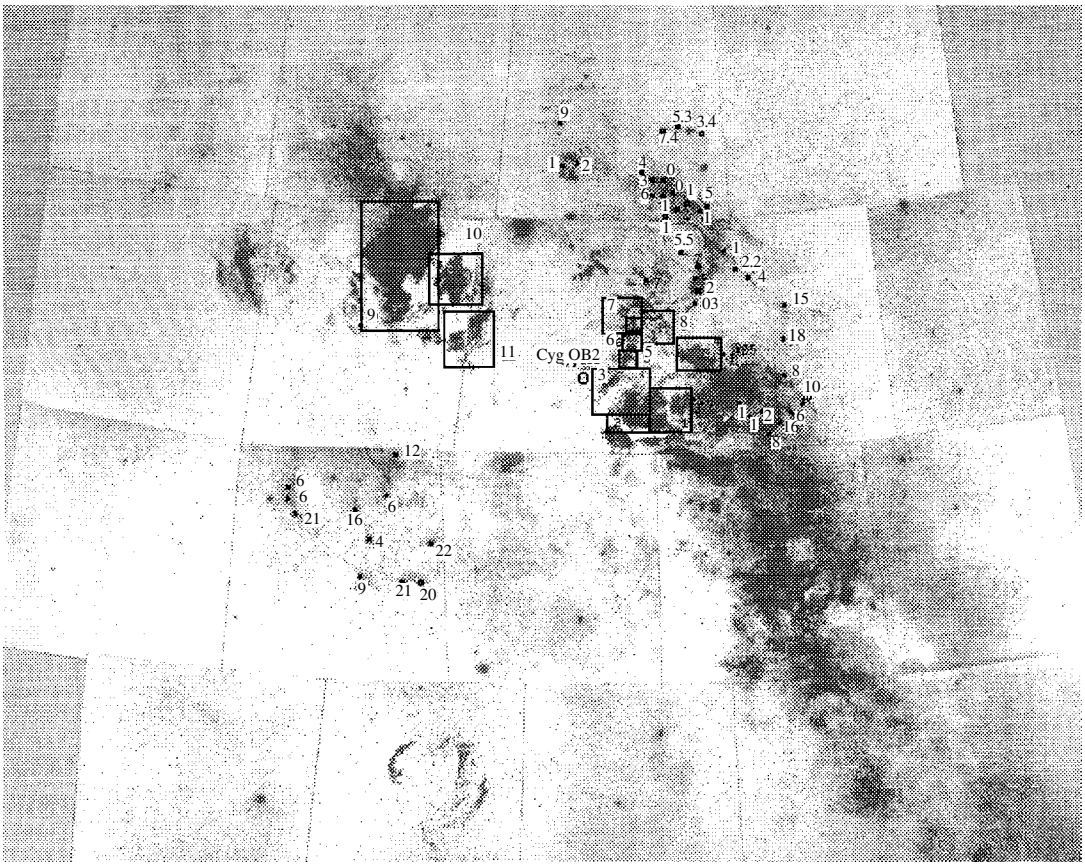

Fig. 2. A map of optical emission in the region. The squares indicate the localization of interference Hα rings for individual positions. The numbers beside the squares give the radial velocities averaged over 10 to 20 measurements. The rectangles indicate the boundaries of the fields for which the radial-velocity histograms were constructed from a large number of Hα measurements. The corresponding histograms are shown in Fig. 3.

Intense blueshifted and redshifted line components are observed toward several areas (fields nos. 3, 6, 7, 7a, 8). In these fields, the shifted line components are systematically more intense than the main component.

According to the results in Fig. 3 and in the table, the peak velocities of the intense line components vary within the range −40 to +45 km s^{-1}. Weaker features in the line wings at high positive and negative velocities are encountered in the range ≈−80 to ≈+55 km s^{-1}. Features are also observed at higher positive and negative velocities but at a level below our signal-to-noise ratio ≥ 5.

Let us to compare our velocity measurements with the Hα observations by Reynolds (1983) with a Fabry–Perot spectrometer in the $l = 0°$–$240°$ band along the Galactic plane at 2° intervals. These observations were carried out with a low angular resolution (50′) but with a higher sensitivity than in our measurements and a similar spectral resolution (12 km s^{-1}). Reynolds (1983) noted the presence of weak emission features (≈3 Rayleighs) at high positive velocities forbidden by the differential Galactic rotation and associated them with the expansion of the X-ray Superbubble at a velocity from 20 to 50 km s^{-1}. It seems that in Fig. 4 from the cited paper, two groups of forbidden positive velocities, $V(\mathrm{LSR}) = +35$ km s^{-1} and $V(\mathrm{LSR}) = +50 \ldots 52$ km s^{-1}, can be identified in the direction $l = 70° \ldots 88°$. The corresponding features at negative velocities are also seen in the range $l = 72° \ldots 82°$, and these are also represented by two groups, $V(\mathrm{LSR}) = -20 \ldots -22$ km s^{-1} and $V(\mathrm{LSR}) = -40 \ldots -42$ km s^{-1}.

3. ANALYSIS OF THE OPTICAL, X-RAY, AND INFRARED OBSERVATIONS FOR THE REGION: THE ACTION OF Cyg OB2 ON THE INTERSTELLAR MEDIUM

In this section, using our interferometric observations and X-ray, infrared, and radio studies of the region, we attempt to answer the following questions:

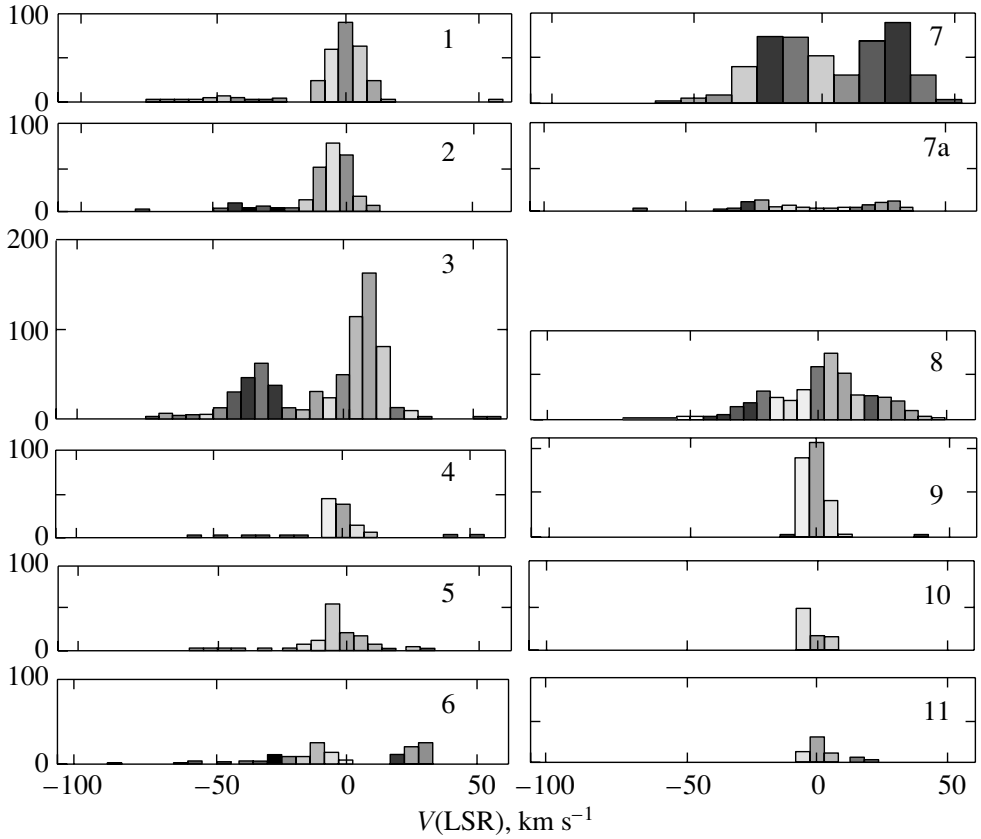

Fig. 3. The velocity histograms as constructed from Hα measurements for fields nos. 1–11 shown in Fig. 2.

Where is evidence for the action of the Cyg OB2 wind on the interstellar gas? Where is the shell swept up by the wind? Where are observational manifestations of the action of intense ionizing radiation from Cyg OB2 on the ambient gas? What are the parameters of the ambient interstellar medium that make the answers to these trivial questions so equivocal?

We immediately note that, first, the answers are not new but rest on a new line of reasoning, and, second, they require further observational confirmations.

The main difficulty involved in investigating the region is that the kinematic distances in this direction are poorly determined, because the line-of-sight projection of the Galactic rotation velocity changes little with distance. Therefore, the most complex question is whether the various gaseous and stellar components in this densely populated region along the Local spiral arm are physically related.

3.1. Kinematic Evidence of the Shell Swept up by the Wind

The problem of revealing kinematic evidence for the existence of a single shell swept up by a strong wind from Cyg OB2 is complicated by the fact that the observed Hα profile is the sum of emissions from the Local spiral arm up to distances of 3 kpc. Consequently, the velocities can differ because of the different localization of individual nubulae in distance and in the arm cross section. These differences attributable to the differential Galactic rotation and to the passage of spiral density waves lie within the range $-10 \ldots +10$ km s^{-1} for the sky region in question (Sitnik *et al.* 2001).

Even if we deal with a physical unity, then, since the hypothetical shell is located in an inhomogeneous dense medium, the line velocity variations over the image may result from the following:

(1) small-scale gas density fluctuations, which cause a warping of the ionization front and, accordingly, variations in the observed radial velocity;

(2) gas outflow via the champagne effect when the ionization front collides with dense cloud cores; in the presence of several clouds, gas outflow is observed in both directions.

Since the kinematic effect of these factors does not significantly exceed the speed of sound in an ionized gas either, evidence for the action of the Cyg OB2 wind should be sought by means of supersonic motions.

The weak features in the line wings observed at high positive and negative velocities are unreliable,

The radial-velocity distribution in fields nos. 1–11

Field	RA(2000)	D(2000)	V, km s^{-1}	FWHM	A
1	$20^h18^m15^s$–$20^h22^m15^s$	40°10′–41°10′	0.15 ± 0.03	13.8 ± 0.1	91.4
			−44.2 ± 0.6	16.4 ± 1.4	6.4
			−26.6 ± 0.5	7.8 ± 1.3	5.4
2	20 22 15 −20 28 15	40 07 −40 30	−4.2 ± 0.1	13.4 ± 0.3	81.8
			−38.2 ± 1.6	17.8 ± 3.8	6.7
3	20 25 15 −20 30 30	40 30 −41 35	9.3 ± 0.2	11.5 ± 0.3	161.7
			−31.7 ± 0.3	16.6 ± 0.8	58.2
			−5.9 ± 1.2	14.3 ± 2.9	28.2
4	20 15 30 −20 18 30	41 25 −42 10	−2.5 ± 0.2	8.7 ± 0.6	53.2
5	20 25 15 −20 27 45	41 35 −42 00	−4.3 ± 0.3	8.5 ± 0.7	51.8
6	20 24 45 −20 26 30	42 00 −42 25	−13.1 ± 1.1	23.3 ± 2.5	17.1
			27.4 ± 0.5	10.2 ± 1.2	25.8
?			−55.8 ± 3.7	11.0 ± 8.5	3.4
7	20 24 30 −20 29 50	42 30 −43 20	27.2 ± 1.0	20.2 ± 0.6	93
			−13.5 ± 0.7	31.7 ± 1.0	79
7a	20 24 30 −20 25 45	42 30 −42 50	26.7 ± 0.2	15.1 ± 0.5	11
			−9.2 ± 0.9	15.0 ± 2.0	5.5
			−22.4 ± 0.2	8.5 ± 0.6	14.2
7a*	20 24 30 −20 25 45	42 30 −42 50	26.4 ± 0.4	17.3 ± 1.0	16
			−19.7 ± 0.3	15.2 ± 0.5	21
8	20 20 15 −20 24 45	42 10 −43 00	−18.5 ± 0.7	23.2 ± 1.7	29
			4.3 ± 0.3	14.1 ± 0.7	71
			24.0 ± 0.8	18.9 ± 1.8	27
9	20 54 00–20 04 00	42 30 −46 00	−1.3 ± 0.1	9.4 ± 0.2	126
10	20 48 00–20 55 00	43 15 −44 35	−3.4 ± 1.1	5 ± 3	60.4
11	20 46 00–20 52 00	41 30 −43 00	−0.45 ± 0.02	7.7 ± 0.03	31.3
			16.3 ± 0.2	5.5 ± 0.4	3.5

because these are often identified at a noise level and may result from incomplete allowance for the radiation from faint stars. The high-velocity motions can also be associated with individual energy sources (the winds from WR and Of stars and blue supergiants or supernova explosions).

Thus, the intense shifted Hα components that we detected in several central fields may serve as the only reliable kinematic evidence for the existence of a shell. It seems reasonable to attribute these intense high-velocity components to the action of a strong Cyg OB2 wind. We emphasize that individual features at high negative velocities can undoubtedly be produced by the radiation from distant nebulae in the Perseus arm. At the same time, the detected positive velocities reaching +55 km s^{-1} have no obvious alternative explanation and most likely suggest that there are large-scale motions of ionized gas in the region.

If we deal with a physical unity, then the intense line features at high positive and negative velocities can characterize the receding and approaching sides of the expanding shell, respectively. Our interferometric observations (see Section 2) lead us to conclude that the possible expansion velocity of the hypothetical ionized shell reaches ≈ 25–50 km s^{-1}.

A single-peaked Hα line is emitted in the thin filaments that form the giant ring system. Its FWHM is 20–35 km s^{-1} for the group of filaments in the northwest and reaches 45 km s^{-1} in the southeast (the latter are considerably weaker). The results presented in Fig. 2 suggest that the velocity at the line peak in the northwest varies over the range -1 to $+6$ km s^{-1} (the rms error is 3–4 km s^{-1}). In the southeast, the velocity in the region of the weakest filaments varies over a wider range, from 4–6 to 20–22 km s^{-1}, with an rms error of 5–9 km s^{-1}. Reynolds (1983) measured the velocities of some filaments and found $V(\mathrm{LSR}) = \pm 3$ km s^{-1}, but these measurements were made with a clearly insufficient angular resolution of 50′ for such thin-filament structures.

Note that several authors (see, e.g., Chaffee and White 1982; Willson 1981; Piependbrink and Wendker 1988; Lockman 1989) observed the velocities of radio line features in the range $V(\mathrm{LSR}) = -15\ldots -20$ km s^{-1} to $V(\mathrm{LSR}) = +15\ldots +20$ km s^{-1} toward the Cygnus X complex by absorption and emission lines. This is generally considered as resulting from the different localization of the emitting and absorbing gas in distance rather than from peculiar motions. Gredel and Munch (1994) identified features in the interstellar C_2 absorption lines in the spectra of the Cyg OB2 stars nos. 5 and 12 at velocities reaching $V(\mathrm{LSR}) = 30$ km s^{-1}, which strongly suggests high-velocity motions of the molecular clumps in the association region. Interestingly, the two stars, which are 5 pc apart in the plane of the sky, exhibit absorption features at close velocities. In the opinion of the authors, this suggests a layered structure of the absorbing molecular clumps.

3.2. Cyg OB2: A New Estimate for the Mechanical Luminosity of the Stellar Wind

Previous studies of Cyg OB2 have revealed an elliptical stellar structure, $48' \times 28'$ in size, with ~3000 members. Three hundred OB stars, five O5 stars, the only northern-sky O3 star, three WR stars, and several O5 If, O4 IIIf, and LBV stars were identified in Cyg OB2; the association includes the most luminous and most massive stars of the Galaxy (Reddish *et al.* 1966; Torres-Dodgen *et al.* 1991; Massey and Thompson 1991; Persi *et al.* 1985). Reddish *et al.* (1966) first pointed out that Cyg OB2 differs from Galactic OB associations by compactness, large mass, and high star density, which make the object similar to young blue globular clusters in the LMC.

Recently, a qualitatively new step has been made by Knödlseder (2000). He passed from optical to infrared wavelengths, which allowed him to significantly increase the stellar population of the association by adding objects previously hidden due to strong absorption: according to his estimates, $A_V \simeq 5$–20^m for Cyg OB2 stars. According to the new data, Cyg OB2 is spherical in shape. The coordinates of its center are $\mathrm{RA}(2000) = 20^{\mathrm{h}}33^{\mathrm{m}}10^s$ and $\mathrm{D}(2000) = 41°12'$; $l = 80°7.2'$, $b = 0°43.8'$; the size of the region containing 90% of the stellar population is 90′ (45 pc). In what follows, the distance to Cyg OB2 is assumed to be $d = 1.7$ kpc, as estimated by Massey and Thompson (1991).

The current mass of Cyg OB2 is $(4–10)\times 10^4 M_\odot$, the number of its members with spectral types earlier than F3 reaches 8600 ± 1300, and the number of its OB stars is 2600 ± 400, including 120 O stars. This mass and star density distinguish Cyg OB2 from other associations so clearly that Knödlseder (2000) reached the following unequivocal conclusion: the object is actually the only Galactic representative of the population of young blue globular clusters, which are so numerous in the LMC. The H–R diagram for Cyg OB2 clearly reveals main-sequence stars up to a mass of 85 $M_\odot$; although the association is compact, star formation in it was, probably, not coeval (Massey and Thompson 1991). The age of Cyg OB2 is 3×10^6 yr, as estimated by Torres-Dodgen *et al.* (1991); using new data on the stellar population, Knödlseder *et al.* (2001) obtained $(2.5 \pm 0.1) \times 10^6$ yr.

The wind mechanical luminosity for previously known members of the association was estimated to be $L_w \simeq 10^{38}$ erg s^{-1} (Abbott *et al.* 1981). The mass loss rate for the five most luminous stars in Cyg OB2 is $\sim(2–10) \times 10^{-5}$ $M_\odot$ yr^{-1} at a wind velocity of 2000–7500 km s^{-1} (Persi *et al.* 1983; Leitherer *et al.* 1982).

Given the new data on the Cyg OB2 population, the above wind mechanical luminosities should be reestimated. We use a detailed analysis of the changes in wind energy during the evolution of a rich star grouping performed by Leitherer *et al.* (1992) (see also Comeron and Torra 1994). As follows from the cited paper, at an early stage ($t \le 2 \times 10^6$ yr) for normal metallicity, the wind mechanical luminosity is kept approximately constant, being 2×10^{34} erg s^{-1} per unit total mass of all the stars with masses in the range 1–120 $M_\odot$. The total mass for Cyg OB2 is $(4–10) \times 10^4$ $M_\odot$, which yields $L_w \simeq (1–2) \times 10^{39}$ erg s^{-1}. This mechanical luminosity is maintained at least for 2×10^6 yr and increases further as WR stars appear.

3.3. Possible Manifestations of the Shell Swept up by the Cyg OB2 Wind

The radius and expansion velocity of the shell that the Cyg OB2 wind could produce in a medium with a known initial density over a cluster lifetime $t \simeq (2–3) \times 10^6$ yr give the relations following from the classical theory by Castor *et al.* (1975) and Weaver *et al.* (1977):

$$R(t) = 66 n_0^{-1/5} L_{38}^{1/5} t_6^{3/5} \text{ pc},$$

$$v(t) = 39 n_0^{-1/5} L_{38}^{1/5} t_6^{-2/5} \text{ km s}^{-1},$$

where t_6 is the age, Myr; R is the radius, pc; and L_{38} is the stellar-wind mechanical luminosity, 10^{38} erg s^{-1}.

It follows from these relations that the possible expansion velocity of $\approx$50 km s^{-1} determined from the optical emission can be produced by the Cyg OB2 wind in a medium with a reasonable initial density $n_0 \simeq 1$ cm^{-3}; in this case, the shell radius can reach $\simeq$200 pc.

The structures of such a size are represented by the giant system of optical filaments and by the X-ray Superbubble, which have been repeatedly discussed in the literature. Below, we briefly consider the main arguments for and against this identification.

The giant ring of optical filaments. The giant ring of weak optical filaments mentioned by Morgan *et al.* (1955) and Struve (1957) has ME $\leq$ 100 cm^{-6}pc (Dickel *et al.* 1969). Ikhsanov (1960) considered this system of filaments as a physical unity that bounds the complex of nebulae ionized by Cyg OB2 stars.

Based on the extinction A_V estimated from the ratio of the Hα and radio continuum intensities and on the distance dependence of A_V, Kapp-Herr and Wendker (1972) concluded that the filaments constituting the giant shell in the plane of the sky lay at different distances. Unfortunately, this method is unreliable in the Cygnus region, because the absorbing matter is inhomogeneous: we now know that A_V varies between 5^m and 20^m (Knödlseder 2000) even toward the compact Cyg OB2 grouping located at the same photometric distance of 1700 pc. Besides, in these estimates, the optical emission was averaged over 11′ fields and the radio emission was estimated with a 30′ resolution, which is clearly not enough for such thin filaments.

Our ionized-gas velocity measurements are consistent with the assumption that the giant system of filaments is the shell swept up by the Cyg OB2 wind. We determined the possible expansion velocity, $\approx$50 km s^{-1}, from the Hα emission of the central region, mainly toward the Cygnus X complex. The filaments with measured velocities are mostly located on the Superbubble periphery and their radial velocities must be lower because of the projection effect.

The filaments in the southeast must be studied in more detail, because our test observations with a poor spatial coverage revealed high positive velocities, 20–22 km s^{-1}. These are the weakest filaments among the objects that we investigated toward Cygnus; the measurement error in the velocity here is larger than that in the remaining region (5–9 km s^{-1}; see Section 1). Besides, it may well be that these filaments do not lie on the shell periphery. As Fig. 1 shows, the system of optical filaments and the X-ray Superbubble as a whole closely coincide in the plane of the sky, but the X-ray region in the southeast goes outside the thin optical filaments by 2°–3°. The high velocities of these filaments may be attributable to a local energy source.

Note that the ring structure of H I clouds with the same angular size observed in the velocity range -20 to $+20$ km s^{-1} (Gosachinskii and Lozinskaya 1997), probably, corresponds, to the system of optical filaments. This is also an argument for a physical unity.

The X-ray Superbubble in Cygnus. The X-ray Superbubble in Cygnus that was identified by Cash *et al.* (1980) using HEAO-1 observations with an angular resolution of 1°.5 × 3° was considered by the authors as a physical unity associated with Cyg OB2 and with the above system of optical filaments. The size of the Superbubble was estimated to be 450 pc, its X-ray luminosity is $L_X \simeq 5 \times 10^{36}$ erg s^{-1}, and the density of the emitting plasma is $n_e \approx 0.02$ cm^{-3}. Different authors explained the formation of a superbubble with such parameters either by sequential explosions of several tens of supernovae in Cyg OB2 (Cash *et al.* 1980), or by the combined action of the wind from the same association (Abbott *et al.* 1981), or by a supernova explosion inside the previously formed low-density cavity (Higdon 1981), or by the explosion of a single supermassive star (Blinnikov *et al.* 1982).

According to the alternative interpretation by Bochkarev and Sitnik (1985) and Uyaniker *et al.* (2001), the X-ray Superbubble is not a physical unity but is the sum of emissions from supernova remnants, the shells around individual stars and OB associations swept up by the wind, cataclysmic variables, hot stellar coronas, etc. located in the Local spiral arm at distances from 0.5 to 4 kpc. The X-ray shell morphology in the plane of the sky results from absorption of the X-ray emission in a dense layer of clouds at 700–900 pc (the so-called Great Cygnus Rift).

We performed a detailed analysis of the ROSAT observations in an effort to reveal the possible X-ray

emission component produced by a strong Cyg OB2 wind. Here, we briefly summarize the main conclusions of our analysis.

The fact that the shell morphology of the Superbubble is mainly explained by absorption may be considered to have been firmly established.

The ROSAT observations confirm the previous conclusion by Bochkarev and Sitnik (1985) that most of the X-ray emission (up to 50–80%) is produced by point sources of a different nature. However, their conclusion that the diffuse part of the X-ray emission originates from the cavities swept up by individual OB associations in the Cygnus region is apparently not confirmed. A simple superposition of the association boundaries on the ROSAT X-ray map reveals no one-to-one coincidence and this cannot be explained by absorption [see Fig. 1 in Uyaniker *et al.* (2001)].

The conclusion by Uyaniker *et al.* (2001) that individual regions of the Cygnus Superbubble have different radiation spectra and cannot be considered as a physical unity is based on a comparison of the X-ray hardness and the column density of the absorbing matter N(H I). The authors pointed out that the bulk of the absorbing matter in the fields with the strongest absorption have high negative velocities, $V(\mathrm{LSR}) \leq -30 \ldots -40$ km s^{-1}. This result is of great interest but it requires a further detailed analysis. Indeed, the above effect implies that either the bulk of the matter lies far and cannot absorb the X-ray emission or it is located in the region under consideration and has been affected by a shock wave, which accounts for the observed high negative velocity. (If this is the case, then the velocity of the absorbing neutral hydrogen closely matches our derived expansion velocity of the hypothetical shell.)

In any case, however, the X-ray spectra of different parts of the Superbubble should be compared only after removing the point sources whose contribution is comparable to the diffuse component.

The diffuse X-ray emission from the Superbubble. To identify the diffuse X-ray emission component, we used the ROSAT XRT/PSPC all-sky survey maps cleaned from point sources; the angular resolution is 12′ (Snowden *et al.* 1997).

The derived intensity distribution of the diffuse 0.7–0.9 keV emission is shown in Fig. 4. The total size of the X-ray region determined from the outermost areas of the Superbubble reaches 15°–18°.

An extended arc-shaped X-ray region, which forms the eastern and southeastern parts of the Superbubble (RA = $21^{\mathrm{h}}0^{\mathrm{m}}$–$21^{\mathrm{h}}33^{\mathrm{m}}$; D = 31°–46°), is clearly seen in the figure. This eastern X-ray arc currently seems to be the most plausible observational manifestation of the part of the shell swept up by the Cyg OB2 wind in a tenuous interstellar medium.

According to Uyaniker *et al.* (2001), this arc structure (the southern arc in the Galactic coordinate system used in their paper) was produced by the Cyg OB4 wind. This conclusion does not seem justifiable. Indeed, Cyg OB4 is the poorest association in the region; it consists of a mere two OB stars (B9 Iab and B0.5 IV; see Blaha and Humphreys 1989). Besides, the elongated shape of the X-ray arc reveals no clear morphological relationship to this association.

Figure 5a shows the intensity distribution of the diffuse X-ray emission, as constructed from ROSAT data, superimposed on the distribution of the intensity ratio of infrared emissions in two bands (60/100 μm), as constructed from IRAS data. Only the brightest X-ray isophotes (confidence level 100σ) corresponding to 16, 32, 100, 200, and 13 000 in units of 10^{-6} counts s^{-1} per square arcmin or to 4, 8, 26, 51, 3300 in units of 10^{-12} erg s^{-1} per square arcmin are shown.

The dust temperature distribution in the intensity ratio of infrared 60/100 μm emissions (see Fig. 5) reveals an extended (≈15°) elliptical structure of warmer dust that generally copies the shape of the X-ray Superbubble and surrounds it. An extended arc is also clearly seen here east of the region. This arc of warm dust has the same shape as the X-ray arc, and it also surrounds the latter from outside. Such a region of warm dust can be produced by inelastic collisions of dust grains with hot X-ray plasma, as is the case in supernova remnants.

Figure 5b shows the temperature distribution of the X-ray emitting plasma that we derived from ROSAT data. The temperature map was constructed from calibrations of the temperature and absorption effects on the fluxes in three spectral bands of the PSPC/ROSAT detector (Finoguenov 1997) and superimposed on the intensity distribution of the diffuse X-ray emission. The temperature map was obtained from the so-called spectral hardness, which is defined as the ratio $(F2-F1)/(F1+F2)$, where $F1$ is the 0.5–0.9 keV flux and $F2$ is the 0.9–2 keV flux, and smoothed with a Gaussian with the FWHM $\sigma =$ 4 pixels. The white spot inside the Superbubble may result from the absorption corresponding to a column density of absorbing atoms $N(\mathrm{HI}) \geq 4 \times 10^{21}$ cm^{-2}.

A detailed analysis of the distributions of temperature, intensity of the diffuse X-ray emission, and absorbing atoms on the line of sight is beyond the scope of this study. Here, it it only important to note that the X-ray temperature differences over the entire length of the eastern arc are small, mainly from 0.50 to 0.57 keV (except for the compact source). This allows

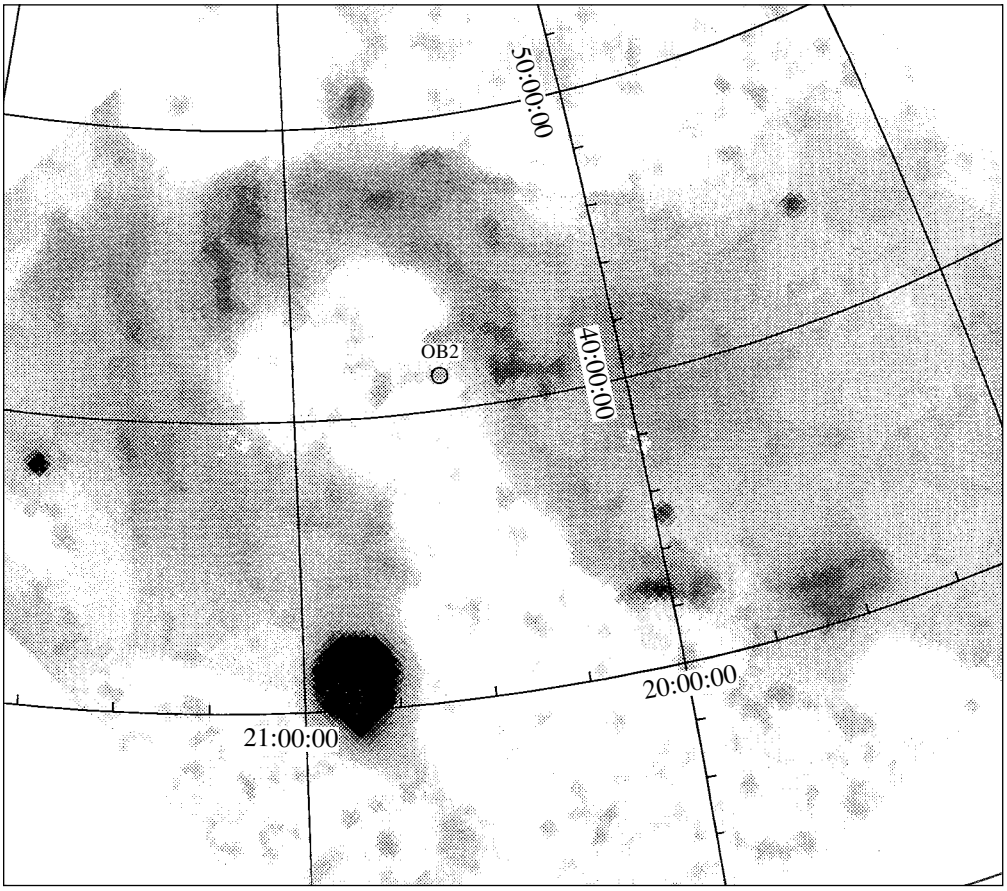

Fig. 4. The intensity distribution of the diffuse X-ray emission, as constructed from ROSAT 0.7–0.9-keV data. The point sources were removed; the bright spot in the south is the supernova remnant Cygnus Loop.

the eastern arc to be considered as a physical entity, which most likely represents the X-ray emission from the part of the shell swept up by the Cyg OB2 wind.

The X-ray emission from the plasma heated by the Cyg OB2 wind, probably, contributes significantly to other parts of the Cygnus Superbubble as well. However, it cannot yet be reliably identified against the background of the total emission along the Local spiral arm. Therefore, we estimate the parameters of the entire X-ray emission as an upper limit on the luminosity and mass of the hot plasma attributable to the Cyg OB2 wind.

The identified diffuse X-ray 0.4–2.1-keV emission from the entire Superbubble corresponds to 275.1 counts s^{-1}. For an equilibrium plasma of solar chemical composition at the temperature $kT_e = 0.6$ keV and a distance of 1.7 kpc, this gives a bolometric luminosity $L_X \simeq 1.2 \times 10^{36}$ erg s^{-1}. In this case, most of the luminosity is emitted in the 0.4–2.1 keV band ($L_{0.4-2.1} \simeq 0.88 \times 10^{36}$ erg s^{-1}).

The mass of the X-ray emitting plasma reaches $M \simeq 8.1 \times 10^4\ M_\odot$, and the electron density is $n_e \simeq 4.6 \times 10^{-3}$ cm^{-3}.

We emphasize once again that this is an upper limit on the luminosity and mass of the hot plasma, which may be attributable to the Cyg OB2 wind. However, even if most of the emission from the X-ray Superbubble is attributable to the Cyg OB2 wind, our new estimate of the wind mechanical luminosity suggests that there are currently no problems with the Superbubble energetics.

3.4. The Interstellar Medium Around Cyg OB2: A General Scheme

The last question posed at the beginning of this section seems easiest to answer: the shell swept up by the wind can be hidden in a highly inhomogeneous interstellar medium characterized by dense clouds with even denser compact clumps and a tenuous intercloud medium.

The conclusion of a high local gas density in the Cyg OB2 region follows from an analysis of the interstellar extinction toward this region.

According to Neckel and Klare (1980), the extinction toward Cyg OB2 reaches $A_V = 7^m$ at a distance

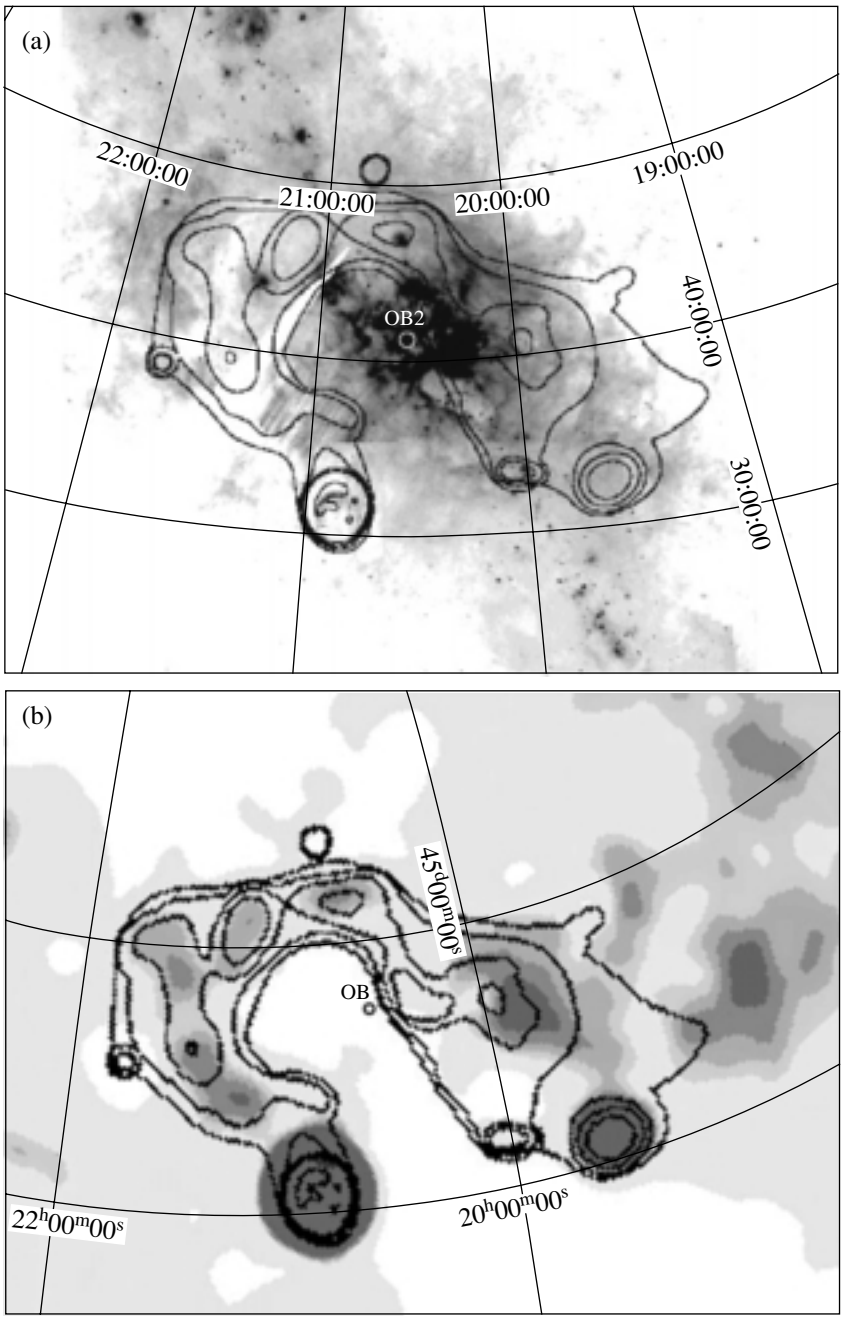

Fig. 5. (a) The intensity distribution of the diffuse X-ray 0.7–0.9 keV emission (indicated by isophotes) superimposed on the distribution of the intensity ratio of infrared emissions in two bands (60/100 μm), as constructed from IRAS data (indicated by shades of gray). The brightest X-ray isophotes (confidence level 100σ) corresponding to 4, 8, 26, 51, and 3300 in units of 10^{-12} erg s^{-1} arcmin^{-2} are presented. The position of Cyg OB2 is marked. (b) The X-ray plasma temperature distribution (indicated by shades of gray) superimposed on the same X-ray intensity distribution. The temperature levels, from darkest (colder plasma) to lightest (hotter plasma), correspond to 0.24, 0.34, 0.45, 0.50, 0.54, 0.57, 0.63, and 0.85 keV.

of ≈1 kpc; in nearby fields, $A_V = 7^{m}$ is reached at a distance of 1–2 kpc. At larger distances, the extinction increases only slightly up to a limiting distance of 3 kpc. According to Ikhsanov (1959), in the extended region bordering Cyg OB2 in the west, north, and south, the extinction monotonically increases to $A_V \simeq 2\overset{m}{.}6$ up to a distance of 1.15–1.4 kpc and then sharply increases to $A_V \simeq 6.5$–7^{m} at a distance of 2.2–3.5 kpc. The brightness ratio of optical nebulae in the radio continuum and Hα toward Cyg OB2 gives an extinction $A_V = 4$–6^{m} (Dickel and Wendker 1978). Thus, the extinction in the entire extended

region up to a distance of 3 kpc does not significantly exceed $A_V \simeq 7^m$.

At the same time, the extinction derived from photometry of Cyg OB2 stars is $A_V = 5–20^m$ (Knödlseder 2000). Hence, a significant fraction of the absorbing matter (up to 50% of the column density) is local relative to Cyg OB2.

The conclusion of a high local gas density in the Cyg OB2 region can also be drawn from other considerations. The star density at the center of the young globular cluster Cyg OB2 is 40–150 $M_\odot$ pc^{-3}, as estimated by Knödlseder (2000). Since only part of the mass of the parent molecular cloud turns into stars, we obtain a lower limit on the initial atomic hydrogen density in the parent cloud: $n(H_2) \geq (1–3) \times 10^3$ cm^{-3}.

The dense matter of the parent molecular cloud left after the main star-formation episode is rapidly removed from the central region of the globular cluster by ionizing radiation and winds from the formed stars. However, the densest gaseous clumps are not swept up by the shock wave but are compressed and remain immersed in a tenuous cavity. Such dense molecular clumps live long enough and can presently be observed in the Cyg OB2 region. They are actually observed: the clumpy structure of the molecular gas composed of separate clumps was revealed by interstellar C_2 absorption lines in the spectra of the Cyg OB2 stars nos. 5 and 12 (Gredel and Munch 1994). The characteristic size of the clumps is ≤ 5 pc (the most probable size is 1 pc) and their mass is $\approx 200\ M_\odot$; the clumps are located in the Cyg OB2 region. Using the size and column density $N(C_2)$, we obtain the molecular hydrogen density in the clumps, $n(H_2) \sim 100–10^3$ cm^{-3}. (The lower limit at $l = 5$ pc is $n(H_2) = 300–600$ cm^{-3} for star no. 12 and $n(H_2) = 130–300$ cm^{-3} for star no. 5.) Such dense clumps are immersed in a low-density gas.

Cygnus X as an H II region ionized by Cyg OB2. The Lyman continuum flux from 120 O-stars of Cyg OB2 alone is $\simeq 10^{51}$ phot. s^{-1} (Knödlseder 2000). In a homogeneous medium with a density of 1, 10, and 100 cm^{-3}, the radius of the corresponding H II region reaches 300, 65, and 15 pc and the emission measure is 300, 6500, and 150 000 cm^{-6}pc, respectively.

Whereas the absence of intense optical emission from this ionized gas can be explained by strong absorption, its intense thermal radio emission must be observed in any case. Using the exclusion method, we find only one possibility: this emission is represented by the Cygnus X complex of radio sources. [This possibility has been repeatedly discussed starting from Veron (1965); see also Landecker 1984.] In any case, the regions of ionized gas with appropriate density and emission measure are observed only in Cygnus X. The bright features of the complex are observed against the background of an extended weaker radio continuum source, 6°–7° in size, with Cyg OB2 being projected onto its central part (Wendker 1970; Huchmeier and Wendker 1977). This diffuse source was immediately identified by the authors as an H II region ionized by Cyg OB2 (see also Wendker *et al.* 1991). If the extended source is at the distance of Cyg OB2, then its radius reaches 100 pc, ME $\simeq 2000$ cm^{-6} pc, and the mean electron density is ≈ 3 cm^{-3}. ME $\simeq 1000–50000$ cm^{-6}pc in the bright H II regions of Cygnus X and reaches $10^6–10^7$ cm^{-6}pc in compact radio clumps; the density is $n_e = 10–100$ см$^{-3}$ in the bright radio sources and at least an order of magnitude higher in compact clumps (see, e.g., Dickel *et al.* 1969; Piependbrink and Wendker 1988).

Thus, the parameters of the Cygnus X complex agree with those expected for the H II region ionized by Cyg OB2 stars. The only objection to this identification is the long-standing and popular belief that Cygnus X is not a physical unity but is the sum of emissions from the many sources located at different distances, from 500 pc to 3–4 kpc, along the spiral arm (see, e.g., Wendker 1984; Piependbrink and Wendker 1988; and references therein).

The following two basic methods of distance determination underlie this belief: from the radial velocities of sources and from the extinction A_V. Both are unreliable in the direction of Cygnus (see above).

Therefore, we cannot rule out the possibility that the diffuse component and some of the sources forming the Cygnus X complex are located at the same distance of 1700 pc. Of course, individual features of the complex can lie nearer or farther. In this case, the Cygnus X complex could be a remnant of the parent cloud ionized by Cyg OB2 stars. [This conclusion was also drawn by Landecker (1984) from detailed measurements of the complex in the H166α recombination line.] Separate dense clumps of this cloud became nests for ongoing star formation and have their own, local ionization sources.

A number of findings argue for the validity of this assumption.

The dust temperature distribution in the region. Figure 5 shows the distribution of the intensity ratio of infrared emissions in two bands (60/100 μm), as constructed from IRAS data, which reflects the dust temperature distribution in the entire region under study. The highest temperature in a large region containing the Cygnus Superbubble is observed toward the Cygnus X complex. The Cyg OB2 cluster lies at the center of the region of warm dust, and

the warmest local spots are directly projected onto Cyg OB2 and surround it. This is evidence of the physical interaction between Cyg OB2 stars and a dense cloud.

The CO distribution in the region. The Cyg OB2 cluster lies within a local region of reduced brightness surrounded by the brightest CO clouds in the direction of Cygnus X. This is clearly shown by the CO isophotal maps integrated over the velocity range -25 to $+25$ km s^{-1} and over narrower velocity ranges: -5–0; 0–5, 5–10, and 10–15 km s^{-1} [see Leung and Thaddeus (1992) and references therein]. This is consistent with the proposed model, because the parent molecular cloud must be destroyed in close proximity to Cyg OB2.

The H I distribution in the Cygnus X region. Note also the shell structure of H I and CO clouds identified by Gosachinskii *et al.* (1999) around the Cygnus X complex. Although this extended shell was identified with major reservations, its existence, if confirmed, argues for a single complex. These authors (see also Gosachinskii and Lozinskaya 1997) also pointed out that the positions and radial velocities of H II regions, as inferred from the observations by Piependbrink and Wendker(1988) in radio recombination lines, reveal a semblance of a ring structure, suggesting a large-scale radial motion in Cygnus X in the velocity range -12 to $+10$ km s^{-1}.

A general scheme for the interaction of Cyg OB2 with the interstellar medium Currently available optical, X-ray, infrared, and radio observations allow the following general scheme of the region to be considered.

The blue globular cluster Cyg OB2 was formed in a medium with a high initial density and mainly destroyed the parent molecular cloud over its lifetime. The radio emission from the remnants of the parent cloud ionized by Cyg OB2 is represented by the diffuse component and, possibly, by individual sources of the Cygnus X complex. The densest compact clumps of the destroyed molecular cloud are observed in radio lines in absorption.

The high gas velocities that we detected in optical nebulae are attributable to an expansion of the shell swept up by the Cyg OB2 wind. The expansion velocity of the swept-up shell reaches 25–50 km s^{-1}; this shell is bounded by a giant system of thin filaments.

The burst of the Cyg OB2 wind into a low-density intercloud medium is responsible for the formation of an extended region of diffuse X-ray emission. The cluster was apparently formed not at the center but at the edge of a dense cloud. Therefore, the burst of the wind into a low-density medium in the southeastern direction produced the most prominent arc-shaped structure of X-ray and infrared emission. This arc-shaped structure seems to be the most plausible manifestation of the shell swept up by a strong Cyg OB2 wind. That is why Cyg OB2 and the dense ionized cloud (Cygnus X) are located not at the center but on the northwestern boundary of the extended X-ray region (the Cygnus Superbubble).

CONCLUSIONS

Our most conservative conclusions can be formulated as follows:

(1) Our interferometric Hα observations have revealed high-velocity motions of ionized gas, which may be related to an expansion of the hypothetical shell swept up by the Cyg OB2 wind in a medium with an initial density of 1–10 cm^{-3}. The expansion velocity determined by these motions reaches 25–50 km s^{-1}.

(2) Given the number of OB stars increased by an order of magnitude, Cyg OB2 has the strongest stellar wind among Galactic associations: according to our new estimate, $L_w \simeq (1-2)\times 10^{39}$ erg s^{-1}. The wind mechanical luminosity over a Cyg OB2 lifetime of $\approx(2$–$3)\times 10^6$ yr is high enough to produce a shell comparable in size to the X-ray Superbubble and to the giant system of optical filaments.

(3) The most plausible manifestations of the shell swept up by the Cyg OB2 wind in a tenuous medium are the following: the giant system of optical filaments; the diffuse component of the X-ray Superbubble in Cygnus, primarily the extended eastern arc that forms it; the extended elliptical region of heated dust, in particular, the eastern arc of heated dust that bounds the arc-shaped X-ray region.

(4) The Cyg OB2 cluster formed in a medium with a high initial density. The remnants of the parent molecular cloud ionized by Cyg OB2 stars are, probably, represented by the diffuse component and, possibly, by individual sources of the Cygnus X complex.

The proposed scheme undoubtedly requires a thorough observational verification. Of greatest interest are searches for high-velocity features of interstellar absorption lines in the entire region; a detailed analysis of the spectrum for the diffuse X-ray emission component of the Superbubble; and a comparison of the column density of the absorbing gas derived from the X-ray spectrum with direct CO line measurements. Such a study is already under way.

ACKNOWLEDGMENTS

This work was supported by the Russian Foundation for Basic Research (project no. 01-02-16118) and the Program "Astronomy" (project no. 1.3.1.2).

REFERENCES

1. D. C. Abbott, J. H. Bieging, and E. Churchwell, Astrophys. J. **250**, 645 (1981).
2. C. Blaha and R. Humphreys, Astron. J. **98**, 1598 (1989).
3. S. I. Blinnikov, V. S. Imshennik, and V. P. Utrobin, Pis'ma Astron. Zh. **8**, 671 (1982) [Sov. Astron. Lett. **8**, 361 (1982)].
4. N. G. Bochkarev and T. G. Sitnik, Astrophys. Space Sci. **108**, 237 (1985).
5. P. Brand and W. J. Zealey, Astron. Astrophys. **38**, 363 (1975).
6. W. Cash, P. Charles, S. Bowyer, *et al.*, Astrophys. J. Lett. **238**, L71 (1980).
7. J. Castor, R. McCray, and R. Weaver, Astrophys. J. Lett. **200**, L107 (1975).
8. F. H. Chaffee and R. E. White, Astrophys. J., Suppl. Ser. **50**, 169 (1982).
9. F. Comeron and J. Torra, Astrophys. J. **423**, 652 (1994).
10. H. R. Dickel and H. J. Wendker, Astron. Astrophys. **66**, 289 (1978).
11. H. H. R. Dickel, H. Wendker, and J. H. Bieritz, Astron. Astrophys. **1**, 270 (1969).
12. A. V. Finoguenov, Candidate's Dissertation (Inst. Kosm. Issled. Ross. Akad. Nauk, Moscow, 1997).
13. I. V. Gosachinskii and T. A. Lozinskaya, Astron. Zh. **74**, 201 (1997) [Astron. Lett. **41**, 174 (1997)].
14. I. V. Gosachinskii, T. A. Lozinskaya, and V. V. Pravdikova, Astron. Zh. **76**, 453 (1999) [Astron. Rep. **43**, 391 (1999)].
15. R. Gredel and G. Munch, Astron. Astrophys. **285**, 640 (1994).
16. J. C. Higdon, Astrophys. J. **244**, 88 (1981).
17. W. K. Huchmeier and H. J. Wendker, Astron. Astrophys. **58**, 197 (1977).
18. R. N. Ikhsanov, Izv. Krym. Astrofiz. Obs. **21**, 257 (1959).
19. R. R. Ikhsanov, Astron. Zh. **37**, 988 (1960) [Sov. Astron. **4**, 923 (1960)].
20. A. V. Kapp-Herr and H. J. Wendker, Astron. Astrophys. **20**, 313 (1972).
21. J. Knödlseder, Astron. Astrophys. **360**, 539 (2000).
22. J. Knödlseder, M. Cervino, D. Schaerer, *et al.*, astro-ph/0104074 (2001).
23. T. L. Landecker, Astron. J. **89**, 95 (1984).
24. C. Leitherer, H. Hefele, O. Stahl, and B. Wolf, Astron. Astrophys. **108**, 102 (1982).
25. C. Leitherer, C. Roberts, and L. Drissen, Astrophys. J. **401**, 594 (1992).
26. E. O. Leung and P. Thaddeus, Astrophys. J., Suppl. Ser. **81**, 267 (1992).
27. F. Lockman, Astrophys. J., Suppl. Ser. **70**, 469 (1989).
28. P. Massey and A. B. Thompson, Astron. J. **101**, 1408 (1991).
29. W. W. Morgan, B. Stromgren, and H. M. Johnson, Astrophys. J. **121**, 611 (1955).
30. Th. Neckel and G. Klare, Astron. Astrophys., Suppl. Ser. **42**, 251 (1980).
31. P. Persi, M. Ferrari-Toniolo, and G. L. Grasdalen, Astrophys. J. **269**, 625 (1983).
32. P. Persi, M. Ferrari-Toniolo, M. Tapia, *et al.*, Astron. Astrophys. **142**, 263 (1985).
33. A. Piependbrink and H. J. Wendker, Astron. Astrophys. **191**, 313 (1988).
34. V. V. Pravdikova, Pis'ma Astron. Zh. **21**, 453 (1995) [Astron. Lett. **21**, 403 (1995)].
35. V. L. Reddish, L. Lawrens, and N. M. Pratt, Publ. R. Obs. Edinb. **5**, 111 (1966).
36. R. J. Reynolds, Astrophys. J. **268**, 698 (1983).
37. E. G. Sitnik, A. M. Mel'nik, and V. V. Pravdikova, Astron. Zh. **78**, 40 (2001) [Astron. Rep. **45**, 34 (2001)].
38. S. L. Snowden, E. Egger, M. J. Freyberg, *et al.*, Astrophys. J. **485**, 125 (1997).
39. O. Struve, Sky Telesc. **16**, 118 (1957).
40. A. V. Torres-Dodgen, M. Tapia, and M. Carroll, Mon. Not. R. Astron. Soc. **249**, 1 (1991).
41. B. Uyaniker, E. Furst, W. Reich, *et al.*, Astron. Astrophys. **371**, 675 (2001).
42. P. Veron, Ann. Astrophys. **28**, 391 (1965).
43. R. Weaver, R. McCray, J. Castor, *et al.*, Astrophys. J. **218**, 377 (1977).
44. H. J. Wendker, Astron. Astrophys. **4**, 378 (1970).
45. H. J. Wendker, Astron. Astrophys., Suppl. Ser. **58**, 291 (1984).
46. H. J. Wendker, L. A. Higgs, and T. L. Landecker, Astron. Astrophys. **241**, 551 (1991).
47. R. F. Willson, Astrophys. J. **247**, 116 (1981).

Translated by V. Astakhov

Astronomy Letters, Vol. 28, No. 4, 2002, pp. 237–240. Translated from Pis'ma v Astronomicheskiĭ Zhurnal, Vol. 28, No. 4, 2002, pp. 276–280.

Localization of X-ray Sources in Six Galactic Globular Clusters from Chandra Data

M. G. Revnivtsev[1, 2*], S. P. Trudolyubov[3, 1], and K. N. Borozdin[3, 1]

[1] *Space Research Institute, Russian Academy of Sciences, Profsoyuznaya ul. 84/32, Moscow, 117810 Russia*

[2] *Max-Planck Institut für Astrophysik, Karl-Schwarzschild-Str. 1, Garching bei München, 85740 Germany*

[3] *NIS-2, Los Alamos National Laboratory, Los Alamos, 87545 New Mexico, USA*

Received August 31, 2000; in final form, November 20, 2001

Abstract—We present our observations of six Galactic globular clusters where the following bright X-ray sources were observed: NGC 6440, NGC 6441, NGC 6624, Terzan 1, Terzan 2, and Terzan 6. Using the Chandra observatory, we were able to achieve a localization accuracy of $0''.6$ for X-ray sources in the globular clusters. The error circle considerably decreased compared to the observations of other observatories, by more than a factor of 10 for some clusters. We detected at least one X-ray source in each of the globular clusters studied and 12 sources in the globular cluster NGC 6440. The source XB1733-30 in Terzan 1 was not detected by the Chandra observatory; we obtained an upper limit on its luminosity.

Key words: *X-ray and gamma-ray sources*

INTRODUCTION

Galactic globular clusters have always been among the objects of particular interest for X-ray astronomy (Hut *et al.* 1992). Estimates show that the globular clusters contain much more X-ray binaries per unit mass than the rest of the Galaxy (Clark 1975).

Initially, it was hypothesized that the X-ray sources in globular clusters could be massive black holes (Bahcall and Ostriker 1975) or black holes of stellar mass (Grindlay 1978). However, the bright X-ray objects in globular clusters were subsequently found to be the sources of type-I X-ray bursts. Thus, presently, these X-ray sources are generally recognized to be binaries with neutron stars. However, new observations show that many globular clusters also contain a considerable number of weaker X-ray sources (Grindlay *et al.* 2001). In this case, it is not clear whether all these sources are X-ray bursters or a heterogeneous set of objects.

Six of the twelve known bright X-ray sources in globular clusters were localized most accurately (with an accuracy of $\sim 2''-3''$) using the HRI instrument onboard the EINSTEIN observatory. This allowed the masses of these binaries to be estimated from the radial distances of the sources from the globular-cluster centers (Grindlay *et al.* 1984). The measured radial distances of the bursters from the globular-cluster centers agree with the assumed binary masses of $\sim 2M_{\odot}$.

The Chandra new-generation X-ray observatory with an angular resolution of $0'.5$ has allowed the localizations of known X-ray sources to be significantly improved. This, in turn, makes it possible to identify these objects more reliably in the optical and radio ranges (see, e.g., Heindl and Smith 2001; Revnivtsev and Sunyaev 2002). In particular, substantial progress has been made in localizing X-ray sources in globular clusters (Grindlay *et al.* 2001; Heinke *et al.* 2001; Homer *et al.* 2001).

Here, we present our localization results and estimates of the X-ray fluxes for sources in six Galactic globular clusters from Chandra observations.

OBSERVATIONS AND RESULTS

For our analysis, we used the following publicly available data from the Chandra X-ray observatory: NGC 6440—July 4, 2000 (the ACIS-S focal detector, an exposure time of ~23 ks); NGC 6441—May 23, 2000 (HRC-I, ~2.3 ks); NGC 6624—October 3, 2000 (HRC-S, ~15 ks); NGC 6652—May 23, 2000 (HRC-I, ~1.7 ks); Terzan 1—March 9, 2000 (HRC-I, ~3.6 ks); Terzan 2—March 9, 2000 (HRC-S, ~10 ks); and Terzan 6—March 9, 2000 (HRC-I, ~10 ks). The data were reduced with the CIAO v2.1.2 standard software package.

*E-mail: revnivtsev@hea.iki.rssi.ru

The positions of X-ray sources in globular clusters and some globular-cluster parameters

ID	Position of globular cluster center		Nucleus radius	$R_{1/2}$	D, kpc	Position of X-ray source		Distance from center	Luminosity, $\log(L$, erg s^{-1})
	$\alpha(2000)$	$\delta(2000)$				$\alpha(2000)$	$\delta(2000)$		
NGC 6440	$17^h48^m52\overset{s}{.}6$	$-20°21'34''$	$7''.8$	$34''.8$	6.4	$17^h48^m55\overset{s}{.}02$	$-20°21'33''.8$	$34''.03$	31.2
–	–	–	–	–	–	17 48 53.32	−20 21 41.7	12.72	32.1
–	–	–	–	–	–	17 48 53.17	−20 21 38.7	9.23	32.2
–	–	–	–	–	–	17 48 53.12	−20 21 27.0	10.1	31.2
–	–	–	–	–	–	17 48 52.93	−20 21 39.1	6.89	31.6
–	–	–	–	–		17 48 52.87	−20 21 42.5	9.31	32.0
–	–	–	–	–	–	17 48 52.85	−20 21 34.1	3.51	32.0
–	–	–	–	–	–	17 48 52.64	−20 21 40.6	6.62	31.6
–	–	–	–	–	–	17 48 52.41	−20 21 32.2	3.22	32.3
–	–	–	–	–	–	17 48 52.16	−20 21.32.4	6.39	32.5
–	–	–	–	–	–	17 48 51.98	−20 21 46.7	15.40	31.7
–	–	–	–	–	–	17 48 51.87	−20 21 33.9	10.27	31.0
NGC 6441	17 50 12.9	−37 03 04	6.6	38.4	11.2	17 50 12.74	−37 03 06.8	3.39	36.6
NGC 6624	18 23 40.5	−30 21 40	3.6	49.2	8.0	18 23 40.46	−30 21 40.3	0.60	37.2
Terzan 1	17 35 46.8	−30 28 52.7	2.4	229.2	6.2	17 35 45.61	−30 29 00.2	30.2	32.4
Terzan 2	17 27 33.4	−30 48 08	1.8	91.2	8.7	17 27 33.15	−30 48 07.8	3.23	36.8
Terzan 6	17 50 46.4	−31 16 31	3.0	26.4	9.5	17 50 46.90	−31 16 29.5	6.58	35.2

We also used observational data for the globular clusters NGC 6652 and NGC 1851. Since the results of our analysis agree, within the error limits, with the localizations published by Heinke *et al.* (2001) and Homer *et al.* (2001), we do not present the results of our analysis for these observations here and refer the interested reader to the corresponding papers.

The Chandra design localization accuracy is $\sim 1'$. However, an analysis of simultaneous optical and X-ray observations of various sky fields shows that the Chandra ($1\text{-}\sigma$) localization accuracy of X-ray sources is $\sim 0''.6$ (see http://asc.harvard.edu/mta/ASPECT/cel_loc/cel_loc.html and http://asc.harvard.edu/mta/ASPECT/celmon/).

To detect and locate the sources, we used the *wavdetect* procedure of the CIAO2.0 package. In this procedure, the source confidence level is determined by estimating the observed background fluctuations. Since all the sources under study are close to the center of the field of view, their images are compact and the statistical uncertainty in the source position is negligible compared to the previously mentioned systematic uncertainty.

Our observations of all six globular clusters revealed at least one X-ray source with a detection confidence level above 4σ within the radius $R_{1/2}$ containing half of the cluster mass. Twelve sources were detected in the globular cluster NGC 6440 within $R_{1/2}$. Note that the only source found in the globular cluster Terzan 1 does not coincide in position with the previously observed bright X-ray burster MX1733-30. Thus, the Chandra observations put an upper limit on the flux from MX1733-30, $L_x \lesssim 4 \times 10^{32}$ erg s^{-1}. It should be borne in mind, however, that if the burster XB1733-30 in its off state has a very soft spectrum (with an effective temperature of $kT \sim 0.1$–0.2 keV; see Campana *et al.* 2000), much of the soft X-ray radiation with $h\nu \lesssim 1$–2 keV can be absorbed on the line of sight.

Since the HRC detector with a very low spectral resolution was used in all our observations except those of NGC 6440, a spectral analysis of the detected sources cannot be performed. To transform the instrumental counts to the energy fluxes from the sources, we used an arbitrary spectral model, a bremsstrahlung model with the temperature $kT =$ 2 keV (the energy range 0.5–7.0 keV). Thus, it should be remembered that our luminosity estimates for the X-ray sources have a systematic uncertainty that stems from the fact that the actual shapes of their

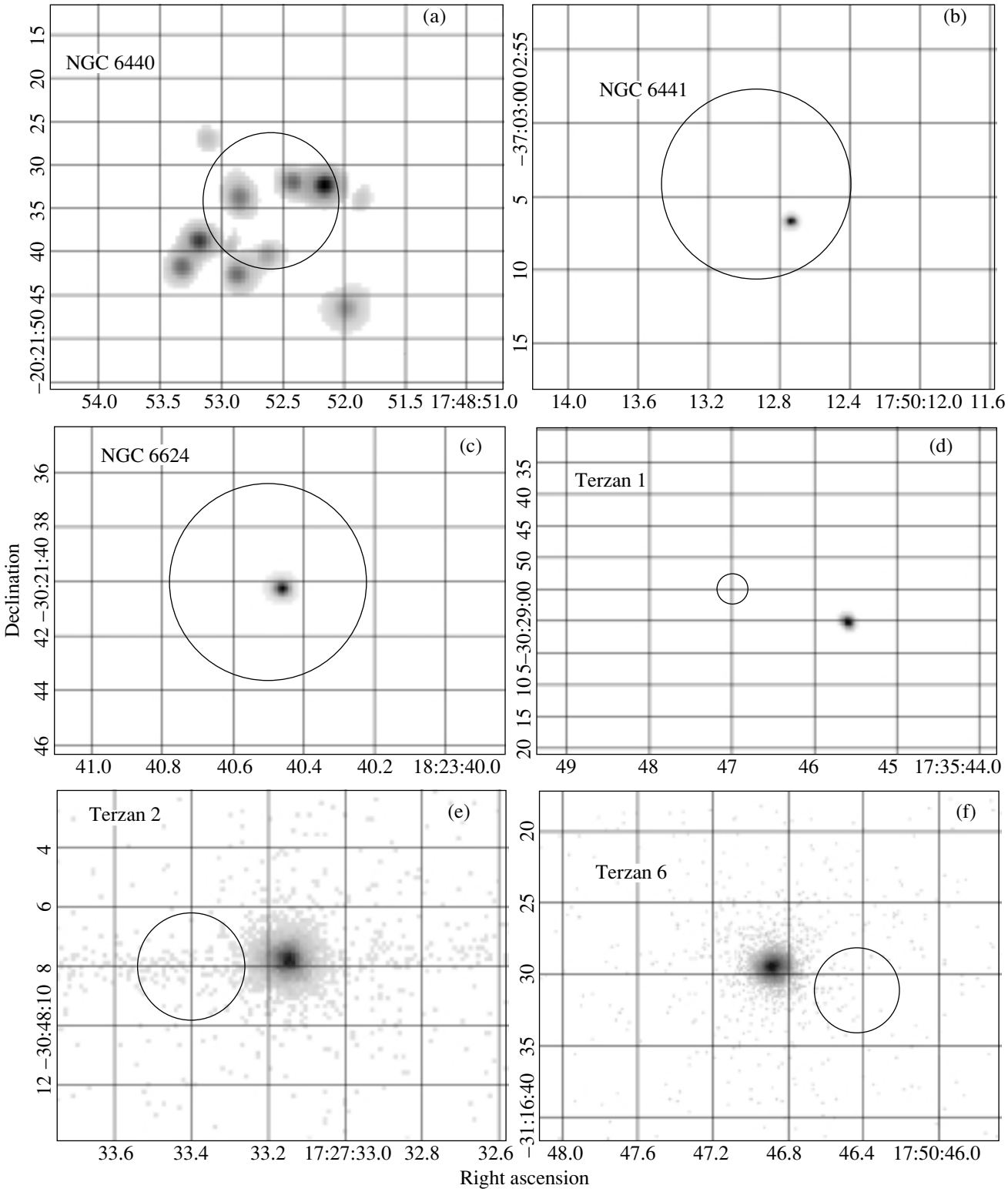

Chandra (0.5–7 keV) images of the globular clusters. The circle indicates the location and size of the globular-cluster nucleus.

spectra are unknown. We plan to perform a spectral analysis of the sources in NGC 6440 in a separate paper.

The table contains the positions of the detected bright X-ray sources. It also gives some parameters of the globular clusters (positions of their centers; nucleus radii; and distances to the clusters). The parameters of the globular clusters except for Terzan 1 were taken from the catalog by Harris (1996). For the cluster Terzan 1, we used data from the catalog by Webbink (1985).[1] The figure shows the Chandra X-ray images of the globular clusters. The circles in the panels indicate the locations and sizes of the globular-cluster nuclei.

Note that according to the Chandra observations, the X-ray source in the globular cluster NGC 6441 is at a distance of $\sim 1\farcs6$ from the position of star U1, which was suggested as an optical counterpart of this source (Deutsch *et al.* 1998). Such a large separation between the positions of the X-ray source and its presumed counterpart calls into question the optical identification of the X-ray source. The localization of the X-ray source in the globular cluster NGC 6441 given in the Table suggests that it lies closer to the cluster center than assumed previously. The new position does not rule out its identification with one of the blue stars that are also described in Deutsch *et al.* (1998).

CONSLUSIONS

We have presented the results of our analysis of the Chandra observations for six Galactic globular clusters. At least one X-ray source was detected in each globular cluster within the radius containing half of the cluster mass. Twelve X-ray sources were detected in the globular cluster NGC 6440; one of them coincides in position with the previously observed source MX1746–20 (Johnston *et al.* 1995). The only source found in Terzan 1 does not coincide in position with the previously observed burster XB1733-30 (Pavlinsky *et al.* 2001; Johnston *et al.* 1995). The localization accuracy of the X-ray sources in Terzan 2, NGC 6624, Terzan 6, and NGC 6440 has improved by a factor of 3 to 10 compared to the ROSAT and EINSTEIN results.

ACKNOWLEDGMENTS

We used data from the Chandra Observatory electronic archive (http://asc.harvard.edu/cda/). This study was supported in part by the program "Astronomy: Nonstationary Astronomical Objects" of the Russian Academy of Sciences.

REFERENCES

1. J. Bahcall and J. Ostriker, Nature **256**, 23 (1975).
2. S. Campana, L. Stella, S. Mereghetti, and D. Cremonesi, Astron. Astrophys. **358**, 583 (2000).
3. G. Clark, Astrophys. J. **199**, 143 (1975).
4. E. W. Deutsch, S. F. Anderson, B. Margon, *et al.*, Astrophys. J. **493**, 775 (1998).
5. J. Grindlay, Astrophys. J. **221**, 234 (1978).
6. J. Grindlay, P. Hertz, and J. Steiner, Astrophys. J. Lett. **282**, L13 (1984).
7. J. Grindlay, C. Heinke, P. Edmonds, *et al.*, Science **292**, 2290 (2001).
8. W. Harris, Astron. J. **112**, 1487 (1996).
9. W. Heindl and D. Smith, astro-ph/0107469 (2001).
10. C. Heinke, P. Edmonds, and J. Grindlay, Astrophys. J. (2001) (in press); astro-ph/0107513.
11. L. Homer, S. Anderson, and B. Margon, Astrophys. J. **550**, 155 (2001).
12. P. Hut, S. McMillan, J. Goodman, *et al.*, Publ. Astron. Soc. Pac. **104**, 981 (1992).
13. H. Johnston, F. Verbunt, and G. Hasinger, Astron. Astrophys. Lett. **298**, 21 (1995).
14. M. Pavlinky, S. Grebenev, A. Lutovinov, *et al.*, Pis'ma Astron. Zh. **27**, 345 (2001) [Astron. Lett. **27**, 297 (2001)].
15. M. G. Revnivtsev and R. A. Sunyaev, Pis'ma Astron. Zh. **28**, 22 (2002) [Astron. Lett. **28**, 19 (2002)].
16. R. Webbink, in *Proceedings of the IAU Symposium no. 113 "Dynamics of Star Clusters," Princeton, 1984,* Ed. by J. Goedman and P. Hut (D. Reidel, Dordrecht, 1985), p. 541.

Translated by N. Samus'

[1] The coordinates of the center of the globular cluster Terzan 1 in Harris (1996) significantly differ from those in other catalogs. The table gives the coordinates from Webbink (1985).

Astronomy Letters, Vol. 28, No. 4, 2002, pp. 241–250. Translated from Pis'ma v Astronomicheskiĭ Zhurnal, Vol. 28, No. 4, 2002, pp. 281–291.

A Nonlinear Theory of Stellar Wind with Allowance for the Influence of Relativistic Particles

D. G. Logunov and I. N. Toptygin*

St. Petersburg State Technical University, ul. Politekhnicheskaya 29, St. Petersburg, 195251 Russia

Received October 15, 2001

Abstract—We solve the nonlinear problem of the dynamics of a steady-state, spherically symmetric stellar wind by taking into account particle acceleration to relativistic energies near the shock front. The particles are assumed to be accelerated through the Fermi mechanism, interacting with stellar-wind turbulence and crossing many times the shock front that separates the supersonic and subsonic stellar-wind regions. We take into account the influence of the accelerated particles on hydrodynamic plasma-flow parameters. Our method allows all hydrodynamic parameters of the shock front and plasma in the supersonic region to be determined in a self-consistent way and the accelerated-particle energy spectrum to be calculated. Our numerical and analytic calculations show that the plasma compression ratio at the shock front increases compared to the case where there are no relativistic particles and that the velocity profile in the supersonic region acquires a characteristic kink. The shape of the energy spectrum for the accelerated particles and their pressure near the front are essentially determined by the presumed dependence of the diffusion coefficient on particle energy, which, in turn, depends on the scale distribution of turbulent pulsations and other stellar-wind inhomogeneities. © *2002 MAIK "Nauka/Interperiodica".*

Key words: *plasma astrophysics, hydrodynamics and shock waves, stellar wind, nonlinear theory, particle acceleration*

INTRODUCTION

The mass and energy ejections from stars are a critical factor that determines the state and properties of the interstellar medium. Apart from the ejections of supernova shells, stellar winds play a major role in these processes. These winds can produce cavities several tens of parsecs in size and their mechanical energy is close to the energy released during supernova explosions (Lozinskaya 1992). A consistent quantitative theory of stellar-wind outflow accompanied by the formation of several shock fronts was developed by Weaver *et al.* (1977). However, these authors disregarded an important phenomenon near the shock front, the acceleration of a fraction of particles from the ambient plasma to relativistic energies. Estimates show (Axford *et al.* 1978; Berezhko *et al.* 1988; Toptygin 1997) that a significant fraction (several tens of percent) of the shock mechanical energy can transfer to the accelerated particles. This results in a substantial modification of the hydrodynamic flow and in a change of its observed parameters [see, e.g., Toptygin (2000), where this effect was estimated for a supernova explosion].

Investigation of particle acceleration by a stellar wind is also of interest in connection with the origin of cosmic rays and the explanation of their composition and shape of the energy spectrum (Berezhko *et al.* 1988; Toptygin 1999; Klepach *et al.* 2000), as well as the electromagnetic emissions in various frequency ranges. The above authors ignored the inverse effect of the accelerated particles on the stellar wind.

Here, we solve the nonlinear problem of outflow into a homogeneous medium of a strong stellar wind that is capable of accelerating particles to relativistic energies. In this case, a system of two shock waves separated by a contact discontinuity is formed (Weaver *et al.* 1977). The system of discontinuities produced during such outflow is schematically shown in Fig. 1. The inner cavity a is filled with a wind that freely expands at velocity u_1; the wind density varies as

$$\rho(R) = \frac{dM}{dt}(4\pi R^2 u_1)^{-1}.$$

The freely expanding wind region is separated from the decelerated wind layer by the shock front I; the layer b contains the wind gas heated at the shock front I and the gas of the cold shell c evaporated into the hot wind region. The shell c is the interstellar gas swept up and heated by the shock separated from the undisturbed interstellar gas d by the shock front II and from the hot wind by the contact discontinuity R_c.

*E-mail: int@cosmos.hop.stu.neva.ru

1063-7737/02/2804-0241$22.00

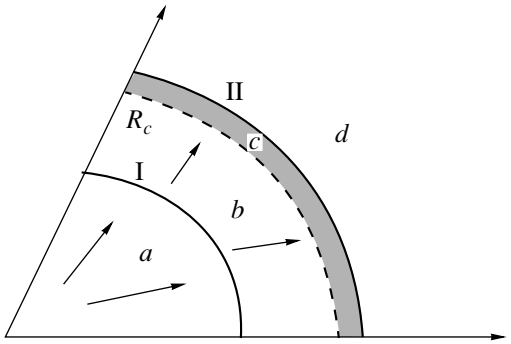

Fig. 1. Structure of the shock waves and contact discontinuities of an ejected supernova shell.

The two waves and the contact discontinuity move away from the star and gradually decelerate, with the outer shock propagating much faster than the inner shock.

For O and WR stars, the mass flux is typically $\dot{M} = J = (10^{-5}{-}10^{-7})M_\odot/\mathrm{yr}$ at initial outflow velocities of the order of $(2{-}3) \times 10^3$ km s^{-1}. For these stellar-wind parameters, self-similar solutions show that for time scales larger than $\sim 10^4$ yr, the shock velocities ($\sim$10–15 km s^{-1}) are much lower than the wind velocity and that the radius of the inner shock is small compared to the radius of the outer shock front. More detailed calculations indicate that the region inside the shock front nearest the star plays a major role in the acceleration, because the mechanical energy density of the plasma flow in this region is highest. The wind outflow time for stars of the above spectral types is of the order of 10^5–10^7 yr. Thus, at the longest final outflow stage, we may use a rough model in which the stellar wind is decelerated to subsonic velocities by a single steady-state spherically symmetric shock front that governs the generation of relativistic particles.

THE INFLUENCE OF RELATIVISTIC PARTICLES ON THE GAS DYNAMICS OF STELLAR WIND

To describe the system under consideration, we must use the gas-dynamical conservation laws for the mass, momentum, and energy fluxes, the equation of state for a nonrelativistic gas, and the kinetic equation that describes the accelerated-particle dynamics. The gas-dynamical equations must include the macroscopic quantities related to the presence of accelerated particles: their pressure and the energy flux carried away from the system. The particle escape from the system stems from the fact that the geometric sizes of the front and the acceleration time are finite and that the transport mean free path of the particles being accelerated increases with their energy. An analysis for a plane geometry (Toptygin 1997) shows that this effect can strongly affect the shock structure if an appreciable fraction of energy transfers to the accelerated particles.

In the steady-state spherically symmetric case, the conservation laws can be written as

$$4\pi r^2 \rho u = J = \mathrm{const}, \tag{1}$$

$$\frac{J}{4\pi r^2}\frac{du}{dr} + \frac{dP_g}{dr} + \frac{dP_c}{dr} = 0, \tag{2}$$

$$\frac{Ju^2}{2} + 4\pi r^2 \left\{ \frac{\gamma_\mathrm{g}}{\gamma_\mathrm{g}-1} u P_\mathrm{g} \right. \tag{3}$$

$$\left. + \frac{\gamma_\mathrm{c}}{\gamma_\mathrm{c}-1} u P_\mathrm{c} - \frac{\overline{\kappa}(r)}{\gamma_\mathrm{c}-1}\frac{dP_\mathrm{c}}{dr} \right\} + S(r) = \mathrm{const},$$

where ρ is the density of the plasma flow; u is its velocity; P_g is the nonrelativistic gas pressure; P_c is the accelerated-particle pressure; $\overline{\kappa}(r)$ is the diffusion coefficient averaged over the accelerated-particle distribution function; γ_g and γ_c are the polytropic indices for the nonrelativistic gas and the accelerated particles, respectively; and $S(r)$ is the energy flux of the escaping particles.

The first equation of this system expresses the conservation law for the mass flux, the second equation expresses the conservation law for the momentum flux (Euler equation), and the last equation is the energy conservation law. The radial energy flux density of the accelerated particle in Eq. (3) is given by

$$q_\mathrm{c} = -\overline{\kappa}(r)\frac{dW_\mathrm{c}}{dr} + u(W_\mathrm{c} + P_\mathrm{c}), \tag{4}$$

in which W_c is the energy density of the accelerated particles related to their pressure P_c by $P_\mathrm{c} = (\gamma_\mathrm{c} - 1)W_\mathrm{c}$, where $\gamma_\mathrm{c} = 4/3$ if the particles were accelerated to energies $E \gg mc^2$.

For the nonrelativistic stellar-wind component, we take the equation of state in the form of a polytrope

$$P_\mathrm{g} \propto \rho^{\gamma_\mathrm{g}}. \tag{5}$$

If the gas entropy is constant and if there are no internal energy sources, for example, heating through turbulence, then we have an adiabatic process. In a monoatomic nonrelativistic gas, which the plasma around the shock front may be assumed to be, the adiabatic index is $\gamma_\mathrm{g} = 5/3$. Additional plasma heating by any sources can be taken into account by changing the polytropic index.

The kinetic equation for the accelerated-particle distribution function $N(r,p)$ in the spherically symmetric case can be written as

$$\frac{1}{r^2}\frac{\partial}{\partial r} r^2 \kappa(r,p)\frac{\partial N}{\partial r} \tag{6}$$

$$-u(r)\frac{\partial N}{\partial r}+\frac{p}{3}\frac{\partial N}{\partial p}\frac{1}{r^2}\frac{d(r^2u)}{dr}=-Q(r,p),$$

where $u(r)$ is the hydrodynamic plasma velocity, $\kappa(r,p)$ is the diffusion coefficient, and $Q(r,p)$ is the injection rate. The escaping particles should also be included in the latter function.

This equation must be solved separately in the supersonic ($r<r_0$) and subsonic ($r>r_0$) regions. If the corresponding distribution functions are denoted by N_1 and N_2, then the boundary conditions at the shock front $r=r_0$ and on the boundaries of the regions under consideration take the form

$$N_1(r,p)\stackrel{r\to 0}{\longrightarrow}0,\quad N_2(r,p)\stackrel{r\to\infty}{\longrightarrow}0 \qquad (7a)$$

and

$$\left.\begin{array}{c}N_1(r,p)=N_2(r,p)\\ \kappa_1\dfrac{\partial N_1}{\partial r}+\dfrac{u_*}{3}p\dfrac{\partial N_1}{\partial p}=\kappa_2\dfrac{\partial N_2}{\partial r}+\dfrac{u_2}{3}p\dfrac{\partial N_2}{\partial p}+Q_0,\end{array}\right\} \qquad (7b)$$

$$\text{for}\quad r=r_0,$$

where κ_1, κ_2, u_*, and u_2 are the corresponding quantities on the inner and outer surfaces of the shock front. These boundary conditions suggest that the particles are injected into the acceleration at the shock front from the background plasma. The particles that arrive from outside can be taken into account by modifying the boundary condition for $r\to\infty$.

Below, to analyze the degree of accelerated-particle influence on the shock parameters, we use the following dimensionless quantities: the global compression ratio $\sigma=u_1/u_2$ (the ratio of the velocity in the region undisturbed by the accelerated particles to the velocity on the outer surface of the shock front), the fraction of the stellar-wind energy transferred to the accelerated particles $\eta=4\pi r_0^2P_{c0}/Ju_1$, the dimensionless stellar-wind velocity $v(r)=u(r)/u_1$, and the dimensionless coordinate $x=r/r_0$. An analysis of the conservation laws allows η to be related to $v(x)$. Thus, integrating Eq. (2) from 0 to r_0 yields

$$\eta=1-v_*+2\int_0^1\frac{1-v(t)}{t^3}dt. \qquad (8)$$

Knowing the distribution function, we can determine the accelerated-particle pressure P_c:

$$P_c(r)=\frac{1}{3}\int_0^\infty\frac{\partial\epsilon}{\partial p}N(p,r)p^3dp, \qquad (9)$$

where $\epsilon(p)$ is the energy of an individual particle.

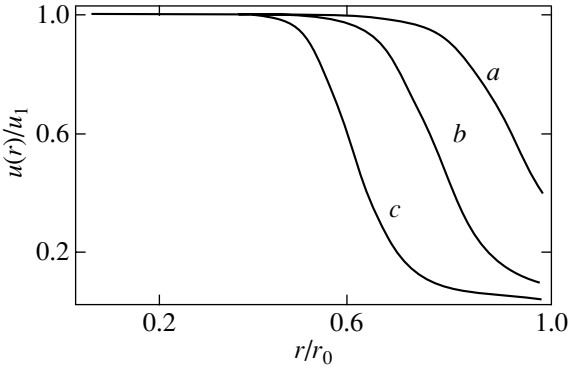

Fig. 2. Plasma velocity $u(r)/u_1$ in the inner region versus coordinate r/r_0 for $k_1=0.1$ and various compression ratios: (a) $\sigma=6.6$, (b) $\sigma=20.0$, and (c) $\sigma=80.0$.

Eqs. (1)–(3) were numerically solved in the inner and outer regions. For $r<r_0$, we assumed a distance dependence of the diffusion coefficient in the form $\kappa(r)=\kappa r/r_0$. Its increase with distance results from a reduction in the magnetic fields with decreasing plasma density. The measure of influence of the accelerated particles on the stellar-wind gas dynamics was the quantity η, which characterizes their pressure at the front. Depending on this parameter and on the dimensionless particle diffusion coefficient $k_1=\kappa_1/u_1r_0$, we obtain different onflow velocity profiles (see Figs. 2–4). In the inner region (Figs. 2, 3), a characteristic feature of the velocity profiles is the transition from a simple prefront at low accelerated-particle pressures (curve a) to a more complex shape with a kink at higher pressures (curves b, c). The depth of particle penetration into the inner region depends on the dimensionless diffusion coefficient k_1. A comparison of Figs. 2 and 3 shows that for $k_1\ll 1$, the velocity profile is deformed only near the shock front. The general pattern of the curves is the same as that for a plane shock front (Toptygin 1997). At a high relative pressure of the accelerated particles, $\eta>0.5$, the jump in velocity u_*-u_2 at the thermal front is small compared to the change in velocity u_1-u_* in the prefront and the shock front becomes smeared, acquiring a thickness of $\sim\kappa_1/u_1$. In the outer region (Fig. 4), the velocity variations at a large distance behind the front follow a law similar to $u_2\propto r^{-2}$.

At moderately high pressures, the numerical solutions can be satisfactorily fitted with functions of the form

$$v_1(x)=1-(v_*-1)x^{\mu_1}. \qquad (10)$$

The parameter μ_1 is determined by the condition that the velocity (10), when substituted in Eq. (8), gives the correct pressure η. This condition yields

$$\mu_1=\frac{2\eta}{\eta+v_*-1}.$$

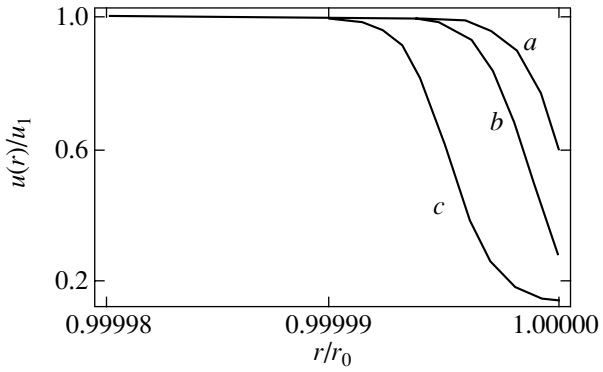

Fig. 3. Plasma velocity $u(r)/u_1$ in the inner region versus coordinate r/r_0 for $k_1 = 10^{-6}$ and various compression ratios: $(a)\,\sigma = 6.6$, $(b)\,\sigma = 13.3$, and $(c)\,\sigma = 16.6$.

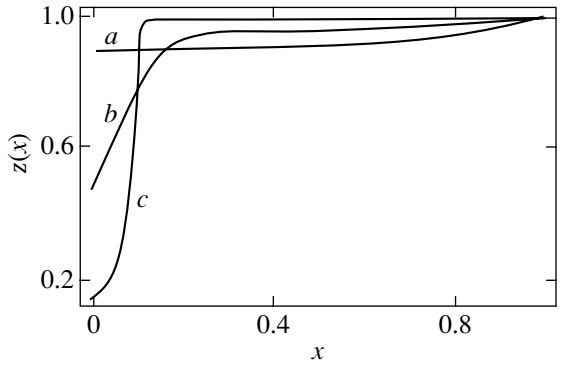

Fig. 4. Plasma velocity $z(x) = v_2(r)r^2/u_2 r_0^2$ in the outer region versus coordinate $x = r_0/r$ for various compression ratios ($k_2 = 0.1$): $(a)\ \sigma = 4.05$, $(b)\ \sigma = 9.46$, and $(c)\,\sigma = 48.66$.

When v_* decreases, a more complex fit is required starting from some value. In this case, the velocity profile is characterized by the following four parameters: v_*, η, the point of inflection x_p, which is the root of the equation $d^2v_1/dx^2 = 0$, and the velocity $v_p = v(x_p)$ at the point of inflection. The velocity variation with allowance for all the peculiarities noted above can be properly described with the formulas

$$v_2^a(x) = \begin{cases} 1 + (v_p - 1)\left(\dfrac{x}{x_p}\right)^{\mu_2}, & x < x_p, \\ v_p\left(\dfrac{x_p}{x}\right)^{\lambda}, & x \geq x_p, \end{cases} \qquad (11)$$

where the parameters μ and λ must be chosen numerically. As our detailed calculations show, these formulas satisfactorily fit the numerical solutions, so the error does not exceed 2–3% in most cases.

In the subsonic wind region, $r > r_0$, the velocity variation with distance can be described with an accuracy of the order of 10% by the dependence

$$u(r) = u_2(r_0/r)^2. \qquad (12)$$

The contribution of the outer region to the acceleration is negligible, because the mechanical energy of the plasma flow in this region is low compared to the supersonic region. Besides, the contribution of the outer region decreases with increasing accelerated-particle pressure because of the decrease in velocity u_2. Therefore, we take the above approximate dependence for $u(r)$ in the outer region.

SOLVING THE KINETIC EQUATION AND CALCULATING THE ACCELERATED-PARTICLE SPECTRUM

The velocity profiles derived in the preceding section can be realized only if the accelerated-particle spectra and fluxes calculated with them provide the required pressure P_c. For the problem to be self-consistent, we must solve the kinetic equation (6) by specifying the functions $u(r)$ and $\kappa(r, p)$. In accordance with the above results, we fit the velocity profiles in the inner and outer regions with expressions (10) and (12), respectively. Determining the diffusion coefficient and its energy dependence is one of the most complex problems in the physics of stellar winds and supernova remnants, because it is not enough to have estimates of the integrated parameters for the disturbed regions to solve this problem. We must also know the magnetic fields in the turbulent region, including those generated by the accelerated particles themselves, and the scale distribution. Since there are no corresponding direct observational data, we estimate the diffusion coefficient indirectly.

It would be natural to assume that the particle diffusion coefficient in a strongly disturbed supersonic stellar-wind region cannot be larger than the mean diffusion coefficient averaged over the entire region of cosmic-ray confinement in the Galaxy, i.e., over its disk and halo: $\kappa < \kappa_{\rm Gal}$. The latter for particles with energy of several GeV, as suggested by observational data (Beresinsky *et al.* 1990), is of the order of $\kappa_{\rm Gal} \approx 10^{28}$ cm^2 s^{-1}.

The dependence of the diffusion coefficient on particle momentum is determined by the structure of the stellar-wind inhomogeneities, their magnitude, and scale distribution. If the wind has a clumpy structure and if there are many clumps in it undergoing collisions because of the velocity difference, then one might expect a large number of shock fronts with different strengths to be formed in the supersonic region. This model, as applied to the Galactic disk, was previously considered by Bykov and Toptygin (1987). It yields a momentum-independent diffusion coefficient at the particle energies that satisfy the condition $r_g(\epsilon) \ll L$, where r_g is the gyroradius and L is

the mean separation between the strong shock fronts (at which the relative jumps in magnetic field are of the order of or larger than unity). At $r_g(\epsilon) \gg L$, the particle transport mean free path increases as $\Lambda(p) \propto p^2$ and the particles emerge from the acceleration regime. In this case, it is convenient to model the diffusion coefficient by a step momentum dependence (Toptygin 1997),

$$\kappa_1(r,p) = \begin{cases} \kappa_1 r/r_0, & p < p_m \\ \infty, & p \geq p_m. \end{cases} \quad (13)$$

This also includes the previously used radial dependence. The maximum momentum p_m is determined by the condition

$$r_g(p_m) \approx L, \quad p_m \approx ZeBL/c, \quad (14)$$

where Z is the ion charge number, and the transport mean free path $\Lambda \approx L$ at $r_g \ll L$ is of the order of the mean separation between the strong fronts. The diffusion coefficient (13) describes a situation when the particles with $p \geq p_m$ cease to interact with the plasma (escaping particles).

In the model under consideration, turbulence acts as an external (relative to the particles being accelerated) factor that is mainly determined by the dynamics of the stellar wind itself. Other models in which Alfven and other fluctuations are generated by the particles being accelerated are also possible (Volk and Bierman 1988; Fedorenko 1990). In the highly nonlinear limiting case of the most intense turbulence generation, the diffusion coefficient reaches the lowest value allowable by the magnetic-field strength:

$$\kappa_1(p) \approx (1/3)vr_g \quad (15)$$

(Bohm limit); i.e., the particle transport mean free path is equal to the gyroradius in order of magnitude: $\Lambda(p) \approx cp/ZeB$.

Below, we calculate the particle acceleration for the above two turbulence models. The particles are assumed to be injected into the acceleration process in a narrow region around the front at a constant rate Q_0 from a monoenergetic background of particles with momenta p_0. The particles also escape from the system at a constant rate Q_m from the narrow region around the front when their momentum reaches p_m. The following injection functions correspond to these assumptions

$$Q(r,p) = Q_0 p_0^{-2}\delta(r-r_0)\delta(p-p_0) - Q_m p_0^{-2}\delta(r-r_0)\delta(p-p_m). \quad (16)$$

The kinetic equation (6) with the right-hand part (16) can be solved by using the Mellin transform in p:

$$\overline{N}(r,s) = \int_0^\infty N(r,p)p^{s-1}dp. \quad (17)$$

For the outer region, after substituting velocity (12), we derive an easily integrable equation. The solution that satisfies the boundary condition at infinity can be written as

$$\overline{N}_2(x,s) = C_2(s)\left[1 - \exp\left(-\frac{1}{xk_2}\right)\right]. \quad (18)$$

In what follows, we use the notation $k_{1,2} = \kappa_{1,2}/u_{1,2}r_0$ for the dimensionless diffusion coefficients.

To solve the kinetic equation (6) in the inner region with velocity (10), we must introduce a new independent variable $\xi = x^\mu$, whereupon we derive an equation whose solution, limited at zero, can be expressed in terms of the degenerate hypergeometric function $F_1(\alpha,\beta,t)$:

$$\overline{N}_1(x,s) = C_1(s)x^{\nu(s)-1} \times F_1\left(\frac{s}{3} - \frac{1}{\mu} + \frac{2s}{3\mu} + \frac{\nu(s)}{\mu}, 1 - \frac{1}{2k_1} + \nu(s), \frac{(1-v_*)x^\mu}{\mu k_1}\right), \quad (19)$$

where

$$\nu(s) = \frac{1}{2k_1} + \frac{\sqrt{24sk_1 + (6k_1-3)^2}}{6\mu k_1}.$$

The integration constants $C_1(s)$ and $C_2(s)$ can be determined from the boundary conditions at the front.

The inverse Mellin transform is given by the integral

$$N(x,p) = \frac{1}{2\pi i}\int_{\beta-i\infty}^{\beta+i\infty} \overline{N}(x,s)p^{-s}ds. \quad (20)$$

This integral is the sum of residues at all singular points left of the integration contour. The cut in the complex s plane attributable to the presence of a radical in the expression for $\nu(s)$ lies on the negative real semiaxis of the complex s and does not affect the distribution function for $p > p_0$. In our case, as calculations show, there is a single pole and the distribution function at the front takes the form

$$N_1(1,p) = N_{10}(\alpha)(p/p_0)^{-\alpha}, \quad (21)$$

where

$$N_{10}(\alpha) = Q_0 R(\alpha)/(p_0^3\Phi'(\alpha)u_1),$$

$$R(\alpha) = x^{\nu(\alpha)-1}F_1\left(\frac{\alpha}{3} - \frac{1}{\mu} + \frac{2\alpha}{3\mu} + \frac{\nu(\alpha)}{\mu}, 1 - \frac{1}{2k_1} + \nu(\alpha), \frac{1-v_*}{\mu k_1}\right),$$

α is the root of the equation $\Phi(s) = 0$, and $\Phi(s)$ is the determinant of the system of linear equations which $C_1(s)$ and $C_2(s)$ satisfy:

$$\Phi(s) = \left\{k_1\frac{\partial N_1}{\partial r} - \frac{\Delta}{3}sN_1 + \frac{N_1}{\exp(1/\sigma k_2) - 1}\right\}\Bigg|_{r-r_0}. \quad (22)$$

Using the normalization condition

$$\int_{p_0}^{p_m} N_1(1,p)p^2dp = n_c, \quad (23)$$

where n_c is the accelerated-particle density at the front, we can relate Q_0 and n_c:

$$Q_0 = n_c u_1 \frac{(3-\alpha)\Phi'(\alpha)}{((p_m/p_0)^{3-\alpha} - 1)R(\alpha)}. \quad (24)$$

The accelerated-particle pressure calculated with formula (9) makes it possible to express the injection rate Q_0 in terms of η. As a result, we obtain

$$Q_0 = n_g u_1 \frac{3\eta\Phi'(\alpha)\sigma}{y_0^{\alpha-5}R(\alpha)I(\alpha, p_0, p_m)}, \quad (25)$$

where n_g is the thermal plasma particle density at the front,

$$I(\alpha, p_0, p_m) = \int_{y_0}^{y_m} \frac{y^{4-\alpha}dy}{\sqrt{1+y^2}}, \quad (26)$$

$$y_0 = \frac{p_0}{mc}, \quad y_m = \frac{p_m}{mc}.$$

The condition for the distribution function to become zero at $p > p_m$ allows the rate of particle escape to be related to the injection rate:

$$Q_m = Q_0\left(\frac{p_0}{p_m}\right)^{\alpha-3}. \quad (27)$$

Using this result, we can calculate the dimensionless energy flux carried away by the escaping particles:

$$s_m = \frac{Q_m c p_m}{u_1 P_c} = \frac{3(p_m/m_p c)^{4-\alpha}\Phi'(\alpha)}{R(\alpha)}. \quad (28)$$

The results of our calculations with the diffusion coefficient (13) for large Mach numbers are given in Table 1.

CALCULATING THE SPECTRUM FOR A POWER DEPENDENCE OF THE DIFFUSION COEFFICIENT

If the diffusion coefficient is formed during the resonant particle interaction with wave turbulence, then its momentum dependence is a power law

$$\kappa(p) \sim p^\beta, \quad (29)$$

with an index β in the range 1 to 2. For the strongest possible turbulence generated by the particles being accelerated, the regime with the Bohm diffusion coefficient (15) appears to be realized.

Given that the condition for equality of the function N_1 and N_2 at the front must be satisfied, the solution in the outer region can be written as

$$N_2(x,p) = N_1(1,p)\frac{1-\exp(-1/xk_2p)}{1-\exp(-1/k_2p)}. \quad (30)$$

Using this expression, the condition for equality of the particle fluxes at the front [the second condition in (7b)] can be represented as

$$\kappa_1(p)\frac{\partial N_1}{\partial r} + \frac{\Delta}{3}p\frac{\partial N_1}{\partial p} + F(p)N_1(p) = Q_0\delta(p-p_0)/p_0^2 \quad \text{for} \quad r = r_0, \quad (31)$$

where $\Delta = v_* - 1/\sigma$ is the jump in velocity at the front, $\kappa_1(p)$ is the diffusion coefficient on the inside of the front, and

$$F(p) = \frac{\exp(1/k_2p^\beta)}{1-\exp(1/k_2p^\beta)}. \quad (32)$$

Thus, calculating the distribution function reduces to solving the kinetic equation (4) with condition (31) and with allowance for the finiteness of the function when $r \to 0$.

Below, we assume a linear dependence of the diffusion coefficient on coordinate and momentum, i.e., $\kappa_1(r,p) = k_1rp$ (in the right-hand part, k_1, as well as k_2, are constants), although all calculations can easily be generalized to a power dependence on momentum with an arbitrary index.

It is easy to verify that the partial solution to the kinetic equation (6), which is finite for $r \to 0$, at a constant velocity and at $Q(r,p) = 0$ is the function

$$N^{(0)}(r,p,\nu) = c(\nu)r^\nu p^{\frac{3\nu}{2}}\exp\left(-\frac{3k_1\nu(\nu+2)}{2}p\right), \quad (33)$$

where $\nu > 0$ and $c(\nu)$ is the constant to be determined from the boundary condition. Using (33), the solution for $N_1(x,p)$ can be roughly represented as the series

$$N_1(r,p) = \sum_i c_{0i}x^{\nu_i}p^{\frac{3\nu_i}{2}}\exp\left(-\frac{3k_1\nu_i(\nu_i+2)}{2}p\right) \times (1 + \varepsilon a_1(p)x^\mu + \varepsilon^2 a_2(p)x^{2\mu} + \ldots). \quad (34)$$

Here, as above, $\varepsilon = 1 - v_*$ and $a_k(p)$ are unknown functions to be determined when substituted in the kinetic equation (6).

The unknown constants $c_k(\nu_i)$ and ν_i can be determined from the boundary condition (31). At a finite

Table 1. Self-consistent stellar-wind and accelerated-particle parameters for the step dependence (13) of the diffusion coefficient on momentum

k_1	v_*	η	σ	μ	α	$\log Q_0$	$\log S_\mathrm{m}$
0.1	0.999	0.001	4.0	12.32	4.266	−6.0	−6.0
	0.913	0.104	4.4	11.90	4.201	−4.2	−3.6
	0.788	0.258	5.1	11.20	4.094	−4.3	−2.8
	0.362	0.848	11.0	8.10	3.608	−7.0	−1.3
	0.286	0.979	13.9	7.30	3.502	−7.8	−1.2
10^{-3}	0.999	0.001	4.0	1.05e-3	4.002	−5.1	−2.5
	0.913	0.088	4.4	0.95e-3	3.942	−4.2	−2.1
	0.788	0.213	5.1	0.88e-3	3.847	−4.3	−1.8
	0.362	0.640	11.0	0.60e-3	3.450	−6.4	−1.2
	0.286	0.717	13.9	0.51e-3	3.372	−7.5	−1.1
10^{-6}	0.999	0.001	4.0	1.10e-6	3.999	−5.2	−2.4
	0.913	0.087	4.4	0.96e-6	3.939	−4.5	−2.1
	0.788	0.213	5.0	0.88e-6	3.845	−4.4	−1.8
	0.362	0.638	11.0	0.59e-6	3.448	−6.3	−1.1
	0.286	0.714	13.9	0.50e-6	3.371	−7.4	−1.0

number of terms in i, this condition can be satisfied only roughly. It represents the equality of the particle fluxes at the shock front; the larger the number of terms taken in the series in i, the better this condition is satisfied. To obtain the numerical values of $c(\nu_i)$ corresponding to ν_i, we can minimize the relative error of condition (31), i.e., the ratio of the absolute flux difference between the inner and outer regions to the absolute particle flux from each region, by considering this error to be a function of all the unknown constants. The larger the number of terms taken in the series in i, the smaller the momenta for which the particle fluxes are equal at the front with a given accuracy. The asymptotics of expression (31) with $N_1(p)$ in the form (34) at large momenta makes it possible to derive an equation for ν_1:

$$-\frac{\Delta}{2}\nu^2 + (1-\Delta)\nu + \frac{k_2}{\sigma k_1} = 0. \qquad (35)$$

The positive solution of this equation (the negative solution would not do because of the condition for $x \to 0$) is

$$\nu_1 = \frac{1}{\Delta} - 1 + \sqrt{\left(\frac{1}{\Delta} - 1\right)^2 + \frac{2k_2}{\Delta k_1 \sigma}}. \qquad (36)$$

When $Q(r,p) = 0$ and $\varepsilon = 0$ (an undistorted profile for nonlinear acceleration), to ensure that the fluxes be equal at large momenta ($p \to \infty$), it will suffice to take one term with ν_1. For this condition to be satisfied with a five-percent accuracy for all momenta $p \geq 10p_0$, we must take no less than 8–10 terms in the sum over i (for $k_1 = 0.001$). Minimizing the flux residual in this way, we can achieve the satisfaction of condition (31) with any prespecified accuracy for any momentum range. A characteristic plot of the relative error in particle flux equality at the front against momentum is shown in Fig. 5. We see from this figure that for all momenta $p > 30p_0$, the condition for equality of the particle fluxes at the front is satisfied with an accuracy higher than 7%.

This method makes it possible to determine only the relative values of the constants $c(\nu_i)$. One constant is always free and it can be calculated from the normalization condition:

$$\int_{p_0}^{\infty}\left(\kappa_1(p)\frac{\partial N_1}{\partial r} + \frac{\Delta}{3}p\frac{\partial N_1}{\partial p} + F(p)N_1(p)\right)p^2 dp = Q_0. \qquad (37)$$

Since the particle flux difference at the front significantly differs from zero only at small momenta, $p \sim p_0$, the normalization condition (37) corresponds to the injection function for which the particles are injected only with momenta close to p_0 and with the total rate Q_0. This injection function apparently reflects the processes during particle injection, because monoenergetic particle injection is an idealization and,

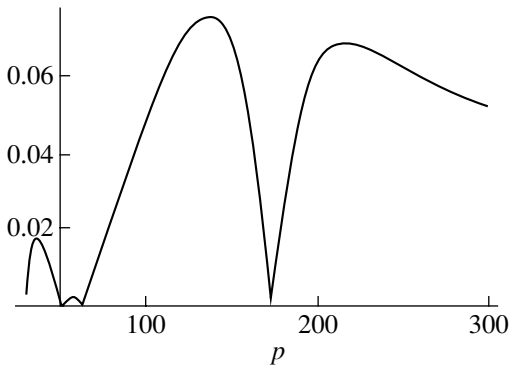

Fig. 5. The error in flux equality at the front versus momentum whe 15 terms are taken in series (34) ($\varepsilon = 0.1$).

in reality, the particles are injected with momenta in a small range near p_0.

Clearly, all constants ν_i for $i > 1$ can be determined in such a way that they are larger than ν_1. In our calculations, we also took into account the fact that only the terms with $\nu_i < \nu_{\max}$, where $3|2\nu_{\max}(\nu_{\max}+2)k_1 \approx 1$, can contribute tangibly to the distribution function and to the expression for the flux difference. At large ν for any (even small) momenta, the corresponding terms in series (34) are vanishingly small because of the exponent in expression (33). Thus, the problem reduces to determining $c(\nu_i)$ by minimizing the functional for a given discrete set of such ν_i that $\nu_1 < \nu_i \le \nu_{\max}$.

To allow for the nonlinearity of the plasma velocity profile in the inner region, we must substitute expression (34) in the kinetic equation (6) and boundary condition (31). In this case, the set of constants ν_i will be different for each order in ε; accordingly, we denote the order in $\varepsilon(\nu_{ni})$ by the first subscript n.

Substituting in the equation and then equating the terms with the same powers ϵ yield a system of coupled differential equations of the first order for $a_{ni}(p)$ (we choose $a_{0i} = 1$):

$$\frac{2}{3}p\frac{da_{ni}(p)}{dp} + A_{ni}(p)a_{ni}(p) + B_{ni}(p) = 0, \quad (38)$$

where

$$A_{ni}(p) = n(k_1\mu p(2+2\nu_{ni}+n\mu) - n\mu), \quad (38a)$$

$$B_{ni}(p) = \left\{k_1\nu_{ni}p\left(2+\nu_{ni}+\mu+\frac{\nu_{ni}\mu}{2}\right)\right. \quad (38b)$$
$$\left. + (n-1)\mu - \frac{\nu_{ni}\mu}{2}\right\}a_{n-1,i}(p) - \frac{\mu+2}{3}pa'_{n-1,i}(p).$$

The general solution to this equation is

$$a_{ni}(p) = p^{3|2n^2\mu}e^{-\alpha_{ni}(p-1)} \quad (39)$$
$$\times\left\{c_{ni} - \frac{3}{2}\int_1^p t^{-3/2n^2\mu-1}e^{\alpha_{ni}(t-1)}B_{ni}(t)dt\right\},$$

where $\alpha_{ni} = (3|2)(2+2\nu_i+n\mu)k_1n\mu$ and c_{ni} are the integration constants.

For all momenta, the term in this expression proportional to c_{ni}, which rapidly tends to zero, is much smaller than the second term, which also rapidly tends to a nonzero constant. The first term can play a significant role only at very small momenta. For such momenta, we must take a large number of terms in the series in i [formula (34)]. Because of the great computational difficulties, we restrict ourselves to constructing an approximate solution only for momenta larger than $(20-30)p_0$. Besides, the range of large momenta is of prime interest in analyzing the cosmic-ray and radiation spectra. Thus, we discard the first term in expression (39).

The remaining second term produces changes in the fluxes at the front. By performing the minimization procedure described above, we can find a new set of constants c_{ni} and ν_{ni} for each ϵ (or, equivalently, for v_*, σ or η). In practice, the smallest constants ν_{ni} undergo the largest changes because their values determine the approach of the relative particle flux at the front to zero for large momenta. For small momenta ($20p_0 \le p \le 1000p_0$), a change in ϵ causes no degradation in the accuracy with which the fluxes are equal and the constants ν_{ni} for $i \ge 2$ (in the first order) can be roughly assumed to be the same as those at $\epsilon = 0$. The results of our first-order calculations for ν_{11} at various ϵ are given in Table 2.

DISCUSSION AND CONCLUSIONS

The above methods for solving the kinetic equation allow the spectrum to be constructed for step and power dependences of the diffusion coefficient on momentum. The accelerated-particle pressure can be calculated for each injection rate by using the derived distribution function. This, in turn, allows the injection rate to be related to the set of hydrodynamic front parameters that determines the specific acceleration regime and, thus, to make the problem consistent. In practice, the calculation is complicated by the need to take into account the particle escape from the system for a step dependence of the diffusion coefficient. This necessitates concretizing the energy carried away from the system by the escaping particles even during the hydrodynamic solution followed by a reconciliation not only in the pressure P_{c0} but also in the parameter S_m, which determines this energy.

To perform numerical calculations requires estimating the dimensionless diffusion coefficients in

Table 2. First-order calculations for various ϵ for a power dependence of the diffusion coefficient

k_1	ϵ	0.00	0.01	0.05	0.1	0.15	0.2	0.3
0.1	ν_{11}	1.215	1.204	1.107	1.052	0.948	0.875	0.734
0.001	ν_{11}	1.215	1.208	1.110	1.063	0.954	0.887	0.757

order of magnitude. To this end, the following standard relation between the diffusion coefficient and the transport mean free path of fast particles can be used: $\kappa = c\Lambda(p)/3$. Assuming the limiting expression for the mean free path $\Lambda(p) = cp/eH = E/eH$, we obtain $\kappa \approx 10^{22}$ cm^2 s^{-1} for standard energy $E \approx 1$ GeV $\approx 10^{-3}$ erg and magnetic field $H \approx 10^{-6}$ G. At characteristic stellar-wind velocities $u_1 \approx 10^8$ cm s^{-1} and acceleration-region size (shock radius) $r_0 \approx 10^{19}$ cm, we estimate the dimensionless diffusion coefficient to be $k = \kappa/u_1 r_0 \approx 10^{-6}$. Since some of the parameters in these expressions are uncertain, the naturally occurring k can be higher by several orders of magnitude. Therefore, we performed our calculations for $k = 0.1$, 10^{-3}, and 10^{-6}.

The plot in Fig. 6 shows that, as in the plane case, the solution is multi-valued for a step dependence of the diffusion coefficient. The question as to which of the possible solutions occurs in nature is solved by analyzing the stability of the derived solutions against small perturbations. Such an analysis for a plane front shows that states with smaller compression ratios at equal injection rates are more stable and, hence, occur in nature.

The finite range of particle injection rates into the acceleration process for which a thermal jump can exist and the general dependence of the injection rate on the compression ratio (Fig. 6, curve b) are among the peculiarities of the solution in the plane case, which also takes place for a spherical geometry. The injection rates required for such nonlinear acceleration processes to develop in the plane and spherically symmetric cases prove to be of the same order of magnitude.

For a power dependence of the diffusion coefficient, the solution becomes single-valued and the injection rate monotonically increases with compression ratio in the range of compression ratios in which our calculations were performed (Fig. 6, curve a). In addition, there is no need to formally introduce the escape momentum, because the distribution function is normalizable at any compression ratio. Because of the exponent, the spectrum proves to be truncated. This is clearly seen in Fig. 7, where the logarithms of the distribution function are plotted against the logarithms of the momentum for $k_1 = 0.001$. The distribution function for a power dependence of the diffusion coefficient (Fig. 7, curve a) falls off sharply at momenta $p \approx 10^3 p_0$. The constant ν_1 in Eq. (34) gives the cutoff momentum. As our calculations show, the maximum dimensionless momentum is of the same order of magnitude as the characteristic inverse dimensionless diffusion coefficient: $p_m/p_0 \approx 1/k_1$. The maximum energy of the accelerated particles can also be expressed in terms of p_m: $\epsilon_m = p_m c \approx (p_m/p_0) \times 10^{-2} m_p c^2 \approx (p_m/p_0) \times 10^6$ eV. In the latter estimates, we took $p_0 \approx 10^{-2} m_p c^2$ for the injection momentum. It is clear from these estimates that under our assumptions in the model under consideration, to achieve the accelerated-particle energies

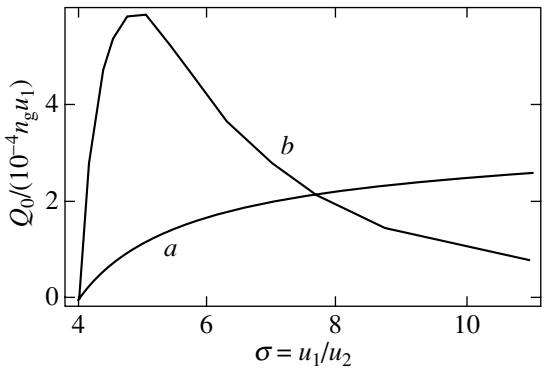

Fig. 6. Injection rate $Q_0/(10^{-4} n_g u_1)$ (n_g is the thermal particle density) versus global compression ratio $\sigma = u_1/u_2$.

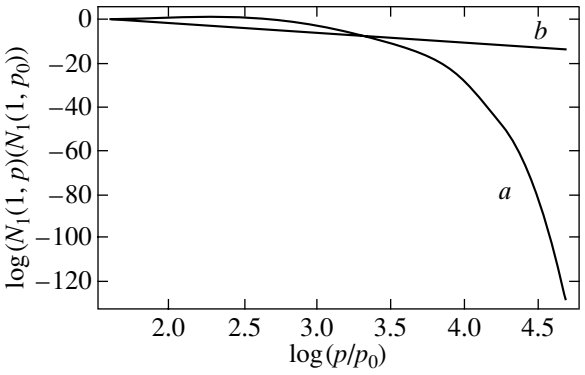

Fig. 7. Logarithm of the distribution function at the front, $\log(N_1(1,p)/N_1(1,p_0))$, versus logarithm of the momentum, $\log(p/p_0)$, for various diffusion coefficients: a—a power momentum dependence; b—a step dependence.

$\approx 10^{12}$–10^{13} eV requires dimensionless diffusion coefficients $k \approx 10^{-6}$–10^{-7}, in agreement with our limiting estimates for k. The acceleration to high energies in the model under consideration seems doubtful. The maximum energy can increase in the presence of an ensemble of shock waves produced by multiple supernova explosions in extended OB associations (Bykov and Toptygin 2001).

The temperature in a monoatomic gas behind the front of a strong shock wave, in which the total gas energy is conserved, is known to be given by

$$T_2 = \frac{3\mu_2 m_{\rm H} v_1^2}{16k}, \qquad (40)$$

where $m_{\rm H}$ is the mass of the hydrogen atom; the molecular weight is $\mu \approx 1.3$ in H I regions and $\mu \approx 0.7$ in H II regions. We noted above that the descending branch of the solution after the curve peak in Fig. 6 may be unstable. Even if we assume that the largest compression ratio with allowance for the accelerated particles cannot exceed its value reached at the curve peak in Fig. 6, the stellar-wind velocity, nevertheless, can decrease by no less than $\approx 15\%$ because of the existence of accelerated particles. Consequently, even at relatively low injection rates, $\sim 10^{-5}$–10^{-6}, the temperature behind the front can decrease by $\approx 30\%$, which, in turn, may cause a change in the thermal plasma spectrum. In addition to thermal radiation, the particle acceleration produces synchrotron radiation, most likely in the X-ray band. The possible types of radiation in such objects deserves attention and is already being studied observationally (Sako *et al.* 1999), because the physical conditions in the disturbed regions around active stars can, probably, be judged from peculiarities of the spectra.

ACKNOWLEDGMENTS

This study was supported by the Russian Foundation for Basic Research (project no. 01-02-16654).

REFERENCES

1. W. I. Axford, E. Leer, and G. Skadron, in *Proceedings of the X Leningrad Workshop on Cosmophysics* (Fiz.-Tekh. Inst. im. A.F. Ioffe Akad. Nauk SSSR, Leningrad, 1978), p. 125.
2. E. G. Berezhko, V. K. Elshin, G. F. Krymskiĭ, and S. I. Petukhov, *Generation of Cosmic Rays by Shock Waves* (Nauka, Novosibirsk, 1988).
3. V. S. Berezinskiĭ, S. V. Bulanov, V. L. Ginzburg, *et al., The Astrophysics of Cosmic Rays,* Ed. by V. L. Ginzburg (Nauka, Moscow, 1990).
4. A. M. Bykov and I. M. Toptygin, Astrophys. Space Sci. **138**, 341 (1987).
5. A. M. Bykov and I. N. Toptygin, Pis'ma Astron. Zh. **27**, 735 (2001) [Astron. Lett. **27**, 625 (2001)].
6. V. N. Fedorenko, Preprint No. 1442, FTI im. A.F. Ioffe (Ioffe Physicotechnical Institute, Russian Academy of Sciences, Leningrad, 1990).
7. E. G. Klepach, V. S. Ptuskin, and V. N. Zirakashvili, Astropart. Phys. **13**, 161 (2000).
8. T. A. Lozinskaya, *Supernovae and Stellar Wind in the Interstallar Medium* (Nauka, Moscow, 1986; American Inst. of Physics, New York, 1992).
9. M. Sako, D. A. Liedahl, S. M. Kahn, and F. Pacrels, astro-ph/9907291.
10. I. N. Toptygin, Zh. Éksp. Teor. Fiz. **112**, 1584 (1997) [JETP **85**, 862 (1997)].
11. I. N. Toptygin, Pis'ma Astron. Zh. **25**, 930 (1999) [Astron. Lett. **25**, 814 (1999)].
12. I. N. Toptygin, Pis'ma Astron. Zh. **26**, 421 (2000) [Astron. Lett. **26**, 356 (2000)].
13. H. J. Volk and P. L. Bierman, Astrophys. J. Lett. **333**, L65 (1988).
14. R. Weaver, R. McCray, J. Castor, *et al.*, Astrophys. J. **218**, 377 (1977).

Translated by V. Astakhov

Astronomy Letters, Vol. 28, No. 4, 2002, pp. 251–256. Translated from Pis'ma v Astronomicheskiĭ Zhurnal, Vol. 28, No. 4, 2002, pp. 292–297.

Frequency Dependence of the Scattering Pulse Broadening for the Crab Pulsar

A. D. Kuzmin[1*], V. I. Kondrat'ev[2], S. V. Kostyuk[3], B. Ya. Losovsky[1], M. V. Popov[2], V. A. Soglasnov[2], N. D'Amico[4], and S. Montebugnoli[4]

[1] *Pushchino Radio Astronomy Observatory, Astrospace Center, Lebedev Physical Institute, Russian Academy of Sciences, Pushchino, Moscow oblast, 142290 Russia*

[2] *Astrospace Center, Lebedev Physical Institute, Russian Academy of Sciences, Profsoyuznaya ul. 84/32, Moscow, 117810 Russia*

[3] *Moscow State University, Vorob'evy gory, Moscow, 119899 Russia*

[4] *Instituto di Radioastronomia del CNR, Italy*

Abstract—We measured the frequency dependence of the pulsar pulse broadening by scattering over a wide frequency range, from 40 to 2228 MHz, based on direct measurements of this parameter using giant pulses from the pulsar PSR B0531+21 in the Crab Nebula. Our measurements were carried out at the following seven frequencies: 40, 60, and 111 MHz at the Pushchino Radio Astronomy Observatory (Astrospace Center, Lebedev Physical Institute, Russian Academy of Sciences), 406 MHz at the Medicina Observatory (Instituto di Radioastronomia, Italy), and 594, 1430, and 2228 MHz at the Kalyazin Radio Astronomy Observatory (Astrospace Center, Lebedev Physical Institute, Russian Academy of Sciences). The measured frequency dependence of the pulse broadening by scattering $\tau_{sc}(\nu) \propto \nu^{\gamma}$, where $\gamma = -3.8 \pm 0.2$, agrees with a model Gaussian distribution of interstellar inhomogeneities ($\gamma = -4$) but falls outside the error limits of correspondence to a Kolmogorov model spectrum of inhomogeneities ($\gamma = -4.4$).

Key words: *Crab Nebula, pulsars, pulse broadening*

INTRODUCTION

Measurement of the frequency dependence of the pulse broadening by scattering $\tau_{sc}(\nu)$, which determines the choice of a model for the scattering in the interstellar medium, is the subject of this study. The frequency dependence of the pulsar pulse scattering was first predicted by Matveyenko and Lotova (1970).

The theory predicts the frequency dependence $\tau_{sc}(\nu) \propto \nu^{\gamma}$, where $\gamma = -4$ for a Gaussian distribution of interstellar inhomogeneities and $\gamma = -4.4$ for a Kolmogorov model distribution.

The frequency dependence of pulse broadening by scattering has not been adequately studied. There are few direct measurements of this dependence in a broad frequency band. Komesaroff *et al.* (1972) observed the pulsar PSR B0833−45 at four frequencies from 300 to 1410 MHz. A convolution of the pulse at 1420 MHz taken as the initial unscattered pulsar pulse with a truncated exponent representing the scattering by a thin screen was used to fit the observed pulse profiles at other frequencies. The shapes of the observed profiles agree with the frequency dependence of the broadening by scattering $\tau_{sc}(\nu) \cong 9.4 \times (\nu/300)^{-4}$, where τ_{sc} is in milliseconds and ν is the frequency in MHz. Having analyzed the pulse shape of this pulsar, Williamson (1974) concluded that it agreed best with the model of scattering in a localized region near the pulsar or near the observer. Rankin *et al.* (1970) measured the integrated profiles for the Crab pulsar PSR B0531+21 at five frequencies from 73.8 to 430 MHz. Comparing with templates based on the highest frequency profile scattered with different τ_{sc} and additionally broadened by dispersion and the receiver time constant, they obtained model profiles similar to the observed ones for an exponent of the frequency dependence $\gamma = -4$. Based on their measurements and published data in the frequency range 102 to 196 MHz, Kuzmin and Losovsky (1999) determined the frequency dependence of the pulse broadening by scattering for this pulsar, $\tau_{sc} = 25 \times (\nu/100)^{-4}$.

Based on their measurements of giant pulses from the millisecond pulsar PSR 1937+214 and on published data, Kuzmin and Losovsky (2002) determined

*E-mail: akuzmin@prao.psn.ru

1063-7737/02/2804-0251$22.00

the frequency dependence of the broadening by scattering, $\tau_{sc} \propto \nu^{-4.0\pm0.2}$.

Thus, according to the data of the above authors, the exponent of the frequency dependence is $\gamma \approx -4$, which corresponds to a Gaussian spectrum of inhomogeneities. However, the accuracy of these measurements does not rule out $\gamma = -4.4$, which corresponds to a Kolmogorov spectrum of inhomogeneities. Moreover, having measured the frequency dependence of the decorrelation band $\Delta\nu(\nu)$ for five pulsars, which is related to the pulse broadening by scattering by the theoretical relation $2\pi\tau_{sc} = 1$, Cordes *et al.* (1985) obtained a mean value of $\gamma = -4.45 \pm 0.3$. They also concluded that the frequency dependence disagrees with a Gaussian spectrum but agrees with a Kolmogorov spectrum, for which $\gamma = -4.4$.

Based on their measurements and published data for nine pulsars, Kuzmin *et al.* (1988) determined the mean $\gamma = -3.0 \pm 0.7$, which is considerably smaller than that predicted by theoretical models. A similar small estimate of the mean, $\gamma = 2.7 \pm 0.8$, for six pulsars with large dispersion measures was obtained by Kuzmin (2001).

Thus, the question concerning the exponent in the frequency dependence of the pulse broadening by scattering $\tau_{sc}(\nu) \propto \nu^{\gamma}$ and, hence, concerning the distribution of interstellar inhomogeneities is yet to be solved. Accordingly, the most complete and commonly used list of scattering broadenings τ_{sc} from the catalog by Taylor *et al.* (1995) based on the frequency dependence $\tau_{sc} \propto \nu^{-4.4}$ obtained by Cordes *et al.* (1985) should be improved and experimentally tested.

To increase the accuracy of measuring γ requires measurements of the frequency dependence $\tau_{sc}(\nu)$ in a wide frequency range. In the above studies, the frequency range of these measurements did not exceed 5 : 1. We directly measured the frequency dependence of the scattering pulse broadening for the Crab pulsar PSR B0531+21 in the widest frequency range, $\nu_{max}/\nu_{min} = 55 : 1$, from 2228 to 40 MHz.

A peculiarity of our study that extended the frequency range is the use of giant pulses from the pulsar to measure the scattering. Giant pulses are observed as very rare isolated pulses of a high intensity that considerably exceeds the mean intensity of the pulsar radio emission. This clearly distinguishes them from a regular sequence of ordinary pulses, eliminates the effect of the succeeding pulses, and enables measurements at low frequencies, at which the scattering is larger than the pulsar period. The duration of giant pulses is much shorter than the duration of ordinary pulsar pulses. This makes it possible to measure the small scattering typical of high frequencies and to extend the range of our study to this frequency band.

MEASUREMENTS AND PROCESSING

The measurements were carried out at seven frequencies: 40, 60, 111, 406, 594, 1430, and 2228 MHz. At 40 and 60 MHz, measurements were made with the DKR radio telescope at the Pushchino Radio Astronomy Observatory (Astrospace Center, Lebedev Physical Institute, Russian Academy of Sciences). A linear polarization was received. We used a 128-channel receiver with the channel bandwidth $\Delta f =$ 20 kHz. The records were made in trains, each containing 1280 individual pulses. At 111 MHz, the measurements were carried out with the BSA radio telescope at the same observatory. A linear polarization was also received. We used a 128-channel receiver with the channel bandwidths $\Delta f = 20$ and 1.25 kHz. The records were made in trains, each containing 1280 and 50 individual pulses, respectively. To check whether the pulses belonged to the Crab pulsar, we processed the records in separate groups of frequency channels, which revealed pulses in each group, and the processing with different dispersion measures. As should be the case for a pulsar, the dispersion dependence of the pulse width has a minimum and the signal-to-noise ratio has a maximum when processing the observations with a nominal dispersion measure DM = 56.7 pc cm^{-3}. Giant pulses were observed both in the main pulse and in the interpulse.

At 406 MHz, measurements were made with the cross radio telescope at the Medicina Observatory (Instituto di Radioastronomia, Italy). We used a digital spectral analyzer, which provided a predetector dispersion compensation in real time (Skulachev *et al.* 2000).

At 594, 1430, and 2228 MHz, measurements were carried out with the 64-m radio telescope at the Kalyazin Radio Astronomy Observatory (Astrospace Center, Lebedev Physical Institute, Russian Academy of Sciences). We used a S2 data acquisition system designed for VLBI observations (Cannon *et al.* 1997). The system continuously recorded the data on a video cassette in a 16 MHz frequency band with two-bit digitization. The data were processed after the observations by the predetector dispersion compensation method (Popov *et al.* 2001).

The observing conditions are summarized in Table 1, where ν is the observing frequency, $\Delta\nu$ is the receiver bandwidth, N is the number of frequency channels, $\delta\nu$ is the bandwidth of a single channel, Δt_{DM} is the dispersion broadening, Res is the sampling interval, and τ is the time constant of the postdetector filter. The instrumental broadening is smaller than the scattering broadening.

Samples of the observed giant pulses are shown in Fig. 1.

Table 1. Observing conditions

ν, MHz	Dates of observations	$\Delta\nu$, MHz	N	$\delta\nu$, kHz	Δt_{DM}	Res	τ
					ms		
40	May 24–25, 2001, Sep. 13, 2001	2.56	128	20	150	25.6	30
60	July 4–16, 2001	2.56	128	20	44	25.6	30
111	May 9–12, 2001	2.56	128	20	6.7	2.56	3.0
111	Sep. 8–26, 2001	0.16	128	1.25	0.4	1.126	1.0
406	May 6–22, 2000	2.0	–	–	–	0.00025	–
594	May 19–20, 2000	16	–	–	–	0.000312	–
1430	Oct. 11–12, 2000	16	–	–	–	0.000312	–
2228	May 19–20, 2000	16	–	–	–	0.000031	–

DATA PROCESSING

We determined the scattering pulse broadening by two methods:

(1) By modeling the pulsar pulse scattering. To this end, we convolved the template representing the initial pulsar pulse with a truncated exponent,

$$G(t) = \begin{cases} \exp(-t/\tau_{sc}) & \text{for} \quad t \geq 0 \\ 0 & \text{for} \quad t < 0, \end{cases}$$

which represents the scattering by a thin screen. The observed pulsar pulse was fitted (by least squares) with the derived model-scattered pulse. As the template, we used a Gaussian pulse. The scattering broadening τ_{sc}, the template pulse width, and the time delay of the scattered pulse were the sought-for parameters. When modeling the scattered pulse at 40 and 60 MHz, we also took into account the dispersion broadening and the broadening by the time constant of the receiver postdetector filter. Figure 2 shows an example of the processing.

(2) By (least-squares) fitting the trailing edge of the observed pulse with the exponent $\exp(-t/\tau_{sc})$. Examples of this fitting are indicated by dashed curves in Fig. 1.

The two methods yielded equal (within the error limits) values of τ_{sc}.

RESULTS

The results of our measurements are given in Table 2, where ν is the frequency, N is the number of giant pulses used, τ_{sc} is the measured scattering pulse broadening, and $\delta\tau_{sc}$ is the measurement error of τ_{sc}.

At 1430 and 2228 MHz, the observed giant pulses have a very short duration close to the microstructure. As was theoretically shown by Shishov (1980) and experimentally found by Hamilton *et al.* (1991), interstellar scattering does not broaden a short-duration pulsar pulse but manifests itself only as an indistinct train of pulses with the envelope that represents the scattering. In this case, the measured scattering may be underestimated. At the same time, pulse trains rather than single pulses are more commonly observed at these frequencies; as a result,

Table 2. Results of our measurements

ν, MHz	N	τ_{sc}	$\delta\tau_{sc}$
		ms	
40	4	600	250
60	5	140	70
111	65	16	5
406	25	0.18	0.08
594	15	0.018	0.008
1430	8	0.003	0.002
2228	5	0.00006	0.00004

Table 3. Published data

ν, MHz	τ_{sc}, ms	References
102	29	Kuzmin *et al.* (1996)
115	13	Staelin and Sutton (1970)
157	3.8	Staelin and Sutton (1970)
196	2.0	Kuzmin* (1994)
600	0.095	Sallmen *et al.* (1999)
1400	0.0025	Sallmen *et al.* (1999)

*At 196 MHz, τ_{sc} was measured by Kuzmin (1994) from the integrated profile of Rankin *et al.* (1970).

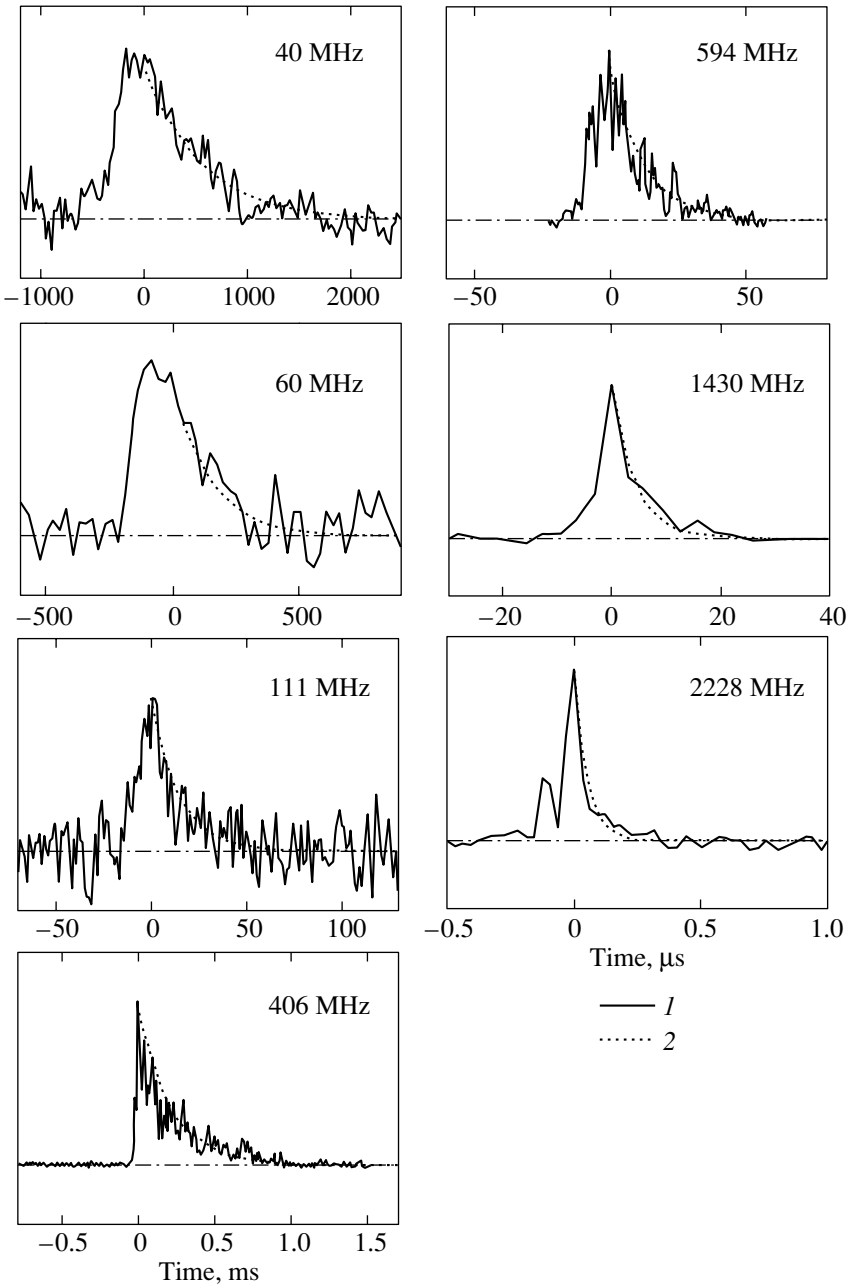

Fig. 1. (*1*)Examples of the observed giant pulses; (*2*) an exponential fit $\exp(-t/\tau_{sc})$ to the pulse trailing edge.

the measured scattering may be overestimated. More accurate measurements are required.

The frequency dependence of the scattering pulse broadening constructed from the data of Table 2 is shown in Fig. 3. The least-squares fitting yields the frequency dependence

$$\tau_{sc} = 22 \times (\nu/100)^{-3.8\pm0.2},$$

where τ_{sc} is in milliseconds and ν is in MHz.

Figure 3 also shows τ_{sc} from the published data listed in Table 3.

DISCUSSION

The frequency dependence of the scattering pulse broadening for the pulsar PSR B0531+21 that we measured with a higher accuracy than in previous studies suggests a Gaussian distribution of interstellar inhomogeneities with $\gamma = -4$. It falls outside the error limits of correspondence to a Kolmogorov model spectrum of inhomogeneities ($\gamma = -4.4$).

This conclusion is opposite to the conclusion by Cordes *et al.* (1985) that the frequency dependence disagrees with a Gaussian spectrum and agrees with

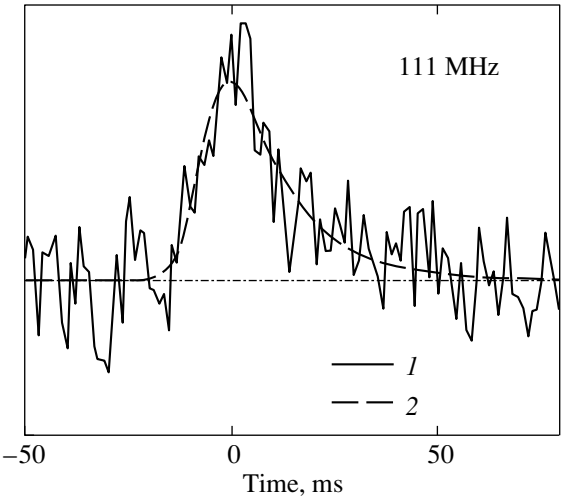

Fig. 2. An example of the processing of the observed pulse (*1*) by fitting a model-scattered template pulse (*2*).

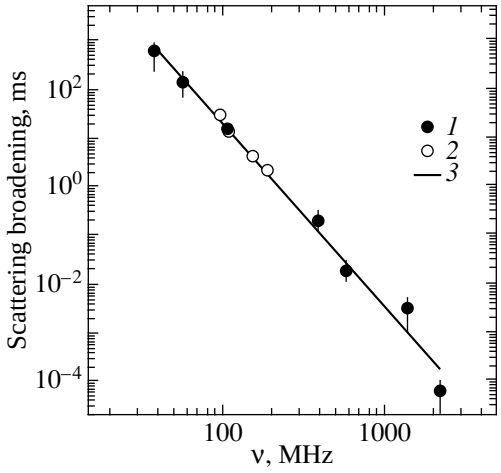

Fig. 3. Frequency dependence of the scattering pulse broadening: (*1*) our measurements, (*2*) published data, (*3*) a power-law fit to the frequency dependence $\tau_{sc} = 22 \times (\nu/100)^{-3.8\pm0.2}$.

a Kolmogorov spectrum of inhomogeneities. However, it should be noted that the mean $\gamma = -4.45 \pm 0.3$ given by Cordes *et al.* (1985) was obtained with no allowance for the weights of the measurements for individual pulsars that they carried out with greatly differing (up to an order of magnitude) accuracies. The most accurate data were obtained for the pulsar PSR B0833−45, for which $\gamma = -4.1 \pm 0.07$. For all the five pulsars investigated by Cordes *et al.* (1985), the weighted mean is $\gamma = -4.16 \pm 0.15$, which is in agreement with our measurements and better corresponds to a Gaussian distribution of inhomogeneities.

The reduction of our measurements to a frequency of 1 GHz yields $\log \tau_{sc}^{1GHz}[s] = -5.45$, twice the cataloged value $\log \tau_{sc}^{1GHz}[s] = -5.82$ (Taylor *et al.* 1995), which must be corrected.

CONCLUSIONS

(1) Based on direct measurements of giant pulses from the pulsar PSR B0531+21 in the Crab Nebula, we have measured the frequency dependence of the pulsar pulse broadening by scattering in the widest frequency range, from 40 to 2228 MHz.

(2) The measured frequency dependence of the scattering pulse broadening $\tau_{sc} \propto \nu^{-3.8\pm0.2}$ suggests a Gaussian distribution of interstellar inhomogeneities toward the Crab pulsar and falls outside the error limits of correspondence to a Kolmogorov model spectrum of inhomogeneities.

(3) The data on the pulse broadening by interstellar scattering in the catalog by Taylor *et al.* (1995) need to be corrected.

Further studies are required to analyze the pulse shape and to determine whether the scattering corresponds to a thin screen or to an extended interstellar medium. Long-term observations are also desirable for an analysis of the scattering variability.

ACKNOWLEDGMENTS

We wish to thank V.V. Ivanova, K.A. Lapaev, A.S. Aleksandrov, A.D. Skulachev, V.V. Oreshko, A. Maccaferri, A. Cattani for help with the observations and data processing and V.I. Shishov for fruitful discussions. We are grateful to Yu.P. Ilyasov for the opportunity to use the receiving–recording system of the Kalyazin Radio Astronomy Observatory. This work was supported in part by the Russian Foundation for Basic Research (project no. 01-02-16326).

REFERENCES

1. W. H. Cannon, D. Baer, Q. Feil, *et al.*, Vistas Astron. **41**, 297 (1997).
2. J. M. Cordes, J. M. Weisberg, and V. Boriakoff, Astrophys. J. **288**, 221 (1985).
3. P. A. Hamilton, P. M. McCulloch, A. D. Kuzmin, *et al.*, in *Galactic and Extragalactic Radio-Astronomy: Proceedings of the XVIII All-Union Radio-Astronomical Conference, Ashkhabad, 1991,* p. 184.
4. M. M. Komesaroff, P. A. Hamilton, and J. G. Ables, Aust. J. Phys. **25**, 759 (1972).
5. A. D. Kuzmin, unpublished work (1994).
6. A. Kuzmin, Astrophys. Space Sci. **278**, 53 (2001).
7. A. D. Kuzmin and B. Ya. Losovsky, Astron. Astrophys. Trans. **18**, 179 (1999).
8. A. D. Kuzmin and B. Ya. Losovskiĭ, Pis'ma Astron. Zh. **28**, 25 (2002) [Astron. Lett. **28**, 21 (2002)].

9. A. D. Kuz'min, V. A. Izvekova, V. M. Malofeev, and Yu. P. Shitov, Pis'ma Astron. Zh. **14**, 140 (1988) [Sov. Astron. Lett. **14**, 58 (1988)].
10. A. D. Kuzmin, B. Ya. Losovsky, and D. Yu. Sitnikov, Pis'ma Astron. Zh. **22**, 359 (1996) [Astron. Lett. **22**, 321 (1996)].
11. L. I. Matveyenko and N. A. Lotova, Astron. Zh. **47**, 483 (1970) [Sov. Astron. **14**, 388 (1970)].
12. M. V. Popov, N. Bartel, W. H. Cannon, *et al.*, Astron. Astrophys. (2001) (in press).
13. J. M. Rankin, J. M. Comella, H. D. Craft, *et al.*, Astrophys. J. **162**, 702 (1970).
14. S. Sallmen, D. C. Backer, T. H. Hankins, and D. Lundgren, Astrophys. J. **517**, 460 (1999).
15. V. I. Shishov, Astron. Zh. **57**, 321 (1980) [Sov. Astron. **24**, 187 (1980)].
16. A. D. Skulachev, V. A. Soglasnov, N. D'Amico, *et al.*, Tr. Fiz. Inst. Akad. Nauk **225**, 105 (2000).
17. D. H. Staelin and J. M. Sutton, Nature **226**, 69 (1970).
18. J. H. Taylor, R. N. Manchester, A. G. Lyne, and F. Camilo, unpublished work (1995).
19. I. P. Williamson, Mon. Not. R. Astron. Soc. **166**, 499 (1974).

Translated by G. Rudnitskii

Astronomy Letters, Vol. 28, No. 4, 2002, pp. 257–260. Translated from Pis'ma v Astronomicheskiĭ Zhurnal, Vol. 28, No. 4, 2002, pp. 298–301.

Photometric Variability of the Protoplanetary Nebula LSIV−12°111

V. P. Arkhipova*, N. P. Ikonnikova, R. I. Noskova, and G. V. Komissarova

Sternberg Astronomical Institute, Universitetskii pr. 13, Moscow, 119899 Russia

Received November 30, 2001

Abstract—We present our photometric observations of an early B supergiant with an infrared excess, the protoplanetary object LSIV−12°111, and the previously suspected variable star NSV 24971. We confirm its photometric variability. During two observing seasons (2000–2001), the star exhibited rapid irregular light variations with amplitudes $\Delta V \sim 0\overset{m}{.}3$, $\Delta B \sim 0\overset{m}{.}3$, and $\Delta U \sim 0\overset{m}{.}4$ and a time scale of $\sim 1^{\rm d}$. There is no correlation between the colors and magnitudes of the star. The variability patterns of LSIV−12°111 and two other hot post-AGB stars, V886 Her and V1853 Cyg, are shown to be similar.

Key words: *protoplanetary objects, photometric observations, evolutionary status*

INTRODUCTION

LSIV−12°111 = BD−13°5550 = IRAS 19590−1249 = NSV 24971 is a high-latitude ($b = -21\overset{\circ}{.}3$) B0 supergiant with emission lines in its spectrum that exhibits a large far-infrared excess. The star is presumed to be an intermediate-mass protoplanetary object (Conlon *et al.* 1993). In the course of its evolution, the red giant lost most of its mass at the end of the AGB; subsequently, its core contracted and heated up at constant bolometric luminosity. As a result, the star moved horizontally across the Hertzsprung–Russell diagram to the left into the region of increasingly hot stars. Currently, we observe the star with a temperature $T_{\rm eff} \sim 24\,000$ K (McCausland *et al.* 1992) that has already begun to ionize its surrounding envelope. Thus, the star's spectrum is represented by two components: the absorption spectrum of a B0 supergiant and the emission spectrum of a gaseous envelope superimposed on it. Conlon *et al.* (1993) detected strong emission features in the Balmer lines; the spectrum also exhibits [Fe II], [N II], and [S II] emission lines. Cold dust with $T_{\rm dust} \sim 120$ K is responsible for the far-infrared radiation (Conlon *et al.* 1993). McCausland *et al.* (1992) determined the abundances of a number of chemical elements in the stellar atmosphere and found an underabundance of carbon and iron, which was also noted in other post-AGB supergiants. In addition, having compared the star's parameters with theoretical post-AGB evolutionary tracks, they estimated the mass of LSIV−12°111 to be $M = 0.67 M_\odot$. This gives hope that its evolutionary manifestations will be found over a period of ∼100 yr.

*E-mail: vera@sai.msu.ru

UBV OBSERVATIONS

Kilkenny and Pauls (1990) detected a change in the brightness of LSIV−12°111 by $0\overset{m}{.}13$ in the V band on two consecutive nights. For this reason, the star was included in the catalog of suspected variables (Kazarovets *et al.* 1998), where it was designated NSV 24971.

During the two observing seasons in 2000–2001, we obtained 43 magnitude estimates for the star. Our measurements were carried out with a UBV photometer attached to the 60-cm Zeiss telescope at the Crimean Station of the Sternberg Astronomical Institute. The comparison star was HD 189558 [$V = 7\overset{m}{.}72$, $B-V = +0.52$, $U-B = -0.02$ (Roman 1955)]. Our UBV observations are listed in the table, and the star's UBV light curves are shown in Fig. 1. LSIV−12°111 exhibited rapid erratic light variations with amplitudes $\Delta V \sim 0\overset{m}{.}3$, $\Delta B \sim 0\overset{m}{.}3$, and $\Delta U \sim 0\overset{m}{.}4$ and a time scale of $\sim 1^{\rm d}$. There is no correlation between its colors and magnitudes (Fig. 2).

The other two hot post-AGB objects, V886 Her and V1853 Cyg, show a similar photometric behavior (Arkhipova *et al.* 1996, 2001). We suggested that the photometric variability of V886 Her and V1853 Cyg could be caused both by a variable stellar wind and by low-amplitude rapid pulsations. However, whereas there is evidence of mass outflow for the latter two stars (variable P Cyg profiles of the H I and He I lines, the existence of shifted C IV and Si IV absorption lines in the ultraviolet spectra of the stars), observations of the C IV and Si IV resonance lines in the low-resolution IUE spectrum of LSIV−12°111 (Conlon *et al.* 1993) show no evidence of mass loss.

1063-7737/02/2804-0257$22.00

UBV observations of LSIV−12°111 in 2000–2001

JD 2 400 000+	U	B	V	$U-B$	$B-V$
51753.448	10.625	11.392	11.261	−0.767	0.131
51755.378	10.708	11.411	11.332	−0.703	0.079
51759.378	10.771	11.504	11.408	−0.733	0.096
51765.347	10.659	11.365	11.274	−0.706	0.091
51766.372	10.939	11.620	11.446	−0.681	0.174
51767.387	10.769	11.516	11.380	−0.747	0.136
51768.361	10.569	11.325	11.242	−0.756	0.083
51776.361	10.729	11.439	11.308	−0.710	0.131
51777.361	10.752	11.412	11.318	−0.660	0.094
51778.346	10.725	11.432	11.325	−0.707	0.107
51780.406	10.844	11.500	11.399	−0.656	0.101
51781.382	10.868	11.544	11.454	−0.676	0.090
51782.292	10.885	11.554	11.462	−0.669	0.092
51817.231	10.557	11.251	11.155	−0.694	0.096
51819.217	10.811	11.394	11.307	−0.583	0.087
51821.214	10.644	11.321	11.237	−0.677	0.084
51823.265	10.868	11.453	11.313	−0.585	0.140
51841.179	10.646	11.344	11.261	−0.698	0.083
51844.186	10.760	11.464	11.384	−0.760	0.080
52047.524	10.858	11.533	11.460	−0.675	0.073
52057.494	10.615	11.335	11.244	−0.720	0.091
52071.487	10.870	11.511	11.421	−0.641	0.090
52072.483	10.886	11.485	11.397	−0.599	0.088
52079.491	10.784	11.408	11.328	−0.624	0.080
52086.452	10.612	11.376	11.256	−0.764	0.120
52092.452	10.898	11.554	11.512	−0.656	0.042
52093.460	10.777	11.490	11.402	−0.713	0.088
52100.456	10.659	11.380	11.255	−0.721	0.125
52101.451	10.542	11.270	11.195	−0.728	0.075
52104.464	10.642	11.358	11.273	−0.716	0.085
52106.453	10.684	11.387	11.257	−0.703	0.130
52107.475	10.740	11.440	11.325	−0.700	0.115
52112.432	10.664	11.413	11.330	−0.749	0.083
52113.420	10.770	11.453	11.364	−0.683	0.089
52131.376	10.748	11.446	11.356	−0.698	0.090
52132.424	10.709	11.430	11.349	−0.721	0.081
52141.343	10.639	11.362	11.288	−0.723	0.074
52147.332	10.817	11.530	11.471	−0.713	0.059
52167.284	10.843	11.550	11.435	−0.707	0.115
52172.302	10.751	11.452	11.353	−0.701	0.099
52191.222	10.449	11.217	11.080	−0.768	0.137
52196.208	10.773	11.478	11.403	−0.705	0.075
52208.195	10.718	11.419	11.347	−0.701	0.072

THE PHOTOMETRIC AND SPECTROSCOPIC HISTORY OF LSIV−12°111

The star LSIV−12°111 = BD−13°5550 has a visual magnitude of $9\overset{m}{.}7$ in the BD catalog. Its current mean magnitude is $\langle V\rangle = 11\overset{m}{.}31$. Has the star actually faded? Using the SIMBAD database, we drew a sample of 40 stars from a $1^\circ \times 1^\circ$ field around LSIV−12°111, which are contained in the BD and Tycho catalogs. The V_T magnitudes of the Tycho catalog are known to be close to Johnson's V magnitudes. LSIV−12°111 has $V_T = 11\overset{m}{.}453 \pm 0\overset{m}{.}137$. Figure 3 shows the relationship between BD and V_T magnitudes. In this figure, LSIV−12°111 is marked by an open circle. We see that for stars fainter than $V_T = 10^m$, the BD magnitudes are systematically brighter by 1^m or more. Therefore, LSIV−12°111 cannot be said to have faded since the BD epoch. The star's mean magnitudes, as derived from our 2000–2001 observations ($\langle V\rangle = 11\overset{m}{.}32$, $\langle B\rangle = 11\overset{m}{.}41$, $\langle U\rangle = 10\overset{m}{.}75$), have been virtually constant since the epoch of the first photoelectric *UBV* estimates obtained by Drilling (1975) in 1973 ($V = 11\overset{m}{.}33$, $B = 11\overset{m}{.}43$, $U = 10\overset{m}{.}62$).

The spectral type of LSIV−12°111 was first determined at the epoch of the Catalog of Luminous Stars (Nassau and Stephenson 1963). In this catalog, the star's spectral type is OB^+h (an O star with Hα emission). Based on low-resolution spectra, Kilkenny and Pauls (1990) estimated the spectral type of LSIV−12°111 to be B0. An analysis of the star's echelle spectrum by McCausland *et al.* (1992) yielded an effective temperature $T_{\rm eff} = 23\,750 \pm 1000$ K, which corresponds to a normal color index of $(B-V)_0 = -0.21 \ldots -0.23$ (Flower 1996) and to the spectral type B0–B0.5 on the supergiant scale by Straizys (1977). In contrast to the other hot post-AGB star V886 Her, which exhibited a fading and a rapid change of its spectral type in a century (Arkhipova *et al.* 1996, 2001), LSIV−12°111 has been an early B supergiant with emission lines in its spectrum at least for the last 40 years. Thus, we may assume that LSIV−12°111 is not a massive ($M \geq 0.7M_\odot$) progenitor of the planetary nebula. In this sense, the star more closely resembles V1853 Cyg = LSII+34°26, which has showed no brightness trend and no temperature variations over the last 30 years (Arkhipova *et al.* 2001). The mass of the star from McCausland *et al.* (1992) may be slightly overestimated.

EXTINCTION

Conlon *et al.* (1993) estimated the color excess for LSIV−12°111 from the relation between $E(b-v)$ and $E(B-V)$ to be $E(B-V) = 0\overset{m}{.}37$. Taking $(B-V)_0 =$

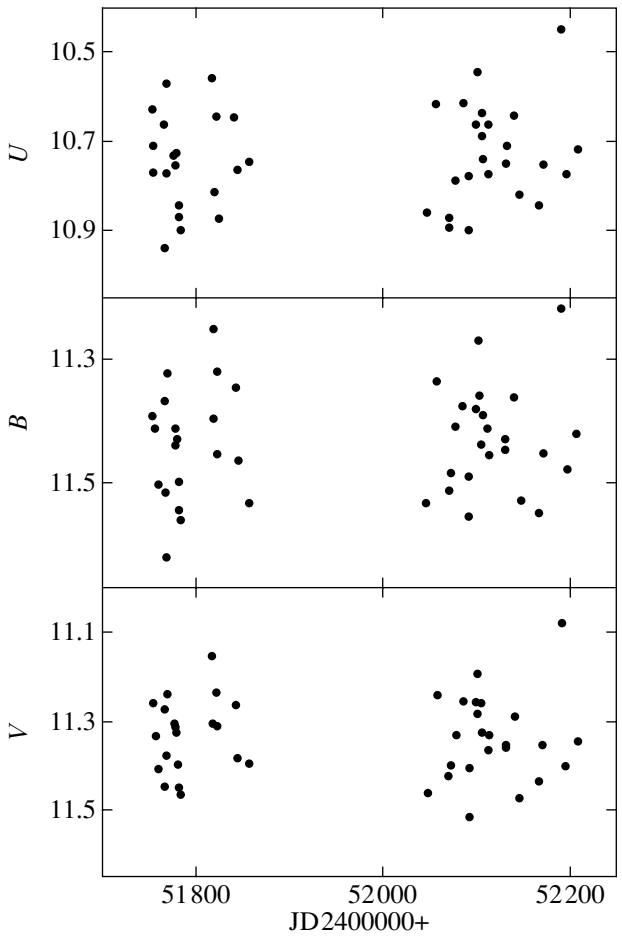

Fig. 1. The UBV light curves of LSIV−12°111 in 2000–2001.

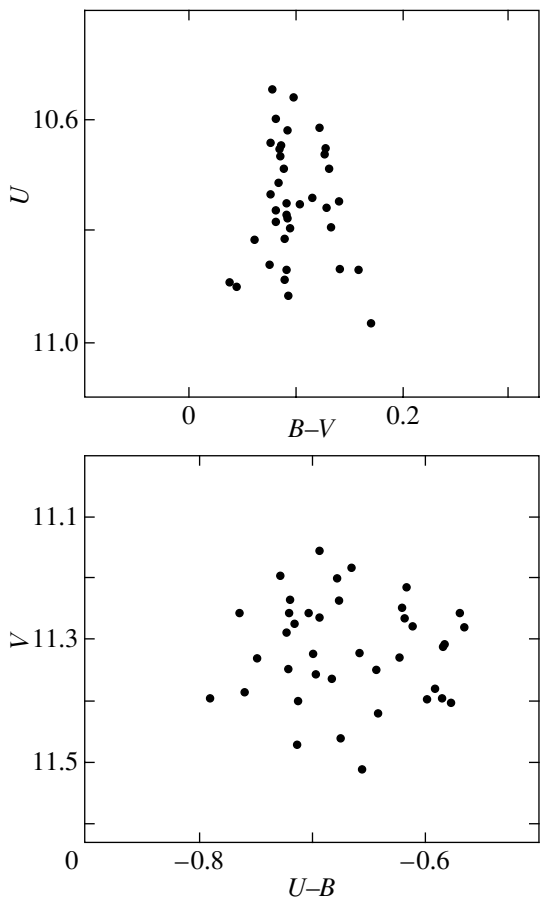

Fig. 2. Color–magnitude diagrams for LSIV−12°111.

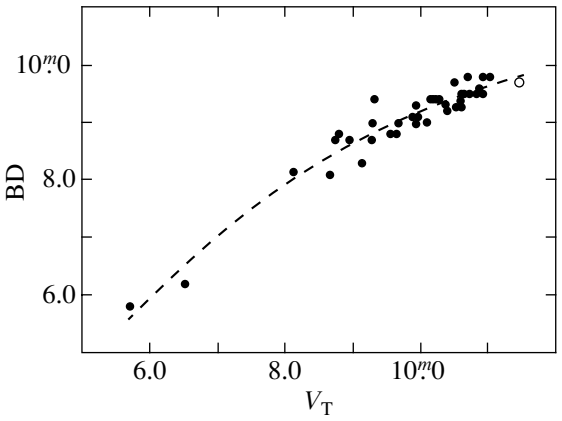

Fig. 3. The relationship between Tycho V_T and BD magnitudes for stars from a $1° \times 1°$ field around LSIV−12°111 (dots). The open circle refers to LSIV−12°111.

-0.21 for the star and using $\langle(B--V)\rangle = +0.1$, we obtained $E(B-V) = 0^m.31$. For 20 stars with a known reddening from the LSIV−12°111 field, we obtained a much smaller color excess: $\langle E(B-V)\rangle = 0^m.16$. As in many other protoplanetary objects (Arkhipova *et al.* 2000, 2001), part of the color excess ($\geq 0^m.15$) for LSIV−12°111 appears to be attributable to its circumstellar dust envelope, whose extinction law may differ from the standard interstellar extinction law.

Note that the intensity of the λ2200 Å interstellar absorption band in the IUE spectra of LSIV−12°111 taken in April 1992 corresponds to a color excess $E(B-V) \sim 0.2$ (Conlon *et al.* 1993), suggesting the existence of a circumstellar dust envelope with an abnormal extinction law.

CONCLUSIONS

Our photometric observations of LSIV−12°111 in 2000–2001 have led us to conclude that its variability is similar in pattern to that of two other hot post-AGB stars, V886 Her and V1853 Cyg. Therefore, its variability seems to be attributable to its evolutionary status. The mean brightness of the star appears to have not changed since the epoch of the BD catalog: the star exhibited no rapid evolutionary changes. To establish the cause of the variability of

LSIV−12°111 requires further photometric observations of the star — its monitoring on short time scales ($<1^d$) and high-resolution spectroscopic observations of LSIV−12°111 to detect a possible variability of the line profiles, as is the case for the related objects V886 Her and V1853 Cyg. Systematic measurements of the star's radial velocities aimed at revealing their possible variability are also needed.

ACKNOWLEDGMENTS

We are grateful to the Russian Foundation for Basic Research for financial support (project no. 01-02-16530).

REFERENCES

1. V. P. Arkhipova, N. P. Ikonnikova, V. F. Esipov, and R. I. Noskova, Pis'ma Astron. Zh. **22**, 526 (1996) [Astron. Lett. **22**, 470 (1996)].
2. V. P. Arkhipova, N. P. Ikonnikova, R. I. Noskova, and G. V. Sokol, Pis'ma Astron. Zh. **26**, 705 (2000) [Astron. Lett. **26**, 609 (2000)].
3. V. P. Arkhipova, N. P. Ikonnikova, R. I. Noskova, *et al.*, Pis'ma Astron. Zh. **27**, 841 (2001) [Astron. Lett. **27**, 719 (2001)].
4. E. S. Conlon, P. L. Dufton, R. J. H. McCausland, and F. P. Keenan, Astrophys. J. **408**, 593 (1993).
5. J. S. Drilling, Astron. J. **80**, 128 (1975).
6. P. J. Flower, Astrophys. J. **469**, 355 (1996).
7. E. V. Kazarovets, N. N. Samus, and O. V. Durlevich, Inf. Bull. Var. Stars, No. 4655 (1998).
8. D. Kilkenny and L. Pauls, Mon. Not. R. Astron. Soc. **244**, 133 (1990).
9. R. J. H. McCausland, E. S. Conlon, P. L. Dufton, and F. P. Keenan, Astrophys. J. **394**, 298 (1992).
10. J. J. Nassau and C. B. Stephenson, Luminous stars in the Northern Milky Way, IV, Hamburger Sternw., Warner and Swasey Observ. (1963).
11. N. G. Roman, Astrophys. J., Suppl. Ser. **2**, 195 (1955).
12. V. Straizys, *Multicolor Stellar Photometry* (Mokslas, Vil'nyus, 1977; Pachart Publ. House, Tucson, 1992).

Translated by N. Samus'

Astronomy Letters, Vol. 28, No. 4, 2002, pp. 261–271. Translated from Pis'ma v Astronomicheskiĭ Zhurnal, Vol. 28, No. 4, 2002, pp. 302–313.

Astrometric Orbits from a Direct Combination of Ground-Based Catalogs with the Hipparcos Catalog

G. A. Goncharov and O. V. Kiyaeva*

Pulkovo Astronomical Observatory, Russian Academy of Sciences, Pulkovskoe sh. 65, St. Petersburg, Russia

Received November 16, 2001

Abstract—A direct combination of 57 ground-based astrometric observational catalogs with the Hipparcos catalog made it possible to detect and analyze nonlinear motions of the photocenters of several tens of unresolved stellar pairs during 1938–1995. We separated these motions into the barycenter proper motions and the photocenter elliptical motions around the barycenters if the semimajor axis of the apparent ellipse in the plane of the sky is $0''.08$ and the period ranges from 10 to 55 years. We consider in detail six pairs for which we determined the photocenter (astrometric) orbits and the component masses for the first time: κ For (period 26.5 yr, semimajor axis of the photocenter orbit $0''.26$), δ And (52.8 yr, $0''.30$), ξ Aqr (25.5 yr, $0''.11$), 83 Cnc (32.0 yr, $0''.19$), α UMa (44.5 yr, $0''.21$), and β LMi (38.35 yr, $0''.12$). Our method is particularly efficient for a large magnitude difference between the components, for example, when searching for white dwarfs. © *2002 MAIK "Nauka/Interperiodica"*.

Key words: *catalogs, astrometric orbits*

INTRODUCTION

We have already described the technique of direct combination of observational ground-based astrometric catalogs with the Hipparcos catalog (hereafter HIP) (ESA 1997), along with some results, in our earlier papers [Goncharov and Kornilov (1997); Goncharov *et al.* (2000, 2001)]. The essence of the method consists in reducing a large number of observational ground-based astrometric catalogs with different observational epochs to a reference frame that is close to ICRS, using the coordinates of single stars from the catalogs in question, the radial velocities of the same stars adopted from the Hipparcos Input Catalogue (HIV) (Turon *et al.* 1993), and the corresponding parallaxes and proper motions adopted from the HIP. The individual proper motions are refined using several iterations and differ from the corresponding initial values. The reference frame thus obtained is then expanded to include multiple stars as well. For each star, a series of homogeneous astrometric observations is obtained, which reflects its linear or nonlinear motion on the sky sphere with respect to the ICRS reference frame over a period of several decades. Such series (although in other reference frames) were traditionally used both to refine the proper motions of stars in FK5-type fundamental catalogs and to study the nonlinear motions of the photocenters of unresolved stellar systems – the so-called astrometric binaries [see, e.g., Gerasimovich (1936)]. In the second case the observed nonlinear motion of the photocenter of a stellar system is decomposed into the proper motion of the barycenter and the elliptic orbital motion of the photocenter relative to the barycenter.

We used astrometric observations of 1535 FK5-catalog stars from 57 ground-based observational catalogs with epochs ranging from 1939 to 1995, and data from the HIP catalog. See Goncharov *et al.* (2001) for the list of catalogs used.

The procedure of the decomposition of the observed nonlinear motion of the photocenter into linear and elliptic components included (Goncharov *et al.* 2001):

(1) The determination of an approximate ($\pm 0''.002$/yr) proper motion of the photocenter over a more than century-long time interval. In such a long time interval (several orbital periods) the mean motion of the photocenter is virtually coincident with that of the barycenter;

(2) The determination of six orbital elements (a, T, Ω, ω, e, i) after eliminating the proper motion inferred from ground-based catalogs and HIP using the method described by Kiyaeva and Kalinichenko (1998). We either adopted the orbital period from external data or determined it with a low accuracy

*E-mail: gaoran@mail.wplus.net

Table 1. Stellar systems studied

Name	HIP	FK5	HD	ADS	$Spectrum_A$	V_A	π
α CMa	32349	257	48915	5423	A0V	$-1^m.4$	$0''.379$
α CMi	37279	291	61421	6251	F5V	0.4	0.283
μ Cas	5336	1030	6582	–	G5VI	5.2	0.132
α Oph	86032	656	159561	–	A5IV	2.1	0.070
10 UMa	44248	339	76943	–	F5V	4.1	0.061
κ For	11072	83	14802	–	G2V	5.2	0.046–0.080
δ And	3092	20	3627	548	K3III	3.3	0.032
ξ Aqr	106786	1569	205767	–	A7V	4.7	0.028
83 Cnc	45699	350	80218	–	F5V	6.6	0.027
α UMa	54061	417	95689	8035	K0III	2.0	0.026
β LMi	51233	390	90537	7780	G8III–IV	4.6	0.022

(1–3 yr) from the astrometric data series considered. We adopted the well-known values for certain orbital elements in some of the cases (marked by asterisks in the tables);

(3) Refinement of the proper motion using the ground-based and HIP catalog data after eliminating the orbital motion of the photocenter inferred above;

(4) Iterative refinement of the orbital elements and of the proper motion as described in pp. (2) and (3) above.

We compiled the proper motions thus obtained for single stars and for the barycenters of stellar systems in the catalog of "Proper Motions of Fundamental Stars" (PMFS) available from the Starsbourg database as catalog I-266 (Goncharov *et al.* 2001).

The astrometric data series obtained for each of several tens of well-known and suspected binaries with periods <55 yr show elliptic orbital motion of the photocenter around the barycenter. Examples can be found in the paper of Goncharov *et al.* (2000). In this paper we analyze 11 stellar pairs, for which we determined the orbits of their photocenters (usually referred to as astrometric orbits). For five pairs the accuracy of the observations used and that of the technique employed can be assessed by comparing our results with sufficiently accurate astrometric orbits obtained by various authors. The astrometric orbits of the remaining six pairs have been determined for the first time, and 83 Cnc has been believed to be a single star.

The 56-year long time interval considered (it is shorter for some of the stars) usually covers only one to two orbital periods, whereas the observational series used are nonuniform and of nonuniform accuracy, and therefore the motion of the photocenter is decomposed into linear and nonlinear components with a certain accuracy, which depends on that of the catalogs employed. The same factors restrict the accuracy of the determination of the elements of the orbit of the photocenter. The new orbits that we computed in this work should therefore be viewed as preliminary orbits to be used for the approximate component mass estimates and when searching for unseen components. We estimated the errors of our elements, except those of the periods, by running individual simulations for each particular star. We simulated 20 model series for the time instants of real observations superimposing on each observation a random error with a standard deviation of $0''.05$, and then computed the rms errors of orbital elements over the 20 sets thus obtained.

PARAMETERS OF STAR PAIRS STUDIED

Tables 1 and 2 first list the pairs with well-known astrometric orbits (see the Sixth Catalog of Orbits of Visual Binary Stars, Hartkopf and Mason 2001), followed by those with new astrometric orbits in the decreasing order of adopted parralaxes. Table 1 gives for each pair its identifications according to various catalogs, the spectral type, magnitude (V_A) of the bright component, and the adopted parallax.

The potential of our method becomes evident from Table 2, where we compare the semimajor axis of the apparent ellipse in the sky plane ($a_{app.}$) to the full standard deviation of observations from the orbit and single-coordinate standard deviations in α and δ (all in arcsec). The references are given to the sources of the well-known orbits. The ratio of the semimajor axis of the apparent ellipse to the full standard deviation

Table 2. Parameters of the comparison of observations used in this paper with the known and new orbits. Semimajor axis of the apparent ellipse in the sky plane is denoted as $a_{\rm app.}$

Name	$a_{\rm app.}$	Deviation			S/N	Reference
		full	in α	in δ		
Well-known orbits						
α CMa	$2''.400$	$0''.201$	$0''.084$	$0''.183$	11.9	Benest and Duvent (1995)
α CMi	1.100	0.161	0.096	0.130	6.8	Girard *et al.* (2000)
μ Cas	0.190	0.076	0.057	0.048	2.5	Drummond *et al.* (1995)
α Oph	0.070	0.050	0.034	0.037	1.4	Augensen and Heintz (1992)
10 UMa	0.175	0.070	0.046	0.059	2.5	Heintz (1997)
New and refined orbits						
κ For	0.255	0.073	0.048	0.063	3.5	–
δ And	0.280	0.071	0.062	0.042	3.9	–
ξ Aqr	0.080	0.053	0.029	0.045	1.5	–
83 Cnc	0.180	0.083	0.053	0.063	2.2	–
α UMa	0.200	0.044	0.032	0.029	4.5	–
β LMi	0.110	0.058	0.050	0.035	1.9	–

can be considered to characterize the signal-to-noise ratio (S/N) of our method.

Hereafter, we analyze six pairs whose astrometric orbits we determined for the first time.

In some of the cases, we cite speckle interferometric observations, always adopted from the Fourth Catalog of Interferometric Measurements of Binary Stars (Hartkopf *et al.* 2001).

For all six pairs, we propose consistent parameter sets hereafter referred to as pair models. The data used in these models include the parallax, spectral type, color indices, and the magnitude of the bright component A adopted from the HIP and HIC catalogs and also the orbit of the photocenter with respect to the barycenter as inferred in this paper. We used the following evident relations. The elements P, T, i, e, and Ω of the orbits of the faint companions relative to the respective bright companions coincide with those of the photocenter relative to the barycenter, and the corresponding ω differ by 180°. The relation between the semimajor axes $a_{\rm BA}$ and $a_{\rm pm}$ of the visual and astrometric orbits, respectively, is determined by the component mass ratios component and magnitude differences: namely, component A, the photocenter, the barycenter, and component B are always in line and the ratios of the barycenter–A and photocenter–A separations to the B–A distance are equal to $B = M_{\rm B}/(M_{\rm A} + M_{\rm B})$, where $M_{\rm A}$ and $M_{\rm B}$ are the component masses and $\beta = 1/(1 + 10^{0.4\Delta m})$, where Δm is the component magnitude difference. It thus follows that the semimajor axis of the orbit of the photocenter is $a_{\rm pm} = a_{\rm BA} \times (B - \beta)$. We solved for each pair the set of equations: $(M_{\rm A} + M_{\rm B}) = a^3_{\rm BA}/(\pi^3 P^2)$, $a_{\rm pm} = a_{\rm BA} \times (M_{\rm B}/(M_{\rm A} + M_{\rm B}) - 1/(1 + 10^{0.4\Delta m}))$, where π and P are the parallax and the orbital period, respectively. If the faint component has been observed, i.e., $a_{\rm BA}$ is known, the mass of each component can be determined without invoking any additional assumptions (α UMa and β LMi). For pairs with unseen components the minimum mass of component B (assuming $\beta = 0$ and $\Delta m > 4^m$) and the semimajor axis of the visual orbit $a_{\rm BA}$ are determined. In these cases the mass of the unseen component is estimated to a certain accuracy from the absolute magnitude, color index, and spectral type using Hipparcos-mission results and Allen's (1977) tables. The uncertainties in the adopted values are included into the errors of the parameters determined. The errors of all model parameters are thus mutually consistent and listed in the tables. The estimated absolute magnitudes of the unseen components in δ And and 83 Cnc suggest that the stars in question are white dwarfs, and the mass of the component B is close to the white dwarf's mass maximum and therefore by fixing the mass $M_{\rm B}$ ($1.3\,M_\odot$) we refine the mass $M_{\rm A}$.

Stellar masses listed in the tables are given in solar mass units and the absolute magnitudes of the components are denoted as $M_{\rm VA}$ and $M_{\rm VB}$. The nonlinear motion of the photocenters and the astrometric orbits are shown in the corresponding figures

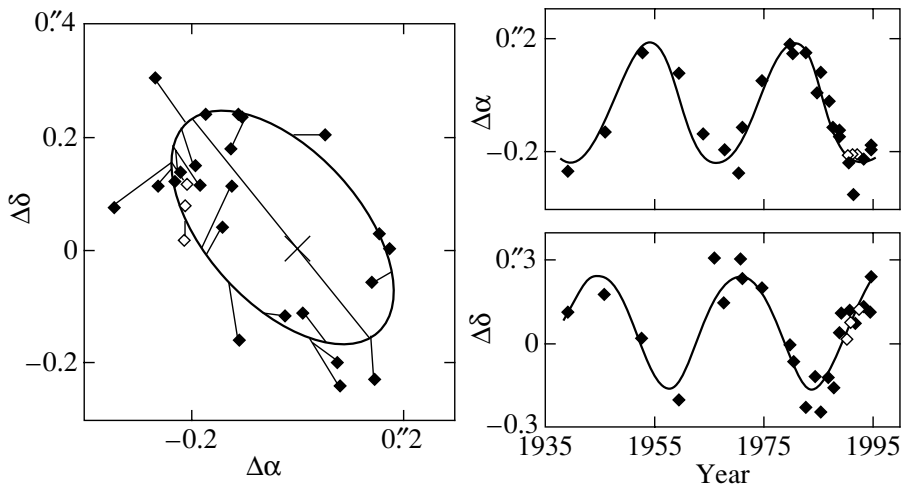

Fig. 1. Astrometric orbit of κ For. See text for the explanations to this and the following figures.

(Figs. 1–6), each of which consists of three plots: $\Delta\alpha$–$\Delta\delta$, time–$\Delta\alpha$, and time–$\Delta\delta$ ($\Delta\alpha$ and $\Delta\delta$ are in arcsec). Ground-based and HIP astrometric observations, which we used to compute our orbits, are shown as filled and open diamond signs, respectively. The observational data points are connected to the corresponding points on our computed orbits. Where space allows, the projection of the semimajor axis on the sky plane is shown.

κ For = HIP11072

Figure 1 shows the nonlinear motion of the photocenter and our computed orbit. Table 3 presents the model that we propose for this binary.

Table 3. Two models of the κ For pair with different parallaxes

Parameter	Model I	Model II
$a_{\rm BA}$	$0\overset{''}{.}54 \pm 0\overset{''}{.}02$	$0\overset{''}{.}85 \pm 0\overset{''}{.}10$
ΣM, $M_\odot$	2.3 ± 0.1	1.7 ± 0.1
$M_{\rm A}$, $M_\odot$	1.2	1.2
$M_{\rm B}$, $M_\odot$	1.1 ± 0.1	0.5 ± 0.1
B	0.48 ± 0.05	0.29 ± 0.05
β	0	0
Parallax	$0\overset{''}{.}046 \pm 0\overset{''}{.}001$	$0\overset{''}{.}08 \pm 0\overset{''}{.}01$
Spectral type$_{\rm A}$	G2V ?	G2V
Spectral type$_{\rm B}$	White dwarf	About K8V
$M_{V\rm A}$	$3\overset{m}{.}5$	$4\overset{m}{.}7$
$M_{V\rm B}$	$> 7\overset{m}{.}5$	$\approx 8\overset{m}{.}5$

Astrometric orbit of κ For:

$a_{\rm pm}$	$0\overset{''}{.}26 \pm 0\overset{''}{.}01$
P	$26\overset{\rm d}{.}5 \pm 2$
T	1983.6 ± 2.3
Ω	$133° \pm 6°$
ω	$22° \pm 31°$
e	0.2 ± 0.1
i	$56° \pm 4°$

The faint component of this pair has never been observed. Hipparcos observations showed appreciable motion of the photocenter (three open diamond signs in Fig. 1), which agree well with our computed orbit.

The parallax given in HIP ($0\overset{''}{.}046 \pm 0\overset{''}{.}001$) agrees neither with the ground-based trigonometric parallax ($0\overset{''}{.}08 \pm 0\overset{''}{.}01$) from the catalog of van Altena *et al.* (1995), nor with the photometric parallax ($0\overset{''}{.}08 \pm 0\overset{''}{.}01$) from the Third Catalog of Nearby Stars by Glise and Jareiss (1991). We had to propose two significantly different models for this binary, which we present in Table 3: a model with a white dwarf with the parallax adopted from HIP and a model with a red dwarf with a parallax of $0\overset{''}{.}08$. Given the parameters of the bright components, we can adopt $M_{\rm A} = 1.2$. Table 3 gives the mean values and the possible scatter for the sought-for quantities $M_{\rm B}$, $a_{\rm BA}$, as well as the dependent quantities $\sum M$ and B. Here we take into account the errors in $a_{\rm pm}$ and P and the quoted formal errors of the parralax.

For this binary we have for the first time deter-

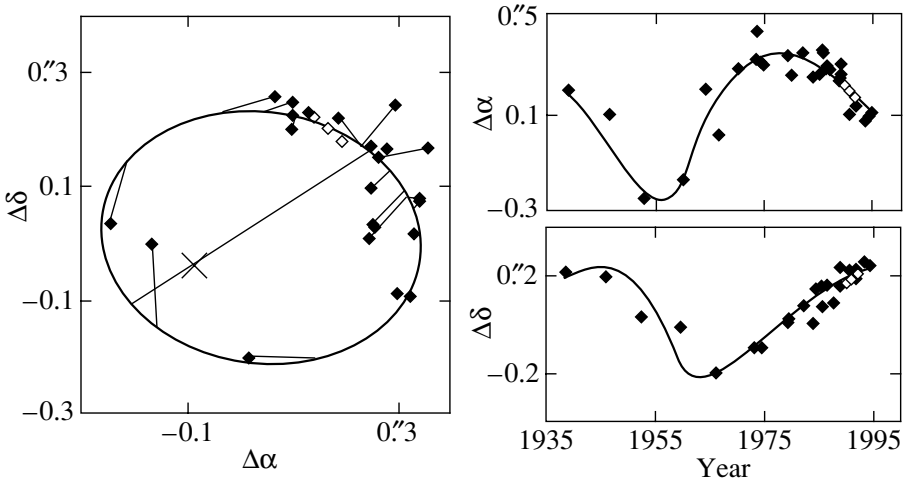

Fig. 2. Astrometric orbit of δ And.

mined the orbit of the photocenter, the semimajor axis of the relative orbit B–A, and the component masses.

δ And = HIP3092

The nonlinear motion of the photocenter and our computed orbit are shown in Fig. 2. Table 4 presents our proposed model for this binary and the model adopted from MSC.

Astrometric orbit of δ And:

$a_{\rm pm}$	$0\overset{''}{.}32 \pm 0\overset{''}{.}03$
P	$52\overset{\rm d}{.}84^*$
T	1958.5 ± 1.1
Ω	$290° \pm 7°$
ω	$51° \pm 9°$
e	0.5 ± 0.1
i	$137° \pm 5°$

The faint component in this binary has never been observed. According to Hipparcos observations, the photocenter moved linearly—see three open diamond signs in Fig. 2. Numerous speckle interferometric observations made from 1976 through 1992 failed to reveal the faint component, apparently, owing to the large component magnitude difference. The star is a single-line spectral binary. Spectroscopic observations of Griffin (2001) yielded an orbital period of 52.84 yr [instead of the 55.19 yr given by Tokovinin (1997) in his MSC catalog] and a rather large half-amplitude of radial-velocity variations (4 km/s) of the photocenter (component A) relative to the barycenter. This fact, combined with evidently nonextreme eccentricity (<0.6) and orbital inclination, can be reconciled only with a sufficiently large offset of the photocenter relative to the barycenter (6–12 AU). Given reasonable parallax values (we adopted a parallax of $0\overset{''}{.}032$ from HIP), this distance corresponds to $0\overset{''}{.}2$–$0\overset{''}{.}4$ and is consistent with our computed $a_{\rm pm}$.

The small number of astrometric observations in the vicinity of the periastron prevents accurate determination of the orbital eccentricity, and we chose the value that yields the photocenter orbit that is most consistent with the results of spectroscopic radial-velocity observations.

In the incomplete binary model proposed by Tokovinin (1997) in his MSC catalog and in our

Table 4. Model of the δ And pair from MSC and our proposed model

Parameter	MSC	Our model
$a_{\rm BA}$	$0.83''$	$0.62'' \pm 0.04''$
$a_{\rm pm}$	$>0.03''$	$0.32'' \pm 0.03''$
P	55.19	52.84
ΣM	>4.8	2.6 ± 0.4
$M_{\rm A}$	4.6	1.3 ± 0.4
$M_{\rm B}$	>0.2	1.3
B	>0.04	0.5 ± 0.1
β	0	0
Parallax	$0.034''$	$0.032'' \pm 0.001''$
Spectral type$_{\rm A}$	K3III	K3III
Spectral type$_{\rm B}$	–	White dwarf
$M_{V\rm A}$	–	0.9^m
$M_{V\rm B}$	–	$>5^m$

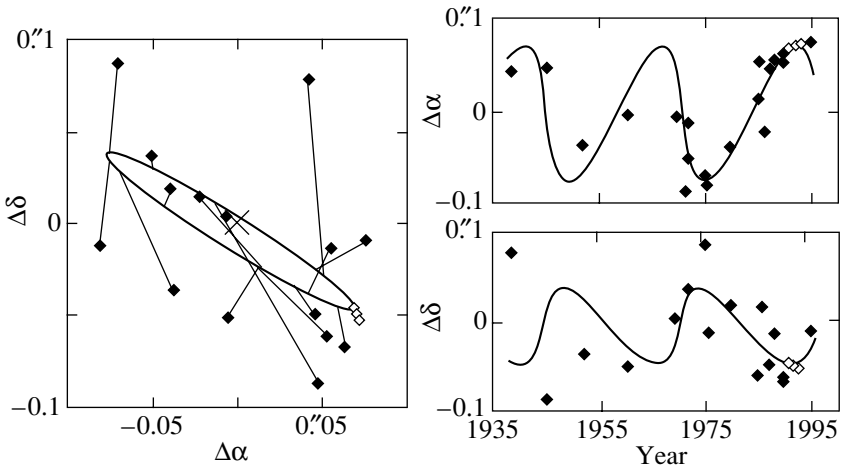

Fig. 3. Astrometric orbit of ξ Aqr.

model presented in Table 4, $a_{\rm pm}$ was not determined from observations.

Because of the rather large $a_{\rm pm}$, a plausible mass for the bright giant-star component ($M_{\rm A} = 1.3\ M_\odot$) can be obtained only for the extreme mass of the faint component, i.e., for this pair the unknown quantities are $M_{\rm A}$ and $a_{\rm BA}$. Their errors are determined mainly by the uncertainty in $a_{\rm pm}$.

The pair considered is surrounded by a dust disk, which was discussed by Judge *et al.* (1987). It extends approximately from the faint component just mentioned to a third component located at a distance of ∼900 AU, thereby making possible mass and energy transfer in the system considered, which can show up in a formal violation of Kepler's law. Judge *et al.* (1987) advance arguments in support of the white-dwarf nature of the faint component. However, according to Plets *et al.* (1997), the combined spectrum exhibits a red excess. The situation is further complicated by the bright component's high metallicity [(Fe/H) = +0.16 (Taylor 1999)].

This system allows various models including: (1) an evolved system consisting of a low-mass giant that has lost most of its mass to produce the dust disk, and a white dwarf with a mass close to the limit; (2) a stellar-planetary system in the state of formation with an age of $\ll 1$ Gyr and a massive dust component enshrouding the low-mass giant and the forming star.

We thus determined for the first time the orbit of the photocenter, estimated the component masses of components, and showed the bright component to be a low-mass giant and the unseen component to be a relatively massive object. These results, combined with the high metallicity, the presence of a dust disk, red excess in the spectrum, and a third and, possibly, a fourth, companion make the system considered an interesting object for further studies.

ξ Aqr = HIP106786

Figure 3 shows the nonlinear motion of the photocenter and our computed orbit.

Proposed model for the ξ Aqr pair:

$a_{\rm BA}$	$0.''34 \pm 0.''03$
$\Sigma M, M_\odot$	2.8 ± 0.7
$M_{\rm A}, M_\odot$	1.9
$M_{\rm B}, M_\odot$	0.9 ± 0.6
B	0.32 ± 0.2
β	0
Parallax	$0.''028 \pm 0.''01$
Spectral type$_{\rm A}$	A7V
Spectral type$_{\rm B}$	Dwarf
$M_{V\rm A}$	$1^m.9$
$M_{V\rm B}$	$>6^m$

According to Hipparcos observations, the photocenter moved linearly—see the three open diamond signs in Fig. 3. There are several speckle interferometric ofservations of this pair, however, they are uncertain—the measured separation between the components remains within measurement errors. It appears that the faint component has never been observed. We have the incomplete and inaccurate orbit computed by Abt (1965) based on spectroscopic observations, which we do not consider here. The astrometric observations we use – especially those made within the framework of the Hipparcos mission

– indicate a longer period—$\approx 25\overset{d}{.}5$ instead of the $21\overset{d}{.}95$ given by Abt.

HIP data ($B-V = +0.175$, spectral type A7V, $M_{VA} = 1.0$, and parallax $0\overset{''}{.}018$) are internally inconsistent. The HIP parallax might be wrong because of the binary nature of the star. We adopted a parallax of $0\overset{''}{.}028$, which agrees best with other parameters.

Based on the absolute magnitude, spectral type, and color index of the star, we adopted a bright-component mass of $M_A = 1.9\ M_\odot$, which implies $M_B = (0.9 \pm 0.6) M_\odot$. Hence the unseen component can be both a red or a white dwarf. The errors of a_{BA} and M_B in the proposed model of the ξ Aqr pair include the uncertainty of the orbit and the above-mentioned error of M_A but not the parallax error. If we adopt a parallax uncertainty of $\pm 0\overset{''}{.}01$, it becomes the dominating error source for the sought-for quantities.

We computed the orbit of the photocenter, the mass of the unseen component, and the semimajor axis of the B–A orbit for the pair in question for the first time, albeit with rather large errors, which are due to the small size of the apparent ellipse. The inferred quantities can be used to search for the unseen component.

83 Cnc = HIP45699

Figure 4 shows the nonlinear motion of the photocenter and our computed orbit.

Astrometric orbit of 83 Cnc

a_{pm}	$0.19'' \pm 0.02''$
P	$32^d \pm 2\overset{d}{.}5$
T	1976.0 ± 3.5
Ω	$148° \pm 5°$
ω	$351° \pm 42°$
e	0.6 ± 0.2
i	$94° \pm 6°$

According to Hipparcos observations the photocenter of this pair moved linearly—see the three open diamond signs in Fig. 4. The faint component has never been observed and the star has been considered single. Judging by its absolute magnitude, the unseen companion should be a white dwarf. If the adopted parallax is correct (as evidenced by the good agreement between the known parameters of the bright component), due to the large value of a_{pm}, a plausible mass for the bright component ($M_A > 1\ M_\odot$) can only be obtained for the limiting mass of the faint component, i.e., the unknown quantities for the pair in question are—M_A and a_{BA} for the fixed mass of $M_B = 1.3\ M_\odot$. The errors of the inferred quantities

Proposed model for the 83 Cnc pair

a_{BA}	0.35 ± 0.02
$\Sigma M, M_\odot$	2.4 ± 0.4
$M_A, M_\odot$	1.1 ± 0.4
$M_B, M_\odot$	1.3
B	0.54 ± 0.2
β	0
Parallax	$0\overset{''}{.}026 \pm 0\overset{''}{.}001$
Spectral type$_A$	F5V
Spectral type$_B$	White dwarf
M_{VA}	$3\overset{m}{.}6$
M_{VB}	$> 7\overset{m}{.}5$

are due mainly to the uncertainties in the estimated a_{pm}. The mass M_A of the visible component thus determined agrees well with the spectral type, $B-V$ (+0.49), and the absolute magnitude of the star.

We thus were the first to discover the binary nature, compute the orbit of the photocenter, and estimate the component masses and the semimajor axis of the B–A orbit.

α UMa = HIP54061

Spectroscopic, speckle interferometric, and visual observations of component B relative to component A are available, as well as two combined orbits: one computed by Heintz (1963), which was later supplemented and refined by Tokovinin (1997) in his MSC catalog (hereafter referred to as "Heintz + MSC"), and one computed by Soderhjelm (1999) reported in the Sixth Catalog of Orbits. The small inclination i and the scarcity of observations in the vicinity of the periastron make the inferred orbital elements Ω, ω, and i rather uncertain (in the Heintz + MSC orbit parameter ω is set equal to 180°, whereas the Sixth Catalog of Orbits sets i and Ω equal to 180° and 0°, respectively). Our estimates of Ω, ω, and i are virtually coincident with those of Heintz + MSC.

Figure 5 shows: *1*—our computed orbit; the orbits computed by Soderhjelm (1999) and Heintz + MSC for $a_{pm} = 0\overset{''}{.}21$—*2* and *3*, respectively; *4–6*—the barycenters; *7*—the results of speckle interferometric observations for $B - \beta = 0\overset{''}{.}35$. They agree well with our orbit. The orbital elements and other parameters of the pair are listed in Table 5. Our inferred quantities are given with standard errors and the sum of component masses is inferred from fixed values of parallax, period, and a_{BA}.

After determining a_{pm}, we computed the component masses and the related quantity B. We were not only the first to do it based on observations but our results are more accurate than those reported in

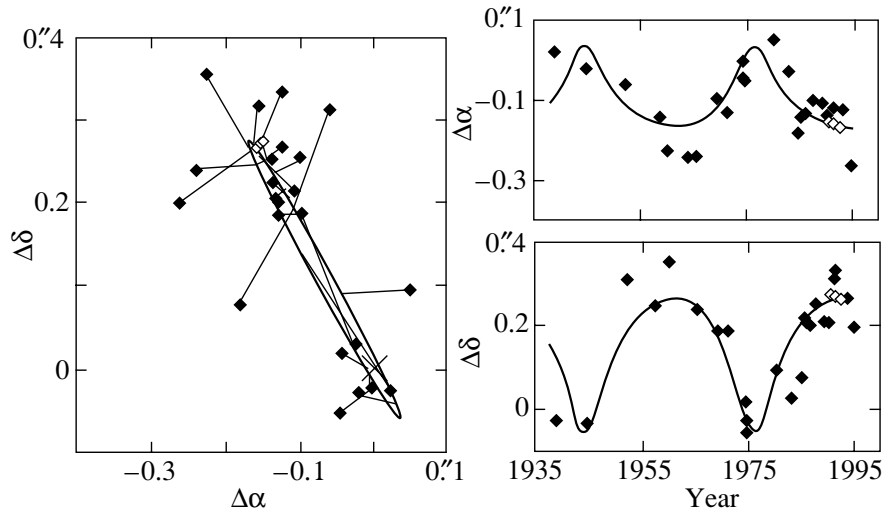

Fig. 4. Astrometric orbit of 83 Cnc.

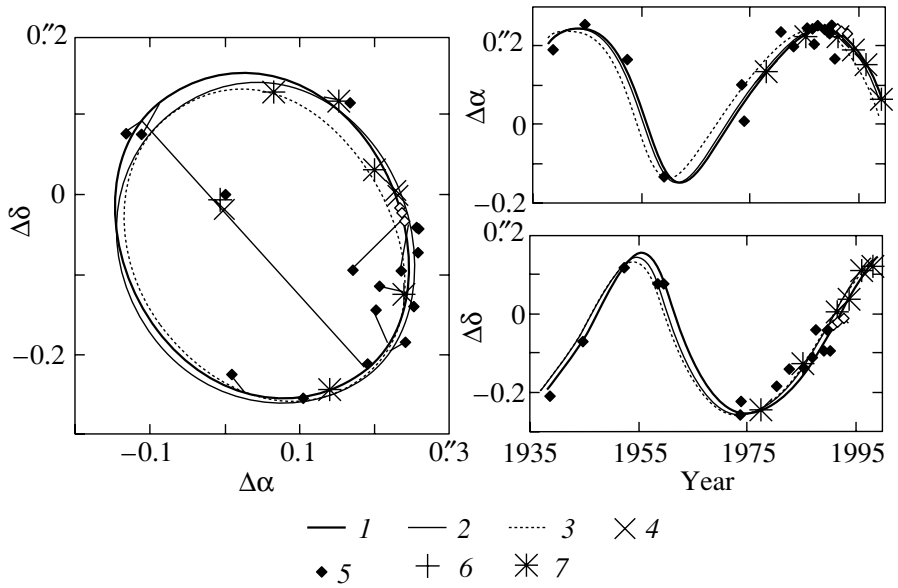

Fig. 5. Astrometric orbit of α UMa.

the Heintz + MSC model, where these corresponding quantities are inferred from the spectral type and color index. The dominating source of quoted mass errors are parallax errors. The inferred mass M_A agrees well with the quoted K0III spectral type. This discrepancy between the spectral type and absolute magnitude of component A, which is corroborated by Hipparcos observations, is possibly due to the high metallicity of the star: (Fe/H) = −0.13 according to Taylor (1999). The estimated mass M_B and absolute magnitude of the faint component leads us to conclude that its spectral type should be somewhere about A3V. According to Kondo *et al.* (1977), the classification of the faint component based on the features of the combined spectrum of the binary gives A8 V, which is consistent with our result.

As is evident from Table 6, our orbits and those computed by Soderhjelm (1999) agree equally well with the astrometric observations we used, whereas the Heintz + MSC orbit agrees with these data rather poorly (even for $a_{pm} = 0''.21$), although the only significant difference is in the time T of the periastron passage.

Thus we were the first to compute the orbit of the photocenter and estimate the component masses for this binary. A periastron passage is expected in 2002 and new observations using various methods are welcome.

Table 5. Parameters of the α UMa Pair

Parameter	Heintz + MSC	Soderhjelm (1999)	The orbit computed by the authors
a_{AB}	$0''.60$	$0''.59$	$0''.60^*$
a_{pm}	$0''.14$	–	$0''.21 \pm 0''.02$
P	$44^d.4$	$44^d.5$	$44^d.5^*$
T	1956.8	1958	1958*
Ω	$320°.3$	$0°$	$318° \pm 24°$
ω	$180°$	$222°$	$174° \pm 23°$
e	0.4	0.39	0.4*
i	$152°$	$180°$	$158° \pm 14°$
$\Sigma M, M_\odot$	5.7	5.94	6.2
$M_A, M_\odot$	4.0	–	3.7 ± 0.4
$M_B, M_\odot$	1.7	–	2.5 ± 0.4
B	0.30	–	0.41 ± 0.04
Δm	$2^m.94$	$2^m.98$	3^{m*}
β	0.063	0.060	0.06
Parallax	$0''.027$	$0''.026$	$0''.026 \pm 0''.001$
Spectral type$_A$	K0III	–	K0III
Spectral type$_B$	F0V	–	About A3V
M_{VA}	–	$-0^m.9$	$-0^m.9$
M_{VB}	–	$2^m.1$	$2^m.1$

β LMi = HIP51233

For this pair, visual (B relative to A), spectroscopic, and speckle interferometric observations are available, as well as two orbits: one computed by Soderhjelm (1999) and one computed by Hartkopf and Mason (2001), which is listed in the Sixth Catalog of Orbits. Both orbits are, as noted by their authors, inaccurate due to the lack of observations in the vicinity of the periastron.

These orbits are shown in Fig. 6: *1*—the orbit computed in this paper; *2*—the orbits of Hartkopf and Mason (2001) and Soderhjelm (1999) for $a_{pm} = 0''.13$ (they coincide in the sky plane); *3*—the results of speckle interferometric observations made from 1975 to 1995 for $B - \beta = 0''.36$; these observations agree well with all orbits. The orbital elements and other parameters of the binary are listed in Table 7.

Spectroscopic observations made by Griffin (2001) yielded a very precise time of the periastron passage—1999.33 ± 0.04. Thus the most accurate period estimate based on two times of periastron passage is—38.35 yr, although the time of the first passage

Table 6. Rms deviation of observations from the corresponding orbits

Orbit	In α	In δ	Full
Heintz + MSC ($a_{pm} = 0''.14$)	0.081	0.053	0.096
Heintz + MSC ($a_{pm} = 0''.21$)	0.039	0.036	0.054
Soderhjelm 1999 ($a_{pm} = 0''.21$)	0.033	0.032	0.046
This work	0.032	0.029	0.044

Table 7. Parameters of the β LMi pair

Parameter	Soderhjelm (1999)	Hartkopf and Mason (2001)	This work
a_{AB}	$0''.3$	$0''.363$	$0''.36$*
a_{pm}	–	–	$0''.13 \pm 0''.04$
P	39^d	$38^d.62$	$38^d.35$*
T	1998	1999.15	1999.33*
Ω	42°	41°.5	$40° \pm 15°$
ω	24°	29°.8	$41° \pm 12°$
e	0.69	0.668	0.7 ± 0.3
i	79°	79°.1	$81° \pm 11°$
$\Sigma M, M_\odot$	2.63	3.01	3.0*
$M_A, M_\odot$	–	–	1.3 ± 0.4
$M_B, M_\odot$	–	–	1.7 ± 0.4
B	–	–	0.57 ± 0.07
Δm	$1^m.32$	$1^m.43$	$1^m.43$*
β	0.23	0.21	0.21
Parallax	$0''.022$	$0''.022$	$0''.022$*
Spectral type$_A$	G8III–IV	G8III–IV	G8III–IV
Spectral type$_B$	–	–	About A8V
M_{VA}	–	$0^m.9$	$0^m.9$
M_{VB}	–	$2^m.3$	$2^m.3$

(1960.98) is not as exact as that of the second one. We adopted the above values for the period and the time of the periastron passage. We were the first to determine the component masses and the related quantity B for this pair from a_{pm} without invoking any additional assumptions. The quoted mass errors are dominated by the uncertainty of the inferred a_{pm}. The inferred mass M_A corresponds to the spectral type of G8 III–IV, absolute magnitude $M_{VA} = +0.9$, and color index $B-V = +0.9$ of the bright component. The lower mass of the bright component compared to that of the faint component might be due to its high metallicity: (Fe/H) = +0.17, according to Taylor (1999). The inferred mass M_B and absolute magnitude of the faint component leads us to conclude that its spectral type should be somewhere around A8V.

All three orbits, if computed with $a_{pm} = 0''.13$, agree equally well with the observations used and are virtually coincident in the sky plane. We determined the component masses for the first time.

CONCLUSIONS

Our studies have shown that the method for directly combining astrometric catalogs based on ground-based observations with the Hipparcos catalog data makes it possible to discover new astrometric binaries, to compute preliminary orbits of their photocenters, and to determine the component masses if the semimajor axis of the apparent ellipse in the plane of the sky exceeds $0''.08$ and the orbital period lies in the range 10 to 55 yr. This method is particularly efficient for a large component magnitude difference, for example, in detecting white dwarfs near stars within 50 pc.

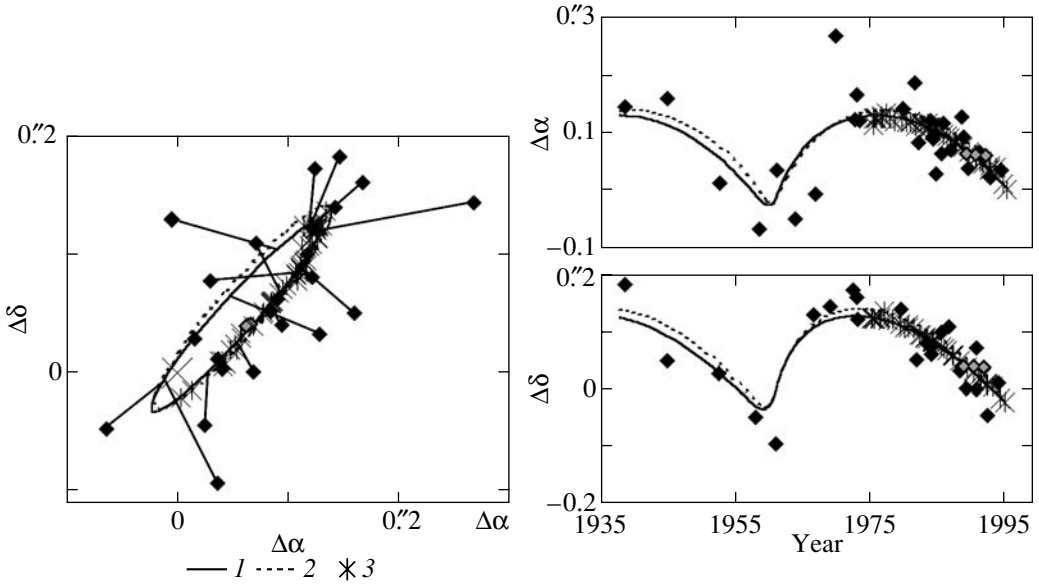

Fig. 6. Astrometric orbit of β LMi.

ACKNOWLEDGMENTS

We are grateful to Roger Griffin from the Cambridge Observatory (Great Britain), who provided his spectroscopic observations, and to Leslie Morrison from the Greenwich Observatory for a discussion of the Carlsberg Meridian Circle results we used.

REFERENCES

1. H. A. Abt, Astrophys. J., Suppl. Ser. **11**, 429 (1965).
2. C. W. Allen, *Astrophysical Quantities* (Athlone Press, London, 1973; Mir, Moscow, 1977).
3. H. J. Augensen and W. D. Heintz, Publ. Astron. Soc. Pac. **104**, 314 (1992).
4. D. Benest and J. L. Duvent, Astron. Astrophys. **299**, 621 (1995).
5. J. D. Drummond, J. C. Christou, and R. Q. Fugate, Astrophys. J. **450**, 380 (1995).
6. ESA, *Hipparcos and Tycho Catalogues,* ESA SP-1200 (1997).
7. B. P. Gerasimovich, Tsirk. Pulkov. Obs. **19**, 3 (1936).
8. T. M. Girard, H. Wu, J. T. Lee, *et al.*, Astron. J. **119**, 2428 (2000).
9. W. Gliese and H. Jahreiss, *Preliminary Version of the Third Catalogue of Nearby Stars* (Astronomisches Rechen-Institut, Heidelberg, 1991).
10. G. A. Gontcharov, A. A. Andronova, and O. A. Titov, Astron. Astrophys. **355**, 1164 (2000).
11. G. A. Gontcharov, A. A. Andronova, O. A. Titov, and E. V. Kornilov, Astron. Astrophys. **365**, 222 (2001).
12. G. A. Gontcharov and E. V. Kornilov, *Journees 1997: Systemes de reference spatio-temporels,* Ed. by J. Vondrak and N. Capitaine (Observatoire de Paris, Paris, 1997), p. 134.
13. R. Griffin, private communication (2001).
14. W. I. Hartkopf, B. D. Mason, G. L. Wycoff, *et al.*, *Forth Catalog of Interferometric Measurements of Binary Stars* (2001), http://ad.usno.navy.mil/wds/int4.html.
15. W. I. Hartkopf and B. D. Mason, *Sixth Catalog of Orbits of Visual Binary Stars* (2001), http://ad.usno.navy.mil/wds/orb6.html.
16. W. D. Heintz, Veroff. Sternwarte Munchen **5**, 252 (1963).
17. W. D. Heintz, Astrophys. J., Suppl. Ser. **111**, 335 (1997).
18. P. G. Judge, C. Jordan, and M. Rowan-Robinson, Mon. Not. R. Astron. Soc. **224**, 93 (1987).
19. O. V. Kiyaeva and O. A. Kalinichenko, Izv. GAO RAN **213**, 233 (1998).
20. Y. Kondo, T. H. Morgan, and J. L. Modisette, Publ. Astron. Soc. Pac. **89**, 163 (1977).
21. H. Plets, C. Waelkens, R. D. Oudmaijer, and L. B. F. M. Waters, Astron. Astrophys. **323**, 513 (1997).
22. S. Soderhjelm, Astron. Astrophys. **341**, 121 (1999).
23. B. J. Taylor, Astron. Astrophys., Suppl. Ser. **134**, 523 (1999).
24. A. A. Tokovinin, Astron. Astrophys., Suppl. Ser. **124**, 75 (1997).
25. C. Turon, M. Creze, D. Egret, *et al.*, Bull. Inf. Cent. Donnees Astron. Strasbourg **43**, 5 (1993).
26. W. F. Van Altena, J. T. Lee, and E. D. Hoffleit, *The General Catalogue of Trigonometric (Stellar) Parallaxes* (Yale Univ. Observatory, New Haven, 1995, 4th ed.).

Translated by A. Dambis

Astronomy Letters, Vol. 28, No. 4, 2002, pp. 272–278. Translated from Pis'ma v Astronomicheskiĭ Zhurnal, Vol. 28, No. 4, 2002, pp. 314–320.

Plasma Drift in the Solar Corona

M. M. Molodensky and V. L. Merzlyakov*

Institute of Terrestrial Magnetism, Ionosphere and Radiowave Propagation, Russian Academy of Sciences, Troitsk, 142092 Russia

Received August 17, 2001

Abstract—Model calculations of plasma drifts in the solar corona were performed. We established that only drifts in crossed fields could result in velocities V of several hundred kilometers per second. Such velocities are typical of coronal mass ejections (CMEs). We derived an analytic expression for V where n, the expansion harmonic of the magnetic-field strength, varies with time. As follows from this expression, V is a power function of the distance with index $(2-n)$ and the radial component changes sign $(n-1)$ times in the latitude range from $-\pi/2$ to $+\pi/2$. We found that if the magnetic dipole moment varies with time, the similarity between the spiral structures of coronal plasma is preserved when they displace within several solar radii and the density gradient at the conical boundaries increases (the apparent contrast is enhanced). There is a correspondence between the inferred model effects and the actually observed phenomena that accompany CMEs. © *2002 MAIK "Nauka/Interperiodica".*

Key words: *Sun, corona, magnetic field, drift*

1. INTRODUCTION

The magnetic field is a major factor that determines the structure and dynamics of the solar corona. Various kinds of magnetic reconnection are commonly suggested as the principal mechanism of dynamical motions (see, e.g., Linker and Mikić 1995). As yet no other possible mechanisms have been investigated in detail. Meanwhile, there are plasma drifts in the solar corona, because the magnetic field is spatially nonuniform and considerably varies with time. Among these drifts, there may be those which significantly affect the dynamical phenomena in the corona. Here, we study the coronal plasma drifts and reveal the accompanying effects.

2. ESTIMATES OF THE DRIFT VELOCITIES

Various types of plasma drift arise in the solar corona when the magnetic field is spatially and temporally nonuniform. In particular, temporal variations in the magnetic field $\mathbf{B}$ give rise to an electric field $\mathbf{E}$, which produces a drift in crossed fields across magnetic field lines with the velocity

$$\mathbf{V}_\perp = c\frac{\mathbf{E}\times\mathbf{B}}{B^2}. \qquad (1)$$

The electric drift velocity (1) is the same for electrons and protons, the main coronal plasma particles, provided that they are magnetized. In the coronal region under study with an extent up to $\approx 6R_\odot$, both electrons and protons are in a magnetized state, because the temperature is $\approx 10^6$ K, the electron density is $\leq 10^5$ cm^{-3}, and the magnetic-field strength is ≥ 0.1 G. For such plasma parameters, the frequency of collisions between protons and electrons is $\leq 5\times 10^{-3}$ s^{-1}, which is lower than their gyromagnetic frequencies, $\approx 10^3$ s^{-1} for protons, by many orders of magnitude.

A good approximation for the coronal magnetic fields is a potential field, with the dipole term being generally dominant. To estimate the coronal drift velocities, we restrict our analysis to a dipole magnetic configuration. In this case, the magnetic-field components are $B_r = 2M\cos\theta/r^3$ and $B_\theta = M\sin\theta/r^3$ and the vector potential has only one longitudinal component $A_\varphi = M\sin\theta/r^2$, where M is the dipole moment and θ is the polar angle. From the equation $\operatorname{curl}\mathbf{E} = (-1/c)(\partial\mathbf{B}/\partial t)$ for a known vector potential of the dipole field, we obtain the electric field $E_\varphi = (-1/c)\left(\dot{M}\sin\theta/r^2\right)$. Knowing E_φ, we derive an expression for velocity (1) in the form

$$\mathbf{V}_\perp = \frac{\dot{M}}{M}\frac{rB_\theta}{B_\theta^2+B_r^2}\left(B_\theta\mathbf{e}_r - B_r\mathbf{e}_\theta\right), \qquad (2)$$

where $\mathbf{e}_r$ and $\mathbf{e}_\theta$ are the unit vectors along r and θ and $\dot{M} = \partial M/\partial t$.

The radial component (2) is of interest primarily in the equatorial zone, because most of the rapid coronal

*E-mail: mvl@izmiran.rssi.ru

motions that lead to CMEs are observed there. Eq. (2) yields an estimate of the velocity $V_e \approx r\dot{M}/M$. If the relative change in dipole moment $\dot{M}/M$ is 10^{-3} s^{-1}, then the solar plasma velocity at the distance $r = R_\odot$ is 700 km s^{-1}. Note that this change $\dot{M}/M$ can result from the rapid motion of filaments (Molodensky and Filippov 1992).

When the change in dipole moment has the second time derivative $\ddot{M} \neq 0$, a polarization drift appears (Frank-Kamenetskii 1964):

$$\mathbf{V}_\mathrm{p} = \frac{mc}{e}\frac{c\dot{\mathbf{E}}}{B^2}, \tag{3}$$

where m and e are the plasma particle mass and charge, respectively. For the motion near the equator considered above, the drift (3) is

$$V_\mathrm{p} = \frac{mc}{e}\frac{r}{B_\theta}\frac{\ddot{M}}{M}. \tag{4}$$

Let us estimate the ratio $\ddot{M}/M$ from the observed maximum (1 km s^{-2}) CME accelerations. Using Eq. (2) for the radial electron drift and $\dot{M}/M = 10^{-3}$, we obtain $r\ddot{M}/M = 1.3$ km s^{-2}. The global magnetic-field strength at the distance $r = 2R_\odot$ is $B_\theta \approx 0.1$ G; hence, the polarization drift velocity (4) is 6×10^{-2} cm s^{-1} for electrons and $\approx$100 cm s^{-1} for protons.

The dipole magnetic configuration itself produces centrifugal and gradient drifts. The centrifugal drift is characterized by a displacement both across magnetic field lines and perpendicular to the radius of curvature R_k of the field line (Frank-Kamenetskii 1964):

$$\mathbf{V}_\mathrm{c} = \frac{mc}{e}\frac{V_\parallel^2}{B^2 R_\mathrm{k}^2}\mathbf{R}_\mathrm{k} \times \mathbf{B}, \tag{5}$$

where $V_\parallel$ is the velocity along the field line. At $r = 2R_\odot$ near the equator, $R_\mathrm{k} \approx 2R_\odot$, the centrifugal electron drift velocity is $4 \times 10^{-18} V_\parallel^2$ when $B_\theta = 0.1$ G. If the parallel velocity is assumed to be $V_\parallel = 1000$ km s^{-1}, then the electron and proton drifts are 4×10^{-2} and 70 cm s^{-1}, respectively.

The gradient drift velocity is (Frank-Kamenetskii 1964):

$$\mathbf{V}_\mathrm{gr} = \frac{1}{2}\frac{R_\mathrm{c}^2 \omega_\mathrm{c}}{B^2}\mathbf{B} \times \nabla\mathbf{B}, \tag{6}$$

where R_c is the gyroradius, $2.21 \times 10^{-2} T^{1/2} B^{-1}$ for the electron and $0.945 T^{1/2} B^{-1}$ for the proton; $T = 10^6$ K in the corona; and ω_c is the cyclotron frequency. The field gradient is $\nabla B \approx 3B/r$. For these conditions, the gradient drift of electrons and protons at $r = 2R_\odot$ is $\approx$0.9 m s^{-1}.

Apart from the above drifts related to temporal and spatial magnetic-field variations, a drift is also produced by a gradient in the solar gravitational field. The velocity of this drift is

$$V_\mathrm{g} = \frac{mc}{e}\frac{g(r)}{B_\theta}, \tag{7}$$

where $g(r)$ is the gravity at distance r from the solar center. Taking, as in the previous cases, $r = 2R_\odot$, we obtain a gravitational drift velocity of 4×10^{-3} cm s^{-1} for electrons and 7 cm s^{-1} for protons.

Our analysis of the drifts shows that only in crossed fields can the drift displace the coronal plasma at the velocity of several hundred kilometers per second typical of CMEs. The velocities of other drifts in the inner corona do not exceed 1 m s^{-1}.

DRIFT IN CROSSED FIELDS

Molodensky and Filippov (1992) and Molodensky *et al.* (1992) considered the mechanism of rapid filament motions. It implies that a stable equilibrium of the filament current in the field of active regions is possible if this current is not too large. In that case, there are two equilibrium positions of the filament: stable and unstable. As the current increases, these points approach each other and merge together; this is why the equilibrium disappears. The filament begins to accelerate and goes outside the active region. This situation is known in mathematics as a pleat catastrophe (Arnold 1989).

In the case under consideration, an important point is that the current associated with the filament rapidly flows. This current carries a dipole moment of the same order of magnitude as the dipole moment of an active region. The latter does not vary during the motion, but the total dipole moment varies on a time scale of $\sim R_\odot/V \approx 10^3$ s, where the velocity of the rapid filament motion is $V \approx 500$ km s^{-1}.

The above estimates for the various types of drift show that only the electric drift produces the velocity observed in the corona. The other drifts produce a velocity that is lower by at least six orders of magnitude. Therefore, we consider below only the electric drift.

Since the velocity of all charged particles is the same (the degree of ionization in the corona at $T = 10^6$ K is 100%), there are no causes for charge separation and the plasma, being quasi-neutral, moves as a whole at velocity $\mathbf{V}_\perp$. As for the longitudinal velocity parallel to $\mathbf{B}$, we note the following. CME is a rare (usually once in several days), large-scale ($\sim 10^{11}$ cm) motion with a sudden commencement. The initial state corresponds to a stationary homogeneous corona. A motion $V_\perp$ arises at some instant in time, and a plasma inhomogeneity and a

A summary of drift parameters

Types of drift	Maximum velocities	Peculiarities of motion
Electric	Up to 1000 km s^{-1}	Electrons and protons move with equal velocities in the same direction
Polarization	Up to 1 m s^{-1}	Electrons and protons move in opposite directions with velocities that differ by a factor of 1840
Centrifugal	70 cm s^{-1}	Same
Gravitational	7 cm s^{-1}	»
Gradient	<1 cm s^{-1}	Electrons and protons move in opposite directions with equal velocities

gas pressure gradient are produced through the displacements $\xi_\perp = \int V_\perp dt$, which results in the motion along field lines at a velocity of sound $V_s = (\gamma kT/m_i)^{1/2} \sim 10^7$ cm s^{-1}. Since this velocity is an order of magnitude lower than $V_\perp$, it may be disregarded. A velocity of the same order of magnitude is produced by a gravity of $g_\odot \times 10^3 \sim 10^7$ cm s^{-1}, where 10^3 s is the CME time scale.

Another CME peculiarity is that very small (of the order of several percent) variations in image contrast and the same variations in density are observed. This can be experimentally recorded by forming difference images: the disturbed corona minus the quiet corona. Therefore, the term with the transfer of the density gradient is much smaller than the term related to the compression of the medium. At $\rho = \rho_0 + \delta\rho$, where $\rho_0(x, y, z, t_o) = \text{const}$ and $|\delta\rho/\rho| \ll 1$, $|\rho \text{div}\mathbf{V}| \gg |\mathbf{V}\text{grad}\rho|$, because ρ_0 appears on the left and $\delta\rho$ appears on the right. Under the continuity condition, only the first term may be retained.

Let us investigate the electric drift (1) for specific configurations of the magnetic field that can be represented in the corona via the potential as

$$U = \sum \frac{C_{nm} P_n^m(\cos\theta)}{r^{n+1}} \begin{pmatrix} \sin m\varphi \\ \cos m\varphi \end{pmatrix} \qquad (8)$$
$$= \frac{q}{r} + \frac{M\cos\theta}{r^2} + \ldots,$$

where the first term corresponds to the end of a solenoid with strength $\mathbf{B} = (q/r^2)\,\mathbf{e}_r$, the second term corresponds to the dipole term, etc.

Since the dependence of the velocity (V) distribution on the magnetic-field structure is primarily of interest, it is appropriate to consider each harmonic in (8) separately to reveal any peculiarities of these distributions. This makes it possible to establish characteristic features of the motion in crossed fields for a particular magnetic configuration and to draw conclusions about the role of harmonics from the observed dynamical phenomena in the corona.

1. Consider the velocity field that emerges when q changes. Suppose that $\partial q/\partial t = \dot{q}$. In spherical coordinates, the magnetic field, its vector potential, and the electric field are, respectively,

$$\mathbf{B} = \mathbf{e}_r \frac{q}{r^2}, 0, 0; \quad \mathbf{A} = 0, 0, \mathbf{e}_\varphi q \frac{\cot\theta}{r}; \qquad (9)$$
$$\mathbf{E} = -\frac{1}{c}\dot{\mathbf{A}}; \quad \dot{\mathbf{A}} = \mathbf{e}_\varphi \dot{q} \frac{\cot\theta}{r}.$$

The velocity produced by the change in q is

$$\mathbf{V} = \mathbf{e}_\theta \frac{\dot{q}}{q} r\cot\theta. \qquad (10)$$

In this case,

$$\text{div}\mathbf{V} = -\frac{\dot{q}}{q}, \qquad \text{curl}\mathbf{V} = 2\mathbf{e}_\varphi \frac{\dot{q}}{q}\cot\theta. \qquad (11)$$

It follows from Eq. (10) that V becomes zero in the $z = 0$ plane, $x = r\sin\theta\sin\varphi$, $y = r\sin\theta\cos\varphi$, and $z = \cos\theta$. For $\dot{q}/q > 0$, the density increases, because $\partial\rho/\partial t + \rho\text{div}\mathbf{V} = 0$, and the vorticity of the velocity field also increases.

2. For a dipole, the vector potential, magnetic field, and velocity are given above. Expression (2) can be rewritten as

$$\mathbf{V}_\perp = \frac{\dot{M}}{M}\frac{\sin\theta r}{f(\theta)}\left(\sin\theta\mathbf{e}_r - 2\cos\theta\mathbf{e}_\theta\right), \qquad (12)$$

where

$$f(\theta) = 4\cos^2\theta + \sin^2\theta. \qquad (13)$$

The equation for magnetic surfaces is

$$\psi = \frac{M\sin^2\theta}{r} = C, \qquad (14)$$

where $C = \text{const}$. In addition, the current lines satisfy the equation

$$\frac{r^2}{\cos\theta} = K, \qquad (15)$$

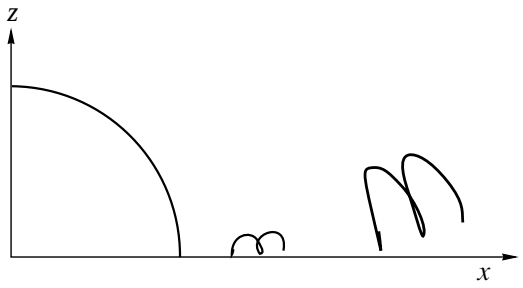

Fig. 1. Drift in the dipole field of a flat spiral structure at $\dot{M} > 0$, whose view is shown at the times when the left end displaces by $1.5r_0$ and $2.5r_0$. The arc of a circumference outlines the r_0 boundary.

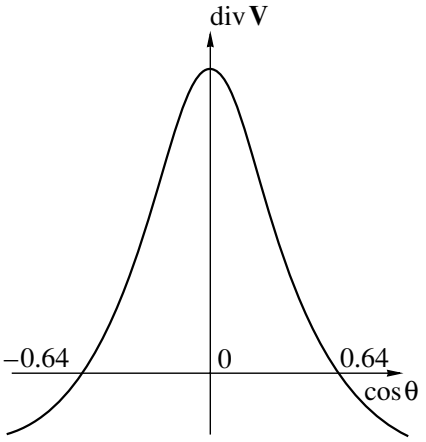

Fig. 2. div$\mathbf{V}$ versus $\cos\theta$. Near the equator, div$\mathbf{V}$ has a maximum; accordingly, the largest plasma rarefaction takes place here; when $|\cos\theta| > 0.64$, the plasma density increases, while on the surface of the cone separating these regions, the density is preserved.

where K is also a constant. When M changes (e.g., for $\dot{M}/M > 0$), the moving plasma particles cross the magnetic surfaces (14), so C/M decreases and for $C/M \to 0$, $r \to \infty$ at all θ except $\theta = 0, \pi$. In this case, K in Eq. (15) is preserved. Consequently, the drift can be described as follows: let us take a point x, z. For a given M, we determine C and K from Eqs. (14) and (15); specifying $M + \delta M$, we derive x_1 and z_1, the coordinates of the point displaced from x, z.

Figure 1 shows the computed motion of a loop (e.g., a prominence) from the region r_0, $\theta \approx \pi/2$ to $1.5r_0$ and $2.5r_0$. The loop shape slightly changes but its helicity is generally preserved, as is the similarity of other structures for moderately large changes in the distances.

From Eq. (12), we derive

$$\mathrm{div}\mathbf{V} = \frac{\dot{M}}{M}\,\frac{5 - 6\cos^2\theta - 15\cos^4\theta}{(3\cos^2\theta + 1)^2}\,. \qquad (16)$$

At $\cos\theta = 0.64$, Eq. (16) has a root. Therefore, Eq. (16) is positive for θ in the range $90° \pm 50°35$ Eq. (16) and negative outside this range (Fig. 2). It follows from the continuity condition that the plasma drift gives rise to a conical surface with an angle at the vertex of $2 \times 50°35$, on which the density is preserved. According to Koutchmy (personal communication), such effects as the conservation of similarity and the enhancement of contrast on individual cone generators are characteristic of CMEs.

3. At $n \neq 1$, using the general method of solving the Laplace vector equation curlcurl$\mathbf{A} = 0$, we obtain the vector potential and the electric field that determine $\mathbf{V}_\perp$. According to Morse and Feshbach (1953), the solution to the Laplace vector equation can be combined from the solutions to the scalar equation $\Delta U + K^2 U = 0$:

$$\mathbf{L} = \mathrm{grad}\varphi, \quad \mathbf{M} = \mathrm{curl}(\mathbf{a}, \omega\psi), \qquad (17)$$

$$\mathbf{N} = \frac{1}{K}\mathrm{curlcurl}(\mathbf{a}, \omega\chi),$$

where φ, ψ, and χ are the solutions to the scalar equation; $\mathbf{a}_1 = \mathbf{e}_r$; and $\omega = r$ (for spherical coordinates) when $K \to 0$, $\mathbf{L}$ and $\mathbf{N}$ are not independent. Therefore, $\mathbf{N}$ may be omitted, and two solutions will remain for which curl$\mathbf{L} = 0$, div$\mathbf{L} \neq 0$, and curl$\mathbf{M} \neq 0$, div$\mathbf{M} = 0$ (see the *Appendix*). This is enough to determine the vector (curl$\mathbf{r}\psi$) and scalar (φ) potentials. Let us write

$$\mathbf{A} = \mathrm{curl}\,\mathbf{r}\psi = -\mathrm{grad}\psi \times \mathbf{r} + \psi\,\mathrm{curl}\,\mathbf{r}. \qquad (18)$$

The last term in Eq. (18) is zero and

$$\mathrm{grad}\psi = \mathbf{B}. \qquad (19)$$

Consequently,

$$\mathbf{A} = [\mathbf{rB}], \qquad (20)$$

and, accordingly, $\mathbf{E} = (-1/c)[\mathbf{rB}]$; hence, we immediately derive the electric drift velocity (1) for harmonics $n \geq 1$ (8). For a point-like solenoid end, it follows from Eq. (20) that $A_\varphi = 0$ and Eq. (9) was derived in a different way.

4. Let us consider a simplified axisymmetric case, $B_\varphi = 0$, for harmonics $n \geq 2$. In this case, we obtain the following drift velocity from Eq. (1) using Eq. (20):

$$\mathbf{V} = -\frac{\dot{B}_\theta^{(n)} r}{B_\theta^2 + B_r^2}\,(B_\theta \mathbf{e}_r - B_r \mathbf{e}_\theta)\,. \qquad (21)$$

The latitudinal component of the n-harmonic, $B_\theta^{(n)}$, can be expressed in terms of the flux function Ψ:

$$B_\theta^{(n)} = -\frac{1}{r\sin\theta}\frac{\partial\Psi}{\partial r}. \qquad (22)$$

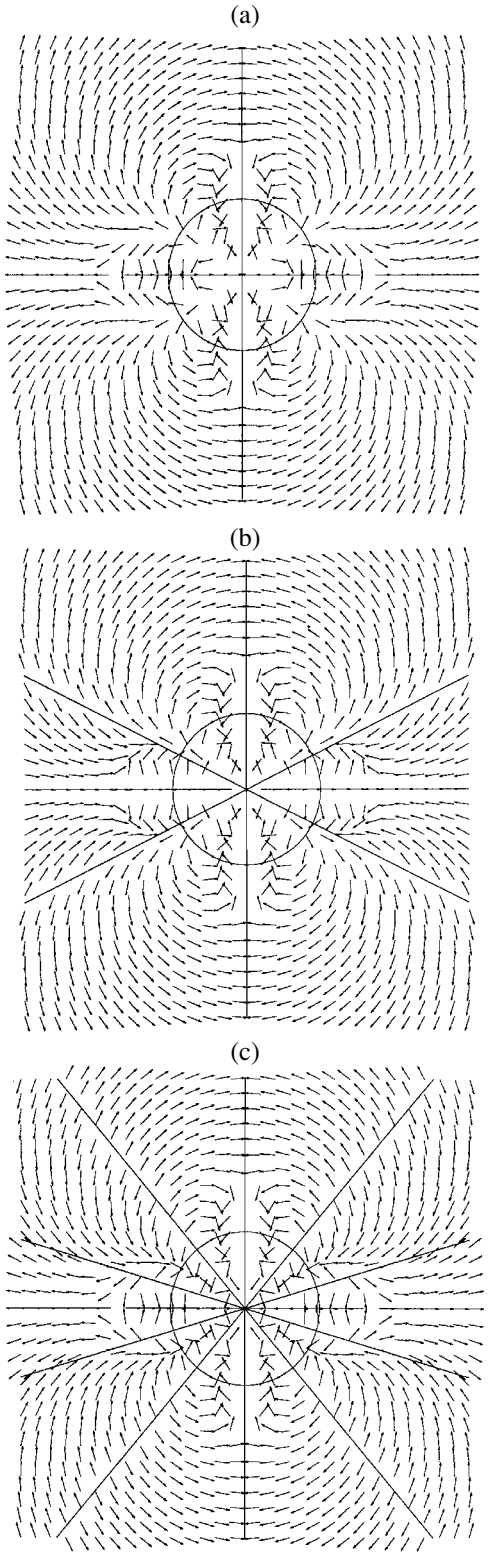

Fig. 3. The field of **V** directions in a magnetic configuration with three odd harmonics, $M = 1$, $C_3 = 2$, and $C_5 = -20$, for (a) $\dot{M} > 0$, (b) $\dot{C}_3 > 0$, and (c) $\dot{C}_5 > 0$. The number of regions with the same sign of the radial **V** component is equal to the index n at $\dot{C}_n \neq 0$.

Since $\Psi = \sin\theta \sum_n C_n(P_n^1(\cos\theta)/r^n)$ in the symmetric case, where $P_n^1(\cos\theta)$ is an associated Legendre polynomial, the time derivative of Eq. (22) is

$$\dot{B}_\theta^{(n)} = n\dot{C}_n \frac{P_n^1(\cos\theta)}{r^{n+2}}. \qquad (23)$$

For $r \to \infty$, the dipole plays a major role in the total magnetic field and, given Eq. (23), Eq. (21) for the velocity takes the form

$$\mathbf{V} = -\frac{n\dot{C}_n P_n^1(\cos\theta)}{r^{n-2} M f(\theta)} (\sin\theta \mathbf{e}_r + \cos\theta \mathbf{e}_\theta). \qquad (24)$$

It follows from Eq. (24) that the drift velocity is $\sim r^{2-n}$; i.e., at $n = 2$, there is no dependence on the distance, while for the higher harmonics, V falls off in a power proportional to the harmonic number. The radial velocity (24) within $0 \le \theta \le \pi$ changes sign $(n-1)$ times; the parameter $f(\theta)$ (13) is always of the same sign. The direction of the latitudinal component (24) changes within the same θ range n times. Figure 3 shows the fields of velocity directions for temporal variations in the first three odd harmonics of expansion (8): (a) $n = 1$, (b) $n = 3$, and (c) $n = 5$. In this case, the magnetic field is represented as the sum of harmonics with aligned moments and the initial values of $C_1 = M = 1$, $C_3 = 2$, and $C_5 = -20$. The straight lines in Fig. 3 separate the regions where the radial **V** component changes sign according to approximation (24), which correctly describes the drift direction. As we see from Fig. 3, the sizes of the regions with predominantly radial motion of the same sign decrease in the latitudinal direction with increasing harmonic number: the angular extent of such an equatorial region is 53° for the third harmonic and 33° for the fifth harmonic. This kind of effect can account for the emergence of CME with an angular size of $<50°$; their number is $\approx 50\%$, as estimated by Hundhausen (1993) and St. Cyr *et al.* (1999).

5. In the axisymmetric case, the procedure for calculating plasma particle trajectories described in Section 2 can also be implemented in the general case. Since in this case, there is the flux function $\psi = A_\varphi r \sin\theta$ and the motion is perpendicular to the field lines, the plasma volume element does not get off from equipotentials and the motion is related to the function ψ alone:

$$\begin{cases} U = C_1 \\ \psi = C_2(t), \end{cases} \qquad (25)$$

where $C_1 = \text{const}$ in the entire time of the motion and $C_2(t)$ is a function of time. System (29) closely matches the previously considered Eqs. (14) and (15) and

$$U = C_n \frac{P_n}{r^{n+1}}, \quad A_\varphi = C_n \frac{P_n^1}{r^{n+1}}, \qquad (26)$$

$$\mathbf{B} = -\text{grad}\, U = \text{curl}\, \mathbf{e}_\varphi A_\varphi.$$

CONCLUSIONS

The plasma motion in crossed fields has a number of peculiar features that distinguish it from other forms of motion. First of all, reasonable *a priori* estimates for the rate of change in the magnetic field (with a time scale of $\sim 10^3$ s) lead to the actually observable velocities in CMEs for a drift in crossed fields. All the other drifts are much slower.

The field decomposition into spherical harmonics allow us to separate the regions (bounded by conical surfaces) in which the sign of the radial velocity is preserved. The cone angle depends on the harmonic number; the larger the harmonic number, the smaller this angle.

In addition, a characteristic feature of the motion is that $\text{div}\mathbf{V} = 0$ on some surfaces: $\text{div}\mathbf{V} > 0$ on one side of the surface and $\text{div}\mathbf{V} < 0$ on its other side. Accordingly, the plasma density decreases everywhere where $\text{div}\mathbf{V} > 0$ and increases on the other side. The surface itself is a kind of a rigid wall on which the brightness contrast increases. Note that for the lowest harmonics, the similarity of structures is preserved during the motion. All these features represent a characteristic picture among CMEs and rapid motions of disappearing filaments whose more detailed discussion deserves a special analysis.

It should be noted that the assumptions of axial symmetry do not limit the generality of the entire analysis. Koutchmy *et al.* (2001) showed how a general field could be constructed from configurations that are symmetric about several (specified from practical considerations) axes. We also kept in mind this practical convenience.

ACKNOWLEDGMENTS

This study was supported by the Russian Foundation for Basic Research (project no. 99-02-16360).

APPENDIX

Above, we gave Eq. (20) for the vector potential of the magnetic field at $r > R_\odot$ if the current above the photosphere is zero. Koutchmy *et al.* (2001) represented the field as a set of axisymmetric harmonics, with each harmonic being symmetric about its own axis. Therefore, the total potential possesses no symmetry. Bearing in mind the problem of determining drifts in this configuration, lets us show that if

$$\mathbf{A} = \text{curl}\, \mathbf{r}\psi, \tag{A.1}$$

then

$$\text{curlcurl}\, \mathbf{A} = 0 \tag{A.2}$$

for

$$\Delta\psi = 0. \tag{A.3}$$

Indeed,

$$\mathbf{A} = \frac{\mathbf{e}_\theta}{\sin\theta}\frac{\partial\psi}{\partial\varphi} - \mathbf{e}_\varphi\frac{\partial\psi}{\partial\theta}, \tag{A.4}$$

$$\text{curl}\mathbf{A} = \frac{\mathbf{e}_r}{r\sin\theta}\left[-\frac{\partial}{\partial\theta}\left(\sin\theta\frac{\partial\psi}{\partial\theta}\right)\right. \tag{A.5}$$
$$\left. - \frac{\partial}{\partial\varphi}\left(\frac{1}{\sin\theta}\frac{\partial\psi}{\partial\varphi}\right)\right] + \frac{\mathbf{e}_\theta}{r}\frac{\partial}{\partial r}\left(r\frac{\partial\psi}{\partial\theta}\right)$$
$$+ \frac{\mathbf{e}_\varphi}{r}\frac{\partial}{\partial r}\left(\frac{r}{\sin\theta}\frac{\partial\psi}{\partial\varphi}\right).$$

Thus, we assume that $\partial/\partial\varphi = 0$ and

$$\text{curl}\mathbf{A} = -\frac{\mathbf{e}_r}{r\sin\theta}\frac{\partial}{\partial\theta}\left(\sin\theta\frac{\partial\psi}{\partial\theta}\right) \tag{A.6}$$
$$+ \frac{\mathbf{e}_\theta}{r}\frac{\partial}{\partial r}\left(r\frac{\partial\psi}{\partial\theta}\right),$$

$$\text{curlcurl}\mathbf{A} = \mathbf{e}_\varphi\frac{1}{r}\left[\frac{\partial^2}{\partial r^2}r\frac{\partial\psi}{\partial\theta}\right. \tag{A.7}$$
$$\left. + \frac{\partial}{\partial\theta}\left(\frac{1}{r\sin\theta}\frac{\partial}{\partial\theta}\left(\sin\theta\frac{\partial\psi}{\partial\theta}\right)\right)\right].$$

The latter relation can be rewritten as

$$\text{curlcurl}\mathbf{A} = \mathbf{e}_\varphi\frac{\partial}{\partial\theta}\left[\frac{1}{r}\frac{\partial^2}{\partial r^2}r\psi\right. \tag{A.8}$$
$$\left. + \frac{1}{r^2\sin\theta}\frac{\partial}{\partial\theta}\left(\sin\theta\frac{\partial\psi}{\partial\theta}\right)\right]$$

and the first term in square brackets can be written as

$$\frac{1}{r}\frac{\partial^2}{\partial r^2}(r\psi) = \frac{1}{r^2}\frac{\partial}{\partial r}r^2\frac{\partial\psi}{\partial r}r.$$

Consequently, the Laplace operator of ψ in spherical coordinates appears in square brackets. According to condition (A.3), this expression becomes zero. Thus, (A.2) follows from (A.8).

REFERENCES

1. V. I. Arnold, *Mathematical Methods of Classical Mechanics* (Nauka, Moscow, 1989; Springer-Verlag, New York, 1989).
2. D. A. Frank-Kamenetskii, *A Course on Plasma Physics* (Atomizdat, Moscow, 1964).
3. A. J. Hundhausen, J. Geophys. Res. **98**, 13 177 (1993).
4. S. A. Koutchmy, private communication.
5. S. A. Koutchmy, V. L. Merzlyakov, and M. M. Molodensky, Astron. Zh. **78**, 953 (2001) [Astron. Rep. **45**, 834 (2001)].
6. J. Linker and Z. Mikić, Astrophys. J. **438**, L45 (1995).

7. M. M. Molodensky and B. P. Filippov, *Magnetic Fields of Solar Active Regions* (Nauka, Moscow, 1992).
8. M. M. Molodensky, B. P. Filippov, and N. S. Shilova, Astron. Zh. **69**, 181 (1992) [Sov. Astron. **36**, 92 (1992)].
9. P. M. Morse and H. Feshbach, *Methods of Theoretical Physics* (McGraw-Hill, New York, 1953; Inostrannaya Literatura, Moscow, 1960), Vol. 2.
10. O. C. St. Cyr, J. T. Burkepile, A. J. Hundhausen, and A. R. Lecinski, J. Geophys. Res. **104**, 12 493 (1999).

Translated by V. Astakhov